HISTORY OF ICE-RAFTING IN THE ARCTIC OCEAN DURING GLACIAL MAXIMA THROUGH MARINE ISOTOPE STAGE 6

by

Shannon M. Cofield
B.S. May 2012, Old Dominion University
M.S. May 2015, Old Dominion University

A Dissertation Submitted to the Faculty of
Old Dominion University in Partial Fulfillment of the
Requirements for the Degree of

DOCTOR OF PHILOSOPHY

OCEANOGRAPHY

OLD DOMINION UNIVERSITY
August 2023

Approved by:

Richard Hale (Director)

Dennis Darby (Member)

George R. Whittecar (Member)

Thomas Allen (Member)

ABSTRACT

HISTORY OF ICE-RAFTING IN THE ARCTIC OCEAN DURING GLACIAL MAXIMA THROUGH MARINE ISOTOPE STAGE 6

Shannon M. Cofield
Old Dominion University, 2023
Director: Dr. Richard Hale

Numerous studies attempted to reconstruct Arctic paleoclimate, specifically ice mass timing and locations, during glacial maxima. While some regions, like the Barents-Svalbard Ice Sheet (BSIS) are well-studied, they may benefit from a high-resolution paleo proxy. Other regions are highly contested, such as the East Siberian Sea or the presence of a central Arctic Ocean ice mass.

This research uses an Fe-grain provenance method to (1) define how the BSIS behaved during Marine Isotope Stage (MIS) 2, 4, and 6, and when it retreated; (2) determine the presence and ages of Shelf Ice Masses (SIMs) in the Beaufort Sea and East Siberian Sea, or if these SIMs broke up during MIS 2, 4, and 6; and (3) identify whether large ice masses existed in the central Arctic Ocean that might have reduced or prevented ice-rafting during MIS 2, 4, and 6. This study uses elemental compositions of sand-sized Fe-grains within ice rafted debris (IRD) from the deep-sea marine sediment core HLY0503-JPC22 as a proxy for ice transport from 41 circum-Arctic Ocean Source Areas (SAs), and also develops new age model and sedimentation rates through MIS 6. The combined >63 μm IRD and Fe-grain peaks in the last three glacial stages indicate ice sheet collapses near the middle of glacial stages and often again near the termination. MIS 4 is a weak glacial stage with smaller ice sheets than MIS 2 and especially smaller than MIS 6. SIMs on the Beaufort Shelf or East Siberian Shelf are problematic during MIS 2 and 4 but could have existed during MIS 6 where the data are inconclusive. Distinct >1 kyr hiatuses in IRD and Fe-grain transport are only observed in MIS 6, suggesting a central Arctic ice mass existed, and probably consisted of grounded icebergs or shelf ice that reached the Lomonosov Ridge. This study provides an increased understanding of Arctic Ocean ice transport during MIS 2, 4, and 6, for the Barents-Svalbard Ice Sheet in the Eastern Arctic, the East Siberian Sea in the Western Arctic, and the Central Arctic Ocean.

Dedicated in memory of Professor Michele Darby, Dr. Chet Grosch, Dr. Larry Atkinson, my father, grandfather, and brother.

To all my family and friends, thank you for a lifetime of encouragement, even for my wildest ideas. Special thank you to my mother for a childhood filled with STEM camps, zoo visits, and museum trips. To my better half, thank you for supporting my ambitious adventures, and listening to all my deep sea, Fibonacci, and Mars rover discussions.

ACKNOWLEDGMENTS

This research would not have been possible without contributions and support from my extensive team. I would like to thank Dr. Dennis Darby for years of instruction, guidance, and collaboration. Stephen Herman served as a key contributor to this research through years of electron microprobe analysis and patiently training me on instrument protocols. Dr. Wes Myers, perhaps reluctantly, welcomed me into the sedimentology lab and not only guided me through my graduate research, but became a lifelong friend. My PhD committee- Dr. Rich Whittecar, Dr. Rip Hale (Chair), and Dr. Thomas Allen- provided years of guidance, productive feedback throughout my academic journey, shaped me through years of undergraduate and graduate courses, and countless memorable field trip adventures. I would like to extend my gratitude to Kristen St. John for her supplemental SEM analysis to support this research. I was fortunate to work alongside many undergraduate and graduate students who assisted me through years of analysis, including Dan, Phil, Patrick, Ryan, James, Lexy, Christina, and many others. Special thank you to Dr. Jens Bischof and Joyce Strain for their enthusiastic introduction to geology, which altered my entire trajectory. I want to recognize the entire Ocean and Earth Sciences Department for everyone’s support, encouragement, and multiple opportunities that created a well-rounded, albeit slightly quirky, geological oceanographer. Finally, I extend my appreciation to my colleagues at NASA’s Jet Propulsion Laboratory and my current team at the Bureau of Ocean Energy Management for additional support and exceptional opportunities to continue expanding my knowledge and experiences- on land, the deep sea, and Mars. Thank you Everyone!

NOMENCLATURE

AO	Arctic Oscillation
A1	Initial core age (ka)
A2	Secondary core age (ka)
BG	Beaufort Gyre
BSIS	Barents-Svalbard Ice Sheet
D-O	Dansgaard-Oeschger Event
D1	Initial core depth (cm)
D2	Secondary core depth (cm)
FIS	Ferro-Scandinavian Ice Sheet
GIS	Greenland Ice Sheet
GRIP	Greenland Ice Core Project
HOTRAX	Healy-Oden Trans-Arctic Expedition 2005
IIS	Innuitian Ice Sheet
IRD	Ice Rafted Debris (or Detritus)
JPC22	Abbreviation for sediment core HLY0503-JPC22
K_{ARM}/K	Magnetic grain proxy
Ka	Thousands of Years Ago
Kyr	Thousands of Years
LGM	Last Glacial Maximum
LIS	Laurentide Ice Sheet
LR04	Oxygen isotope benthic stack (Lisiecki and Raymo, 2005))

MIS	Marine Isotope Stage
NaN	Not a Number
PCHIP	Piecewise Cubic Hermite Interpolating Polynomial
SA	Source Areas
SEM	Scanning Electron Microscopy
SIM	Shelf Ice Mass
TPD	Transpolar Drift
$\delta^{18}O$	Ratio of oxygen-16 and oxygen-18

TABLE OF CONTENTS

LIST OF TABLES

LIST OF FIGURES

Figure Page

CHAPTER 1

INTRODUCTION

1.1 PROBLEM

In the past few decades, the Arctic Ocean has become a visible indicator of Earth's changing climate through reduced sea ice, glacier retreat, and warming sea surface temperatures. Likewise, in the past, the Arctic experienced dramatic climate changes during glacial periods related to global climate feedback loops impacting ice volume, sea level, ocean currents, and atmospheric conditions. Some of these conditions are well-constrained while others remain uncertain. The Barents Sea glacial history is well-documented, especially for MIS 2 (Elverhøi et al., 1993). However, high-resolution sediment analysis of a core taken near the Fram Strait can help address data gaps to resolve the dynamic, episodic history of the Svalbard-Barents Ice Sheet as it retreated during the Last Glacial Maximum (LGM) and even the preceding glacial maxima, MIS 6, which is poorly constrained at present (Fig. 1).

Previous studies have assumed much of the shelf under the East Siberian Sea near the Taymyr Peninsula to just east of Wrangel Island remained ice free during the LGM (Fig. 1). Likewise, new data suggest ice may have been present on the Chukchi Borderland (also referred to as the Chukchi Plateau) and East Siberian Sea, but the ages of these ice sheets remain uncertain (Basilyn et al., 2010; Dove et al., 2014) (Fig. 1).

If large ice masses existed on the East Siberian Shelf near Wrangel Island, the shelf regions of the Beaufort Sea (including the Chukchi Borderland), or the New Siberian Islands during glacial maxima, there should little to no ice-rafted detritus (IRD) from these areas during the period of ice growth (Fig. 1). If this area was occupied by grounded ice, little calving or sediment entrained sea ice could form and drift toward Fram Strait until the grounded ice mass disintegrated (Fig. 1). Since ice masses require much longer intervals to build than to disintegrate (Carlson, 2011), a large ice mass would prevent circum-Arctic ice transport; hence there should be hiatuses in IRD transport for long durations, likely exceeding 1 kyr.

Studies have hypothesized a large, floating ice sheet, or marine ice dome, in the central Arctic Ocean during glacial periods (Hughes et al., 1977; Grosswald and Hughes, 1999). A central Arctic Ice Sheet may have reached the Lomonosov Ridge as suggested by ice grounding evidence dating to MIS 6 ~130-191 ka (Jakobsson et al., 2013) (Fig. 1). However, broad evidence for these large, partially grounded central ice shelves, or an explanation of how they grew from adjacent landmasses or SIMs remains unknown (Jakobsson et al., 2013).

While age dates for deep-sea sediment cores from the Holocene are well constrained through radiocarbon chronology (Polyak et al., 2004; Darby et al., 1997, 2006) the lack of abundant forams throughout older Arctic sediment cores, and the maximum dating range of ^{14}C dating, makes radioisotope dating difficult. Previous studies have used a variety of methods including sediment color and coarse grain fractions (Dong et al., 2017), and correlation of physical properties, such as magnetic signature, combined with radiocarbon dating if foraminifera (or “forams”) or other shell fragments are present (Nowaczyk et al., 2001). Deep-sea cores that extend back millions of years have the benefit of correlating measured core paleomagnetic data to well-documented geomagnetic field reversals using the Geomagnetic Polarity Time Scale. However, paleomagnetics can still be used for cores that are younger than the most recent Brunhes-Matuyama magnetic reversal (~800 ka). For example, unique magnetic intensity signatures caused by sea level changes and bottom sediment winnowing that concentrated magnetic minerals can be related to past sea level changes documented in global oxygen isotope curves (Myers and Darby, 2015). Another important caveat to the problem of constructing Arctic age models is the tendency to focus on extremes within climatic data, such as glacial terminations (Jakobsson et al., 2014a). They also suggest dynamic data may reflect complexities in climate data, rather than inaccurate age control (Jakobsson et al., 2014a).

1.2 PURPOSE

This research will determine specific sources of IRD from a well-dated, high-resolution Fram Strait sediment core, HLY0503-JPC22 (or "JPC22"), positioned to capture IRD outflow, with an emphasis on glacial intervals to help resolve the following questions:

- Eastern Arctic Ocean: How did the Barents-Svalbard ice sheet behave during the LGM (MIS 2), as well as MIS 4 and 6, and when did it retreat during each of these stages?
- Western Arctic Ocean: Can we determine the presence and/or ages of SIMs on the East Siberian shelf near Wrangel Island; and the New Siberian Islands, and shelf areas of the Beaufort Sea during MIS 2, 4, and/ or 6, and determine when these SIMs (if present) broke up?
- Central Arctic Ocean: Did large ice masses exist in the central Arctic Ocean that might have reduced or prevented ice-rafting during MIS 2, 4, and/ or 6?

CHAPTER 2

BACKGROUND OF THE STUDY

2.1. REVIEW OF THE LITERATURE

This section provides an overview of Arctic Ocean oceanography, paleoclimate, Arctic ice types including a comparison of glacial and sea ice, and Arctic forams.

2.1.1 ARCTIC OCEAN AND PALEOCLIMATE BACKGROUND

The Arctic Ocean is the only modern ocean basin completely surrounded by land, which contributes to unique oceanographic features. Likewise, the Arctic paleoclimate is sensitive to a number of climatic cycles with a wide range of durations.

2.1.1.1 ARCTIC OCEANOGRAPHY AND CURRENTS

During the Pleistocene, the Arctic Ocean had one of the most unusual and dynamic paleoenvironments of any ocean basin. The Arctic Ocean is nearly surrounded by polar land masses, which have vast continental shelves extending hundreds of kilometers toward the central Arctic Ocean, especially in the Chukchi Sea, East Siberian Sea, Laptev Sea, Kara Sea, and Barents Shelf (Fig. 1).

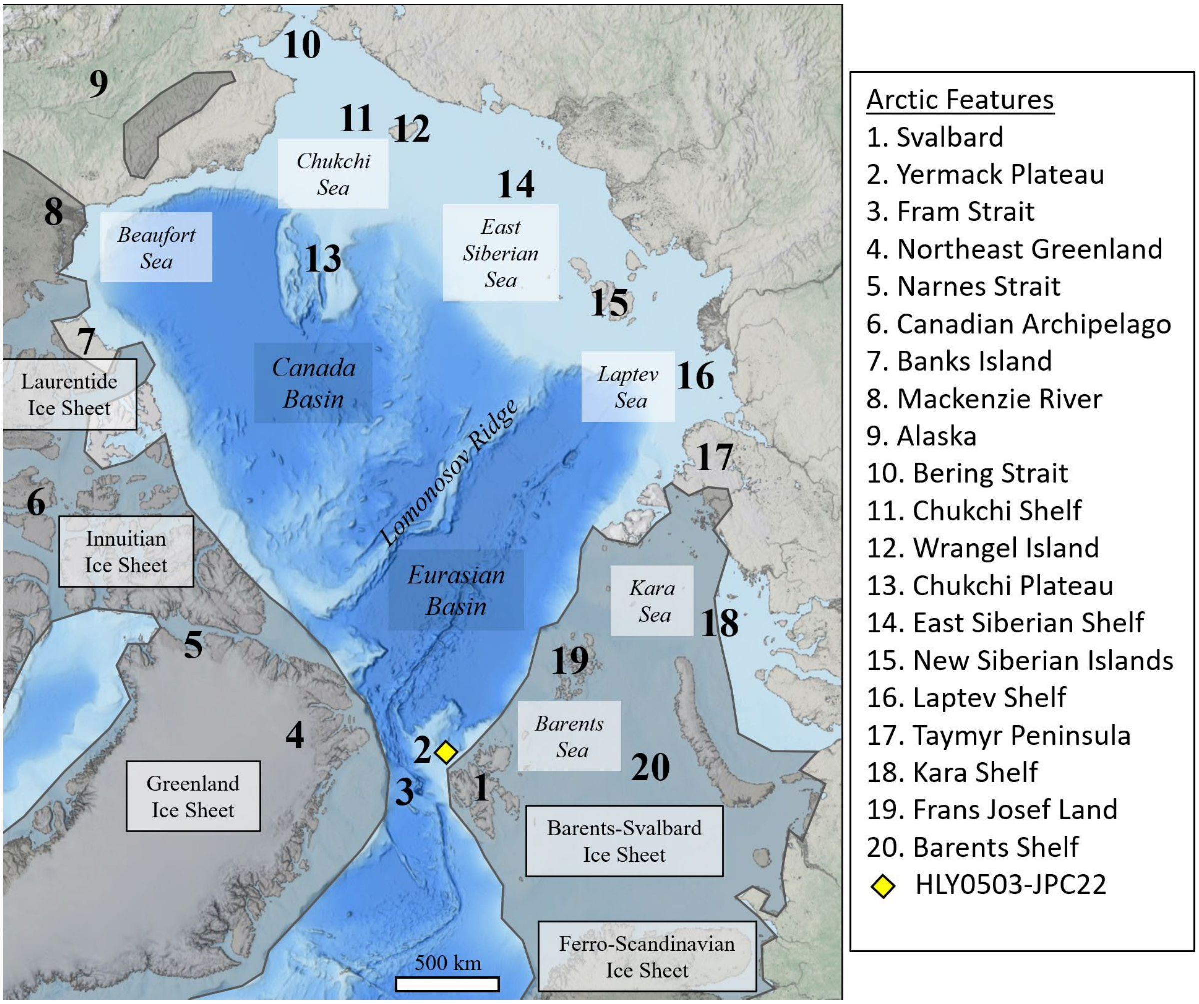

Fig. 1. Locations of Laurentide Ice Sheet (LIS), Innuitian Ice Sheet (IIS), Greenland Ice Sheet (GIS), Barents-Svalbard Ice Sheet (BSIS), and a portion of the Ferro-Scandinavian Ice Sheet (FIS). These are general ice sheet locations and extents, based on ice extents from Jakobsson et al. (2013), vary during MIS 2, 4, and 6 (After NOAA-NCEI, 2020). Additional geographic locations (right column) are represented by corresponding numbers on the map.

The Fram Strait and the Bering Strait serve as direct connections between the Arctic Ocean waters to the global ocean Atlantic Waters and Pacific Waters (Macdonald et al., 2004) (Fig. 1). Only the Fram Strait contains a deep, rifting basin which allows the exchange of surface, intermediate, and deep-water masses from the North Atlantic. The Bering Strait lacks a similar deep, rifting basin. Therefore, Bering Strait shelf regions are almost entirely exposed during low stand sea levels associated with glacial periods, thus prevents ocean water exchanges. Landmasses surrounding the Arctic Ocean contain several large rivers which supply a sizeable volume of fresh water to the Arctic Ocean surface waters. The input of fresh river water contributes to low salinity (~28 ppt) Arctic Ocean surface waters (Myhre et al., 1995). Directly below the surface waters, the thin Polar Mixed Layer sits atop the Pacific Intermediate waters and the Atlantic Intermediate waters, entering from their respective basins. The Lomonosov Ridge subdivides the Arctic Ocean basin into the Canada Basin and the Eurasian Basin, each with their own distinct bottom waters (Fig. 1).

Owing to the extreme high latitude of the Arctic Ocean, the region is subject to strong Coriolis Effect, and the Arctic Oscillation (AO). The primary surface currents in the Arctic Ocean are the Beaufort Gyre, which rotates clockwise in the Canada Basin, and the Transpolar Drift, which moves from the East Siberian and Laptev Seas toward the Fram Strait (Aagaard and Carmack, 1989; Jakobsson et al., 2013; Timmermans and Marshall, 2020) (Figs. 1 and 2). The AO has two phases that impact Arctic Ocean circulation: positive and negative. When the AO is in a positive phase, the atmospheric pressure over the north pole is lower than normal, which leads to strong Westerlies in the upper atmosphere. This prevents cold Arctic air from reaching lower latitudes, so the climate tends to stay cooler over the Arctic Ocean. A positive AO causes the Transpolar Drift to become stronger and shift closer to North America transporting thicker ice toward the Fram Strait (Rigor et al., 2002). Large transports of ice to the North Atlantic can cause freshening at deep-water formation sites, leading to a slowing of global thermohaline circulation. A positive AO likely dominates glacial intervals. When the AO is in the negative phase, atmospheric pressure is higher than normal, causing weaker Westerlies and allowing cool Arctic air to reach lower latitudes. During the negative phase, the Transpolar Drift shifts closer to Russia and Beaufort Gyre circulation intensifies. The exact mechanism controlling the AO remains unknown (Dickson et al., 2000).

2.1.1.2 ARCTIC OCEAN LONG-TERM CYCLES

On a longer timescale than AO phases, ~1,500yrs (Darby et al., 2012), the paleoclimate during the Pleistocene was dominated by a series of glacial and interglaciation periods. These climate variabilities are primarily controlled by Milankovitch (or "Milankovic") Cycles- orbital cycles of Eccentricity (~100 kyr), Obliquity (~41 kyr), and Precession (~26 kyr). Between 800-2,500 ka, the dominant forcing appears to be Obliquity. However, the transition from a 40-kyr cycle to an eccentricity-dominated 100-kyr cycle is known as the Mid-Pleistocene Transition (~800 ka), but the exact cause remains debated (Lisiecki and Raymo, 2005). The 100-kyr cycles had much larger temperature variations than 40-kyr cycles, which likely contributed to larger ice sheets. These timeframes have been constrained by isotope analysis and are commonly referred to as Marine Isotope Stages (MIS).

With stronger glacial periods during the last 800 kyr, large ice sheets developed during these periods. As glacial ice formed, global sea levels dropped >150 m (Jakobsson et al., 2014b). In the Arctic Ocean, the drop in sea level exposed nearly all of the vast continental shelves, resulting in a reduced Arctic Ocean volume and area. With the subsurface Bering Strait and Canadian Archipelago transformed to dry land or ice covered, the only exchange between Arctic Ocean waters and global oceans was through the Fram Strait (Fig. 1).

However, not all glacial maxima exhibited the same traits. While MIS 2 (14-29 ka) was the most-recent glacial maximum (LGM), Jakobsson et al. (2010) theorized MIS 6 (130-191 ka) ice sheets may have been much larger as a result of orbital parameters that affected the spring season. During MIS 6, incoming solar radiation was lower, and the spring season was longer, which allowed snow cover to remain in place with less exposure to summer melting periods (Colleoni et al., 2011). Isotopic evidence indicates that MIS 4 (57-71 ka) was much less severe than MIS 2 or MIS 6 (Lisiecki and Raymo, 2005).

Evidence of terrestrial glacial geomorphology and iceberg gouging on bathymetric highs clearly demonstrate that the Arctic Ocean hosted a series of glacial and ice sheet build ups and decays but change across the entire Arctic Ocean was not homogenous. Variability in forcing mechanisms between different regions resulted in locally specific ice buildup and decay patterns, or even prevented ice buildup. For glacial ice, the climate may be cold enough, but if there is no source for precipitation to develop, the ice will not develop on land. If winds are strong enough over a specific area, a region of open water, or polynya, may form. While a polynya may produce sea ice in areas downwind, the area directly affected by the strong winds may remain ice free.

2.1.1.3 ARCTIC OCEAN MILLENNIAL CYCLES

Milankovitch Cycles account for paleoclimate changes on timescales ranging from 10 kyr to 100 kyr and have global implications due to their origin in orbital variations. At the regional scale, however, additional millennial cycles in the North Atlantic influence Arctic ice dynamics and IRD transport.

Heinrich events were identified through distinct peaks in IRD abundances in marine sediment cores at 7-10-kyr intervals linked to cycles of extensive iceberg discharges (Heinrich, 1988). ~11 ka distinct Heinrich events were identified between 10-80 ka in the North Atlantic, related to surging ice calving from the Laurentide Ice Sheet through Hudson Strait (Bond et al., 1993). Heinrich events are identified by large abundances of IRD, typically 20% detrital limestone and unique clays characteristics. Another interesting observation is the lack of forams during Heinrich events, which reflect a decrease in ocean productivity during these intervals (Broecker, 1994), possible due to reduced salinity (Bond, 1992). While limestone IRD (typical of the LIS) is not the focus of this study, foram abundances are estimated.

Dansgaard-Oeschger (D-O) events were identified by rapid cool-cold 1.5 kyr oscillations during glacial periods in Greenland Ice Core Project (GRIP) data. D-O events have been associated with iceberg calving intervals (Bond and Lotti, 1995). GRIP data only extend back ~250 kyr (Dansgaard et al., 1993); therefore, D-O events have been primarily identified in the Late Pleistocene. Similar to Heinrich events, D-O events are associated with IRD peaks, albeit less pronounced than those associated with Heinrich events (Bond et al., 1993).

Bond events, or Bond cycles, have been linked to North Atlantic minor IRD ice rafting events in ~1.5 kyr cycles. Unlike D-O events which occurred during glacial periods, Bond events occur during the Holocene (~12ka to present). The origin of these cycles remains debated but have been linked to variations in solar output (Bond et al., 2001).

All of these millennial cycles are related hypothetically, but the exact nature of their relationship remains under investigation. In general, during a glacial period, there are rapid "warming" and cooling events, D-O cycles. These cycles vary in intensity, becoming more extreme toward the termination of each glacial period. During the coldest D-O cycle of each glacial period, there was an associated Heinrich event followed by rapid warming during the glacial termination before the initiation of the next glacial cycle. The most recent of these coldest D-O cycles was the Younger Dryas (~11.5 ka), while the first Bond Event occurred 11.1 ka (Bond et al., 2001).

2.1.2 ARCTIC ICE BACKGROUND

There are three main categories of Arctic Ocean ice: glacial ice sheets, SIMs, and sea ice. Glacial ice includes any ice that originates on land such as an ice sheet, ice cap, or ice shelf. SIMs grow in place on a shelf and grow thick enough to interact with the seabed but lack evidence of terrestrial origin. Sea ice does not originate on land and is further differentiated by age and nexus location. First-year sea ice includes ice that only has a single year of growth, whereas multi-year ice has >1 yr of growth and does not melt completely during the summer. Fast ice forms attached to a shoreline, while drift ice does not form attached to the shoreline and forms by suspension freezing that can entrain sediment when it is suspended by wind-driven turbulence in open water depths <50 m. Anchor ice forms wither when groundwater intruding into the Arctic Ocean freezes at the sediment-water interface, or due to turbulent overturning that allows supercooled water to reach depths >50 m (Reimnitz et al., 1987).

All of the described Arctic ice types have the ability to entrain sediment, referred to as IRD, as they form. Any ice that enters the Arctic Ocean will carry and transport IRD as it floats with the wind and currents. Glacial ice tends to contain a mix of fine-grained material and coarser-grained materials. Most sea ice tends to only contain fine-grained material that was in suspension in the water column. While anchor ice can theoretically contain both coarser and finer-grained materials, Arctic shelves are mostly fine-grained (<250 µm), thus anchor ice contains mostly finer-grained sediment (Darby et al., 2011).

Sedimentation rates are extremely low in the Arctic Ocean, typically 1-2 cm/kyr. Depending on the location and climate forcing (i.e., MIS), rates may range from mm/kyr to cm/kyr. The Fram Strait boasts one of the highest sedimentation rates in the Arctic Ocean (Norgaard-Pederson et al., 2003). A deep-sea marine sediment core collected proximal to this study's core, P2423a, (80º02'N, 05º26'W, 829 m water depth) demonstrates sedimentation rates ranging from 0.8 cm/kyr during the Holocene to 7.2 cm/kyr during MIS 2 (Notholt, 1998).

2.1.2.1 ARCTIC ICE SHEETS

During MIS 2, 4, and 6 glacial periods, there were five important ice sheets (Fig. 1): the Laurentide Ice Sheet (LIS), Innuitian Ice Sheet (IIS), Greenland Ice Sheet (GIS), Barents-Svalbard Ice Sheet (BSIS), and Fenno-Scandinavian Ice Sheet (FIS).

The location and history of the two major ice sheets, the Laurentide and Fenno-Scandinavian Ice Sheets, during the Pleistocene have been fairly well-constrained (Dyke and Prest, 1987; Dyke et al., 2002; Ottesen et al., 2002; Dahlgren and Vorren, 2003; Levitan, 2009). Even the lesser Innuitian ice sheets, which occupied much of the Canadian Archipelago in the Arctic, is now well-documented as to its extent as a continuous ice sheet that joined the Greenland Ice Sheet in Narnes Strait during the last glacial maxima and the Laurentide Ice Sheet to its south (Fig. 1)(England, 1999).

The BSIS covered nearly all the Barents and Kara Sea Shelves (Landvik et al., 1998; Kneis et al., 1999). Geomorphological evidence, such as grounding-zone wedges, suggests the BSIS retreat during the LGM was extremely episodic (Dowdseswell et al., 2008; Ingolfsson and Landvick, 2013). Developing a better understanding of the dynamic history of this ice sheet's retreat may provide some insights into modern dynamic ice sheet behavior. For example, if an ice sheet's disintegration intervals are more dynamic than previously identified, especially during a period of warming, it provides insights to how modern-day ice sheets may respond as the climate continues to warm.

Other proposed ice masses and shelf ice in the Arctic are still either speculative or unconstrained as far as their extent and history (Jakobsson et al., 2001). Recently multibeam and seismic evidence was obtained to suggest the presence of an ice mass on the East Siberian Sea shelf, but the extent and timing of this glacial shelf ice is unknown (Jakobsson et al. 2013, 2016). Even the thickness and existence of a large ice cap in the central Arctic has been proposed but never documented with physical evidence (Broecker, 1975; Hughes et al., 1977; Grosswald, 1980; Denton, 1981; Grosswald and Hughes, 1999, 2008). The Fe-grain data in this study will help constrain the existence, or lack, or a large central Arctic ice cap.

2.1.2.2 SHELF ICE MASSES

Recent multibeam bathymetric surveys and seismic surveys on the East Siberian shelf near Wrangel Island have revealed evidence for extensive glacial gouges in water depths up to 1,200 m (Niessen et al., 2013), which implies the presence of a ~1,000 m thick ice mass on this shelf area during some past glacial maxima. Additional geophysical data and sediment cores propose an interpreted glacial trough on the East Siberian Margin, referred to as the De Long Trough, most likely during MIS 6 (O’Regan et al., 2017). There is little evidence that large ice sheets occupied the adjacent continent, so this ice mass must have grown in place as a SIM. Minimal isostatic rebound on this shelf suggests it was unlikely that this SIM existed during MIS 2 (O’Regan et al., 2017). Numeric models of ice volume support the hypothesis of ice grounding in East Siberian Sea down to 1,000 m water depth during MIS 6 (Colleoni et al., 2016). Other numeric models showed an absence of a Wrangel Island SIM during MIS 2 and MIS 4, but a large SIM over Wrangel Island extending across the Chukchi Plateau during MIS 6 (Batchelor et al., 2019). Additionally, these models show an absence of ice over the East Siberian Shelf during MIS 2, 4, and 6. Whether SIMs occupied the entire East Siberian Shelf or just the easternmost portion, and when such a large ice mass occupied this area, remain unresolved.

Additional SIMs have been proposed for other circum-Arctic areas such as the Beaufort Shelf from the Mackenzie River to western Alaska, however the timing of their formation and break up is unknown (Jakobsson et al., 2013) (Fig. 1). Batchelor et al. (2019) numerical models do not indicate SIMs were present during MIS 2, 4 or 6, but the LIS may have extended to the Mackenize River.

2.1.2.3 CENTRAL ARCTIC OCEAN ICE CAP

Previous studies have proposed that a large, floating ice cap, or marine ice dome, existed in the central Arctic Ocean during some glacial maxima that might have been ≥1 km in thickness (Hughes et al., 1977; Grosswald and Hughes, 1999). Such large ice masses were proposed based on a global imbalance between the estimated glacial ice volume and calculated ice volume based on the $^{18}O/^{16}O$ ratio ($\delta^{18}O$) in marine benthic shells. Lighter ^{16}O isotope preferentially evaporate and fall as precipitation over land. In the Arctic, precipitation falls as snow and builds massive glaciers. The depletion of ^{16}O leaves the oceans seemingly “enriched” in the heavier ^{18}O isotope. Oxygen isotope analysis on marine sediment cores shows a peak favoring ^{18}O during glacial periods. Benthic forams in a Pacific deep-sea core showed a change in $^{18}O/^{16}O$ of 1.70 per mil during an interglacial-glacial transition. Deep-sea temperatures remain near freezing, so the change in the $^{18}O/^{16}O$ ratio did not result from deep-sea cooling. Since the volume of glacial ice has been well-documented as well as the resulting eustatic sea level change, it has been suggested that the ^{18}O-enriched water was stored as floating ice on the Arctic Ocean (Shackleton and Opdyke, 1973).

In addition, recent multibeam evidence indicates the grounding of very large ice masses in water depths up to 1km on the Lomonosov Ridge during MIS 6 (Vogt et al., 1994; Polyak et al., 2001; Jakobsson et al., 1999, 2008, 2010) and the Chukchi Borderland possibly during MIS 2 and 6 (Polyak et al., 2001). The history of these large ice masses and their impact on ice-rafting in the Arctic is still uncertain. There is evidence that the Chukchi Borderland groundings caused deviations in drift paths of icebergs during MIS 2. However, the impact of such large ice masses in the central Arctic during glacial maxima on sea ice-rafting is unknown (Bischof and Darby, 2002).

2.1.3 SEA ICE AND GLACIAL ICE RELATIONSHIPS

Sea ice and glacial ice impact climate feedback systems differently. Sea ice plays a critical role in ocean-atmosphere exchanges, while glacial ice affects ocean chemistry, namely Oxygen isotopes. Both sea ice and glacial ice can entrain and transport sediment. When drifting ice exits the Arctic Ocean, it may encounter slightly warmer surface waters, typically near Fram Strait in the North Atlantic Ocean. The entrained sediment is deposited on the seafloor by melt-out. The presence of thick ice masses in the central Arctic Ocean during glacial maxima would slow or block IRD transport of sea ice from non-glaciated shelves such as the westernmost part of the East Siberian or Laptev Sea sources to Fram Strait. If IRD from the East Siberian or Laptev Sea are identified in sediment cores from Fram Strait during glacial maxima, it would suggest ice was able to circulate, and the Arctic Ocean was not covered by thick ice capable of shutting-down ice-rafting. Correlating IRD abundance with glacial, or sea ice volume or rafting is complicated because of variations in melt-out rates.

Marine sediment cores collected in Fram Strait have shown intervals of coarse-grained IRD deposition, which identify intervals of rapid calving typically at the onset or termination of glacial periods, while finer-grained IRD deposition and IRD from areas never glaciated identify intervals of primarily sea ice-rafting (Darby and Zimmerman, 2008; Darby et al., 2010). While this study analyzes bulk IRD samples, the provenance analysis is based on Fe-grain elemental compositions. Sand-size Fe-grains in IRD provide specific geospatial source identification that can often permit the distinction between sea ice and iceberg IRD (Darby et al., 2011, 2015). The combination of IRD textural analysis and Fe-grain provenance in cores traversed by icebergs and sea ice in the past can help resolve questions related to sediment source and net drift patterns through time. From this the location and timing of large ice masses can be better constrained. Therefore, it is important to distinguish these types of ice (Stickley et al., 2009).

Different types of ice can transport sediments ranging from fine (<45 µm) to coarse-grained (>250 µm). Sea ice transports fine-grained sediments, but may include sediments generally <250 µm, largely due to the fine-grained nature of the Arctic shelves where this ice forms (Darby et al., 2011). Icebergs calved from glacial ice can transport sediment of any size, and often coarser IRD than typically found in sea ice (Darby et al., 2006). Additionally, sea ice and iceberg IRD can usually be distinguished by texture, but there are many exceptions such as anchor ice which has the capability to entrain any size sediment (Darby et al., 2011). To be certain of the sea ice mode of transport, a source needs to be identified that was free of glacial ice, such as the Laptev Sea, or complete absence of >250-µm grains.

To further differentiate sea-ice rafting from glacial transport in the East Siberian Sea, Scanning Electron Microscopy (SEM) provides textural data and surface markings on quartz grains (St. John et al., 2012). Sea-ice-rafted grains are sub-rounded with medium relief, while grains transported by glacial ice are more angular, with lower relief, and may exhibit striations or other glacial process microfeatures. Before becoming entrained in sea-ice, sediments were transported to the coastal (land) environment, thus making them subject to enhanced chemical weathering relative grains transported by glacial ice (Stickley et al., 2009; St. John et al., 2015).

Scanning Electron Microscope (SEM) analysis of surface markings on >250 μm quartz grains from selected samples should help confirm transport by glacial ice or sea ice.

In addition to distinguishing sea ice and iceberg IRD, the Fe-grain provenance analysis can identify circum-Arctic locations of IRD reaching the Fram Strait throughout glacial stages (MIS 2, 4, and 6). This will place constraints on ice drift across the Arctic with implications for thick ice accumulations on various Arctic shelves.

2.1.4 FORAMINIFERA

While forams in most Arctic marine sediment cores are not as plentiful as marine sediment cores from tropical locations, they are not entirely absent. The predominant species in the Arctic are the planktonic *Neogloboquadrina pachyderma.* The isotopic ratios preserved in all foram shells, or tests, reflect ocean water chemistry during their formation, which varies with global climate and ice volume. While not directly analyzed in this study, the direction of *N. pachyderma* test formation (sinistral vs. dextral) changes with ocean water temperature, providing additional context about the general Arctic ocean conditions. While a variety of factors can impact foram abundance on relatively short time scales (i.e., food sources, nutrient availability, seasonal effects), the generally low sedimentation rates observed in the Arctic Ocean negates the impacts of such high-frequency variability.

The presence of forams may indicate the absence of sea ice, polynyas driven by katabatic winds from steep glacial fronts or polar plateaus, or sea ice which still transmitted light level required for blooms. Forams are assumed to be present during all open water conditions (Noorgard-Pedeerson et al., 2007). However, the absence of forams may indicate long periods of limited primary production (i.e., thick ice blocking light transmission). Unlike the methodology for the circum-Arctic Fe-grain analysis, forams likely formed in the water masses over the core site and were not transported by sea or glacial ice. Therefore, foram abundances provide a general context of sea ice conditions on the Yermack Plateau (Fig. 1). Since the majority of forams in this study are *N. pachyderma*, larger forams (>63 µm) are categorized as adult-stage, and smaller forams (45 µm to 63 µm) as juvenile-stage.

2.2 LIMITATIONS OF EXISTING STUDIES

Most Arctic paleoclimate studies suffer from a similar set of limitations. Low sedimentation rates result in coarse temporal resolution. Unlike tropical analogs, deep-sea Arctic Ocean sediments lack forams throughout a sediment core. When present, sedimentologists analyze forams for a variety of isotopes or carbon dating, which provide proxies for absolute ages in sediment cores. Unlike cyclic paleoclimate proxies (i.e., tree rings, lake varve layers, ice core layers), Arctic Ocean sediment layers may contain hiatuses or a range of sedimentation rates. Developing an age model for a sediment core is crucial to interpreting core data. Without datable material or cyclic layers, developing age models for Arctic Ocean sediment cores remains a challenge. This study develops an age model based on a magnetic grain size proxy from JPC22 correlated to Vostok $\delta^{18}O$ atmospheric ice core data, as outline in Xuan et al. (2011).

CHAPTER 3

METHODOLOGY

3.1 RESEARCH DESIGN

The Fe-grain fingerprinting technique for sediment provenance determination has proven to be a robust method for identifying unique source regions throughout the Arctic Ocean (Darby, 2003, 2015). The method utilizes the chemistry of individual detrital sand-sized Fe-grains as a proxy for paleo ice drift in the Arctic Ocean. Ice that forms on or near Arctic margins, including glacial ice, SIMs, and sea ice, can entrain sediment from their respective geographic locations. Fig. 2 shows the 41 circum-Arctic locations, known as Source Areas (SA), used to identify the provenance of Fe-grains in this study. Typically, Arctic Ocean currents transport ice away from their SAs and around the Arctic Ocean (Fig. 2). Because lower sea levels during glacial periods terminate outflow through the Bering Strait, drifting ice either remains in cold Arctic waters, or exits to the south through Fram Strait. Once ice reaches the slightly warmer North Atlantic waters and begins melting, IRD is deposited.

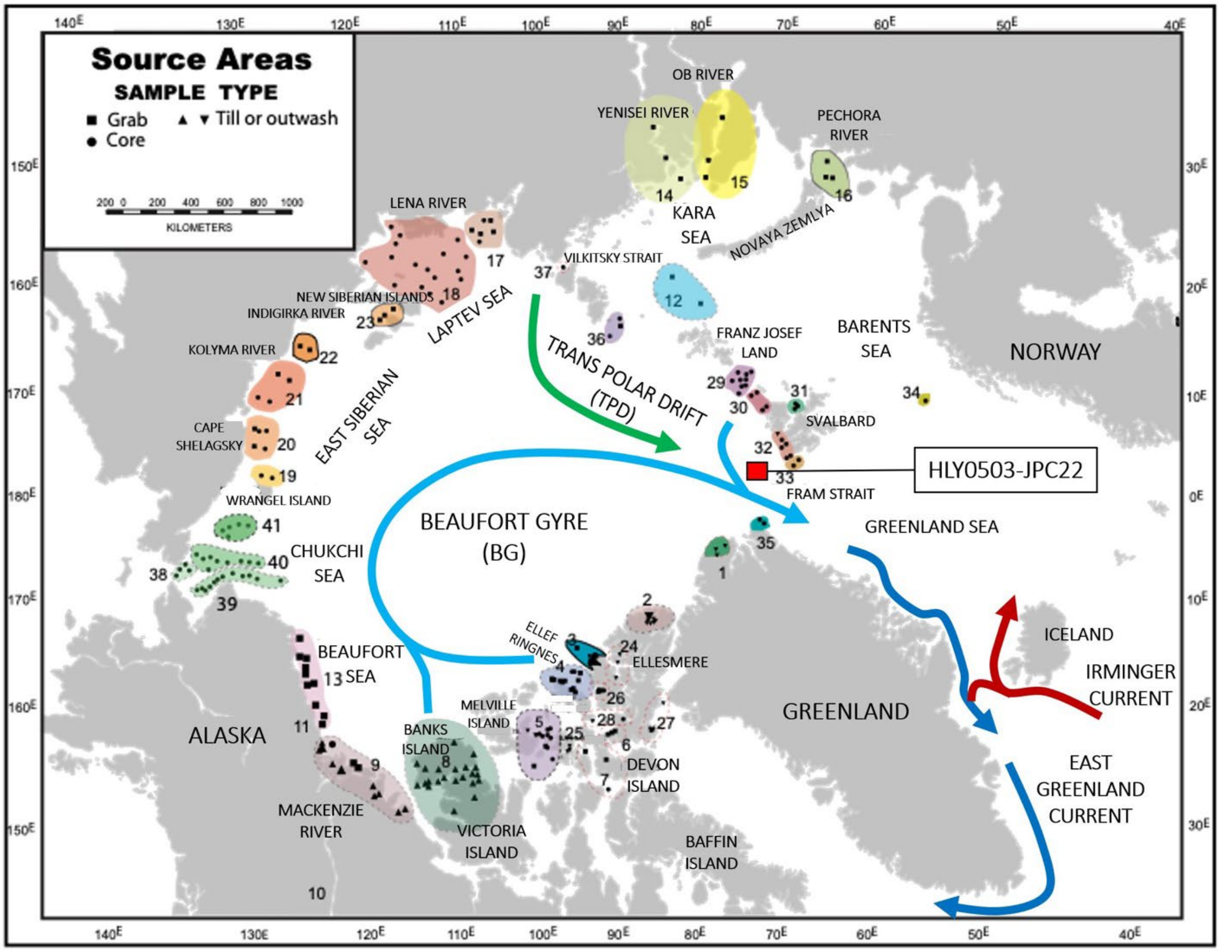

Fig. 2. Forty-one circumarctic SAs for Fe-grains matching. Each individual SA was developed and synthesized from numerous representative samples. Map shows JPC22 (yellow diamond), prominent surface Arctic Ocean currents including the Transpolar Drift (green arrow), Beaufort Gyre (blue arrow), East Greenland Current (dark blue arrows), and Irminger Current (red arrows) (After Darby et al. 2015).

IRD can range from clay-size particles to larger drop stones, depending on the origin of the ice. Most deep-sea Arctic sediments are mud (fine-grained) to sand-sized grains, with abundant clays and silts and occasional drop stones. This study focuses on sand-sized Fe-grains (45-250 μm). The JPC22 sediment core was collected using a vessel-based jumbo piston. The Byrd Polar

Institute provided sediment samples from the archived sediment core at 1-cm intervals throughout glacial maxima MIS 2, 4, and 6. Samples were subdivided into four size fractions (<45 µm, 45-63 µm, 65-250 µm, and >250 µm) by wet sieving.

After the four size fractions were individually dried and weighed, Fe-grain were magnetically separated from the 45-63 µm, 65-250 µm, and >250 µm intervals, and analyzed for their elemental compositions, or "chemical fingerprint". Darby et al. (2015) constructed an extensive Circum-Arctic SA database by analyzing the elemental composition of >38,000 Fe-grains from 41 unique SAs around the Arctic margins (Fig. 2). These Circum-Arctic SAs are defined by differences in point counts of the >250 µm mineral grain and rock fragments (Darby and Bischof, 1996). This database provides a reliable catalogue of unique Fe-grain chemical fingerprints associated with each SA. In this study, chemical fingerprints provide a proxy for Arctic Ocean ice movement during glacial periods by connecting Fe-grains deposited at the JPC22 site to their original SAs. The Fe-grain provenance method has a high statistical accuracy with incorrect matches accounting for <2 % of Fe-grains (Darby et al., 2015).

3.1.1 METHODOLOGY CONSIDERATIONS

In general, Arctic Ocean sediments have minimal diagenetic effects (Darby et al., 2015). Cold water slows or prevents most diagenesis on the timescale of this study (<1 Myr). Furthermore, the lack of evidence for bioturbation suggests minimal intermixing of sediment layers, which increases the reliability of sediment layer dates. Since this study's sediment core was collected at a water depth of 798 m, sediment does not risk much disturbance from wind driven waves, storms, or tidal influences. However, currents can still winnow melt-out IRD while it settles to the sea floor, thus removing valuable fine-grained IRD in a region characterized by low sedimentation rates.

3.2 AGE MODEL

An age model was developed for JPC22, which provides calculated ages associated with each core depth based on secondary data or a proxy. This section describes the process to develop the age model, data, calculations, and lists a few considerations for using the age model.

3.2.1 AGE MODEL DEVELOPMENT

Because JPC22 extended beyond the reliable age-range for radiocarbon dating, and due to lack of abundant forams throughout the core, radiocarbon dating is not the only method used to establish absolute dates for this core. However, two samples were selected for radiocarbon dating to serve as tie-points and corroborate the age model (Myers and Darby, 2015) (Appendix Table 8).

In their study, Xuan et al. (2011) examined JPC22 and analyzed the similarities between a K_{ARM}/K, a magnetic grain size proxy, and the LR04 benthic isotope stack data (Lisiecki and Raymo, 2005). K_{ARM}/K is a measure of the magnetic grain size where ARM is the anhysteretic remanent magnetization and K is the low-field magnetic susceptibility. Using data from grain size analysis, they concluded finer grain sizes correspond with larger K_{ARM}/K values, which occurred during interglacial periods (i.e.- higher sea levels). The authors did not find a correlation between coarser (>63 μm) magnetic grains and K_{ARM}/K, which suggested variations in K_{ARM}/K data are not caused directly by coarse IRD deposition (2011). The size differences are restricted to the silt-size magnetic minerals (<63 μm) that are affected by current winnowing. These implied changes in bottom-current velocity depending on water depth and/or detrital provenance directly related to glacial-interglacial conditions that impacted the grain size of magnetic sediments. While their study did suggest K_{ARM}/K data and the Lisiecki and Raymo (2005) LR04 benthic isotope stack could be used to develop an age model for JPC22, they indicated that they do not know the cause for the correlation. Myers and Darby (2015) and this study propose sediment winnowing is enhanced during periods of lower sea level, resulting in higher concentrations of the coarser magnetic minerals. As described in Section 2 above, lower sea level results in fewer outlets for Arctic Ocean water, thus increasing flow velocities through Fram Strait and on the shallow Yermack Plateau, increasing the potential for winnowing of fine-grained sediment.

3.2.2 AGE MODEL DATA

For this study, MIS dates are provided by the LR04 benthic isotope stack (Lisiecki and Raymo, 2005). While JPC22 sample core depths for this study are estimated to reach ages close to MIS 11 (~424 ka), based on previously dated Arctic cores and associated sedimentation rates, this study only requires age control through MIS 6, or 191 kyr. Two $\delta^{18}O$ records are available for this age model, the North Greenland Ice Core Project Oxygen Isotope Data (NGISP) and Vostok, Antarctica ice cores. While the NGISP data are closer proximity to the Arctic, Greenland ice core data only reliably extends to ~125 ka. Since JPC22 extends beyond the age limits of NGISP data, Vostok ice core data serves as an age control, with data reaching 420 ka (Petit et al., 1999). The Vostok ice core is located at the Russian Vostok station in East Antarctica (78° S, 106° E, elevation 3,488 m). To overcome any lag in the isotope records due to the geographical separation between Antarctica and the Yermack Plateau, this study uses the atmospheric $\delta^{18}O$ record. Atmospheric gases circulate the earth on a time scale of a few days, whereas water in the global oceans circulates in thousands of years. Isotope data measured from oxygen in water molecules may have a significant lag from the Arctic, which could greatly impact an age model.

3.2.3 AGE MODEL CALCULATIONS

Vostok $\delta^{18}O$ atmospheric data are compared to JPC22 K_{ARM}/K data, and peaks and troughs are manually correlated (Appendix Fig. 26 and Appendix Table 8). Distinct MIS (2, 5a, 5c, and 5e), and two ^{14}C dates from previous analyses (17.9 kyr at 100.5 cm and 21.5 kyr at 138.0 cm) from Xuan et al. (2011) help constrain the initial correlations. In the Vostok core, $\delta^{18}O$ data younger than 150 ka are higher resolution and slightly noisier than older data (Petit et al., 1999). To overcome the noise inherent in the high-resolution data between 0-150.0 kyr, raw Vostok $\delta^{18}O$ data are smoothed using a 4.0-kyr boxcar filter (Fig. 7). For younger ages (shallower core depths), JPC22 K_{ARM}/K data are correlated to the 4.0 kyr smoothed line. All data >150.0 kyr are matched directly from JPC22 K_{ARM}/K to $\delta^{18}O$ raw data. The correlations provide a list of "picks" – tie-points between troughs and peaks in JPC22 K_{ARM}/K and $\delta^{18}O$ data (Appendix Table 8).

Manually selected picks are interpolated using a Piecewise Cubic Hermite Interpolating Polynomial (PCHIP) in MATLAB, which calculates ages for all core depths (Appendix Fig. 27, Appendix Fig. 28, and Appendix Fig. 29). Tails in interpolated data at the top of the core (core depths 0.5-8.5 cm) are addressed using sedimentation rates and will be discussed in Section 3.6.1.

3.2.4 AGE MODEL CONSIDERATIONS

Xuan et al. (2011) point out their method may not be reliable for sediments older than MIS 6. K_{ARM}/K data >MIS 6 are included so the entire dataset is visible during the manual matching picks. Since K_{ARM}/K were not independently dated, the dataset could not be arbitrarily truncated. This interpolation method makes no assumptions of data outside the bounds of what is known. Likewise, this interpolating process does consider any of the processes that produce the data used; therefore, there is no measure of uncertainty within the model. Standard error must be assumed from the data used. For this study, input data are the matching picks from the atmospheric $\delta^{18}O$ Vostok data. Petit et al. (1999) state their dating accuracy is better than ±10 kyr for most of the ice core record, and better than ±5 kyr for the last 110.0 kyr. Their accuracy never exceeds ±15 kyr. For comparison, accuracy of the LR04 benthic stack is ±4 kyr from 0-1 Ma (Lisiecki and Raymo, 2005).

3.3 SEDIMENTATION RATES

Sedimentation rates (also known as depositional rates) for MIS 2, 4, and 6 are calculated using the calculated ages from the age model. Sedimentation rates throughout the core (Appendix Table 9) support age model development, and identify periods of high sedimentation rates, as well as low rates, and depositional hiatuses. Sedimentation rates are calculated by dividing differences in adjacent initial and secondary depths (cm) by the differences in their respective initial and secondary ages (kyr). "Time per cm" is also calculated by dividing differences in calculated ages (kyr) by differences in adjacent depths (cm).

$$\text{Sedimentation (Depositional) Rate} = (D1 - D2) / (A1 - A2) \tag{1}$$

$$\text{Time per cm} = (A1-A2) / (D1-D2) \tag{2}$$

where: D1 = Initial Core Depth (cm)

A1 = Initial Age (kyr)

D2 = Secondary Core Depth (cm)

A2 = Secondary Age (kyr)

3.3.1 SEDIMENTATION RATE CONSIDERATIONS

As described above, the PCHIP interpolation method results in a slight tail at the top of the core (0.5-8.5 cm). To address the data tail, MIS 1 sedimentation rates were calculated the average time per interval (0.1 kyr/cm; Appendix Table 10) and adjust the PCHIP calculated ages within the data tail accordingly.

3.3.2 HIATUS CALCULATIONS

An important dynamic captured in this study is the presence of hiatuses in Fe-grain deposition. This occurs when IRD (including Fe-grains) is not deposited, either due a blockage in ice transport, or a lack of melt out. This study defines a hiatus is as an interval with <2 Fe-grains matched per 10g bulk sample weight. Hiatus durations (kyr) are calculated by subtracting adjacent interval calculated ages. Some hiatus intervals are bound by missing samples (identified by "NaN" in (Cofield, 2023a), which may increase the error on the starting and ending dates of specific hiatuses. In some cases, particularly during MIS 6, multiple hiatuses are bound or interrupted by single missing samples. It is possible missing samples are part of the overall hiatus, and actual hiatuses time periods are slightly longer than this study resolved.

3.4 SAMPLE SOURCES

The marine sediment core, JPC22, was chosen because it includes sediment older than MIS 6 and has portions of age models based on a magnetic grain size proxy and oxygen isotope data (Xuan et al., 2012; Myers and Darby, 2015). The core was collected from the Yermak Plateau in Fram Strait, 80º 29.386'N, 007º 46.141'E at 798 m water depth (Figs. 1 and 2), during the Healy-Oden Trans-Arctic Expedition (HOTRAX) 2005. When sea levels drop >150 m during glacial intervals, the Fram Strait becomes the only connection between the Arctic Ocean and the sub-polar oceans, making this an ideal location to capture ice flows exiting from the Arctic Ocean in both glacial and interglacial intervals. One-cm-thick samples were obtained at one-cm intervals from JPC22, based on estimated depths for MIS 2, 4, and 6, with a few exceptions due to lack of core material. Each 1-cm-thick bulk sample contained at least 5 g (dry weight) sediment.

3.5 SAMPLE PROCESSING

This section outlines the entire bulk-sediment sample processing routine, including Fe-grain extraction and analysis, foram abundance estimates, and a separate SEM test on two quartz grain samples.

3.6 FE-GRAINS

All Fe-grains were extracted from bulk samples through wet-sieving and magnetic separation before being analyzed for chemical composition with an electron microprobe.

3.6.1 PREPARATION AND WET SIEVING

Sample preparation, processing, and analysis followed standard methods described in Darby et al. (2015) and Folk (1980) and summarized in Fig. 3. In brief, bulk samples were freeze-dried and weighed, then wet-sieved using mesh screens with apertures of 45 µm, 63 µm, and 250 µm. These specific sieve intervals were selected to: (1) enhance magnetic separation; (2) capture sediment fractions that separate sea ice transport (45-63 µm) from glacial ice transport (>250 µm); and (3) further subdivide fine sand (63-250 µm) and coarse sand (>250 µm). The partitioned samples (45-63 µm, 63-250 µm and >250 µm) are dried at 95° C. The <45 µm fraction are dried at 45° C to prevent clay transformation for any future analysis and archived.

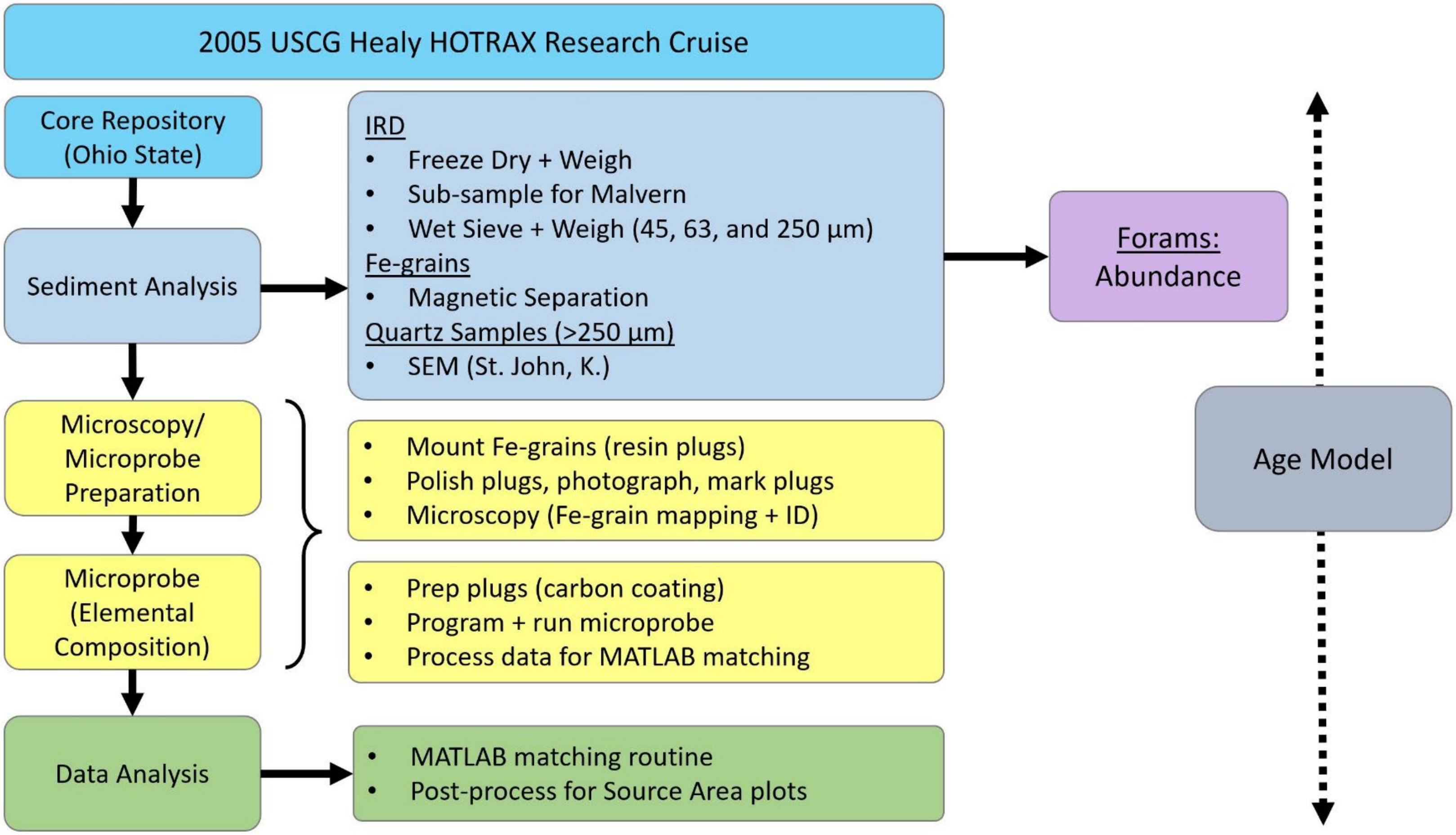

Fig. 3. Flow chart for sample processing, sample analysis, and data processing.

3.6.2 MAGNETIC SEPARATION

To isolate Fe-grains from the 45-63 µm and 63-250 µm subsamples, samples were processed with a hand magnet, then electromagnetic. Some Fe-grains, such as magnetite, were easily removed by a hand-magnet. Other Fe-grains required a Frantz electro-magnetic separator. All non-magnetic grains were archived in their vials.

After extraction, all 45-63 µm and 63-250 µm magnetic grains from all size fractions were combined into one representative sample for each core depth interval. Magnetic separation isolated the Fe-grains required for this study, but also extracted other magnetic minerals, primarily quartz grains with magnetic mineral inclusions. These quartz grains are not ideal for this study's provenance method as the magnetic mineral inclusions may not represent the original SAs. Therefore, it was important to recognize their presence and address them in the upcoming microscopy preparation.

3.6.3 PREPARATION FOR ELECTRON MICROPROBE ANALYSIS

Samples were mounted in epoxy plugs, polished, and marked for electron microprobe analysis. Each plug contained samples from four depth intervals, and was hand marked to provide a series of etched symbols (i.e., interval identification, arrows, and flags for IRD) in the resin as a spatial guidance under microscopy high-power. After marking, plugs were photographed under a 10x or 40x optic, and photographs were manually "mapped" by identifying Fe-grains using optical microscopy (Appendix Fig. 25). During mapping, individual Fe-grains were identified and numbered on photographs in the order they would be programmed for electron microprobe analysis. This step not only streamlines the programming process, but it assists navigation under high-power field of vision on the microprobe. The lens was immersed in an oil with the refractive index of quartz to avoid inadvertently mapping the quartz grains with magnetic inclusions. For each interval, all Fe-grains were counted with a maximum of 100 grains identified for microprobe analysis. In cases where the total number of Fe-grains exceeded 100, this study developed a “multiplication factor” based on the total possible number of Fe-grains that could have been analyzed. For example, an interval with 100 grains had a multiplication factor of x1.0, and an interval with 175 grains had a multiplication factor of x1.75. The multiplication factor was applied to matched grain numbers for each SAs. After optical microscopy, the plugs were cleaned with soap and water and alcohol, then dried. All photograph hardcopies were archived by core depth.

Cleaned resin plugs were coated with a thin layer of carbon in a vacuum evaporator prior to microprobe analysis to prevent the electron beam from “charging” across the plug surface, which would interfere with the results.

3.6.4 ELECTRON MICROPROBE ANALYSIS

Carbon-coated epoxy plugs were analyzed for elemental composition using the Cameca SX100 electron microprobe. Each Fe-grain analysis was programmed into the electron microprobe software using the “mapped” photographs. The microprobe could analyze up to 6 epoxy plugs, with a total of 24 samples or ~2,400 Fe-grains. Once programmed, the electron microprobe automatically analyzed the elemental composition of each Fe-grain by measuring the amount of Ti, Fe, Mn, Mg, Si, Al, Cr, Zn, V, Ca, Zn, Nb, Ta, and O (Bence and Albee 1968; Darby, 2003).

3.6.5 FORAMINIFERA

Foram analyses were not included in the original development of this study. However, some intervals deeper in the core revealed intervals filled with forams. Unfortunately, this was discovered after most IRD samples were fully processed (through magnetic separation) and archived in their vials, so this study only provides a qualitative representation of abundances. Foram abundances were estimated by visually inspecting fully processed IRD sample, in their vials, under a microscope. The estimated fraction of forams in each sample was established and scored according to the following scale:

0- Absent (0%)
1- Low/Absent (1<5%)
2- Low (<5-25%)
3- Moderate/Low (25-50%)
4- Moderate (50%)
5- Moderate/High (50-75%)
6- High (75-90%)
7- Very High (>90%)

Sediment processing did not alter or dissolve the calcium carbonate foram tests, and they were archived in their respective size fraction vials.

3.6.6 SEM QUARTZ GRAINS ANALYSIS

Two >250 µm samples were selected for SEM analysis. One sample was from the estimated MIS 2 termination (44.5 cm; ~8.5 ka) and the second sample was from the estimated MIS 2 peak (83.5 cm; ~15 ka). These two intervals were selected because they represent the most recent examples of drastically different glacial episodes during MIS 1 and 2 and could help distinguish between glacial and sea ice transport. Kristen St. John, James Madison University, Harrisonburg, Virginia, conducted the SEM analysis of quartz grains.

3.7 DATA PROCESSING

This section outlines all data synthesized in a master database, and the data processing steps for the electron microprobe data, and MATLAB matching routine data.

3.7.1 SEDIMENT SAMPLE DATABASE

Bulk samples and sample processing data are archived in a master database including core depth, freeze-dried bulk sediment weight, and dry weights for sieved intervals (Cofield, 2023b). In addition to these sediment parameters, the master file contains the interpreted age model developed for this study, and all final processed microprobe data.

3.7.1.1 ELECTRON MICROPROBE DATA

Unprocessed microprobe data are downloaded directly from the Cameca software, and assigned appropriate metadata (core name, core depth interval, and grain number). Each analyzed Fe-grain is assigned a mineral number based on the following refined Titanium (Ti %) or Chromium (Cr %) parameters from the optical minerology parameters (Appendix Fig. 25):

Mineral 0 (fresh ilmenite) = 24% < Ti < 34%
Mineral 1 (altered ilmenite) = Ti > 34%
Mineral 2 (titanomagnetite) = 1%< Ti < 24%
Mineral 6 (Magnetite) = Ti < 1%
Mineral 8 = Cr > 6%
Mineral 9 = all other Fe-grains outside criteria for Min 0-Min 9

Mineral coding for this study followed mineral coding criteria for the SA dataset (Darby et al., 2015)

3.7.2 MATLAB MATCHING ROUTINE

The MATLAB matching routine consists of a set of four scripts, developed for Darby et al. (2015) that match each analyzed Fe-grain from the microprobe data to the entire SA dataset (Cofield, 2023c). There are two primary input files for the matching routine: the microprobe dataset with elemental compositions for each grain and the master SA database. This study only matches SAs 1-41 (Fig. 2), so the input file is truncated after SA 41 so as to match only sources within the Arctic Ocean. Prior to matching, microprobe data are normalized, all data artifacts or missing (non-sampled) intervals are replaced with a “NaN”, and elements are arranged in the following order: Ti, Fe, Mn, Mg, Si, Al, Cr, Zn, V, Ca, Nb, Ta, Ni, and O.

The methodology has a 1.5 % match error at 2 standard deviations (i.e., 1.5 Fe-grains out of 100 Fe-grains), and only increases to 1.9 % match error at 4 standard deviations. Standard deviations are based on 30-130 replicate analyses for each element (total = 360 replicates). In this study, all Figures which show Fe-grains that have been matched to their SAs using the MATLAB process include a threshold line showing samples with <2 grains matched per 10 g bulk sample weight to account for the 1.9 % match error, or ~2 grains for 100 grains analyzed at each cored depth. (Cofield, 2023c) highlights the depths and calculated ages where total matched grains are <2 grains per 10g bulk sample weight.

To address issues associated with oxygen detection during microprobe analysis, the standard deviation for oxygen is set to a value that prevents it from impacting the MATLAB matching routine. Also, the SA dataset and core dataset are normalized so that each grain analysis summed to 100 %. Oxygen is abundant in Fe-oxides and did not serve as a unique identifying element for provenance determination. Because increasing the matching range to three (3) standard deviations may improve the range of matches with minimal impact on the average match error (Darby et al., 2015), this study matches all Fe-grains at 3 standard deviations. The output file from the matching routine lists each grain per core depth interval, and what portion (fraction) matches to any and/ or all 41 SAs.

The final post-processed database lists the summation of all grains per each depth interval with the number of grains that matched to each of the 41 SAs. The previously calculated “multiplication factor” is applied to all intervals with >100 possible Fe-grains mapped on the photographs.

CHAPTER 4

RESULTS

4.1 RESULTS OVERVIEW

This section provides results from the age model development, sedimentation rates, grain size analysis, foram abundances, SEM quartz grain analysis, and the Fe-grain matching using the provenance method.

4.2 AGE MODEL

Troughs and peaks with similar features (i.e., distribution, fluctuations, and overall shape, such as bimodal) are matched between K_{ARM}/K and Vostok $\delta^{18}O$ data from MIS 1 to MIS 6 (Appendix Fig. 26 and Appendix Table 8). The goal was to match as many similar features as possible throughout both data sets to minimize the bias introduced when developing an age model based on extremes, such as only major peaks and troughs (Jakobsson et al., 2014b). This study's age model (Fig. 4) further supports Xuan et al.'s (2011) previous use of K_{ARM}/K to develop an age model. They suggested an uncertainty in their method after MIS 5, but this study's age model supports the hypothesis of a relationship between K_{ARM}/K and the Vostok $\delta^{18}O$ data during MIS 6. Figure 4 values are plotted as individual data points with a connecting line, thus conveying the high-resolution sampling for this study. The JPC22 age model captures similar characteristics in the K_{ARM}/K data, such as low K_{ARM}/K values during glacial periods (coarser magnetic minerals), and multiple troughs and peaks specifically during MIS 6 (Fig. 5). The offset(s) between K_{ARM}/K and Vostok $\delta^{18}O$ may be a result of differences between JPC22 sedimentation rates compared to ice accumulation rates at the Vostok Ice core location (Fig. 6).

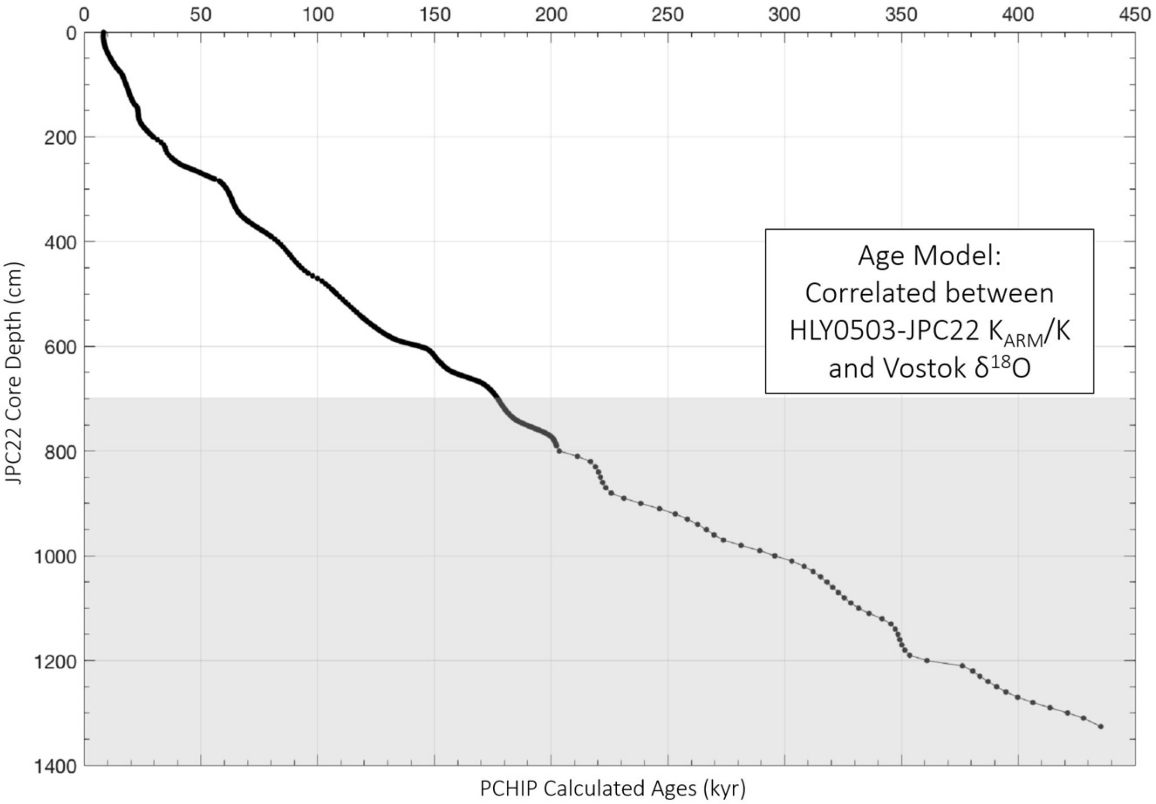

Fig. 4. JPC22 core depths (cm) and PCHIP calculated ages (ka) from PCHIP interpolation. JPC22 age model seems most reliable through MIS 6 (<753.5 cm core depth), with data beyond MIS 6 reliability shaded in gray.

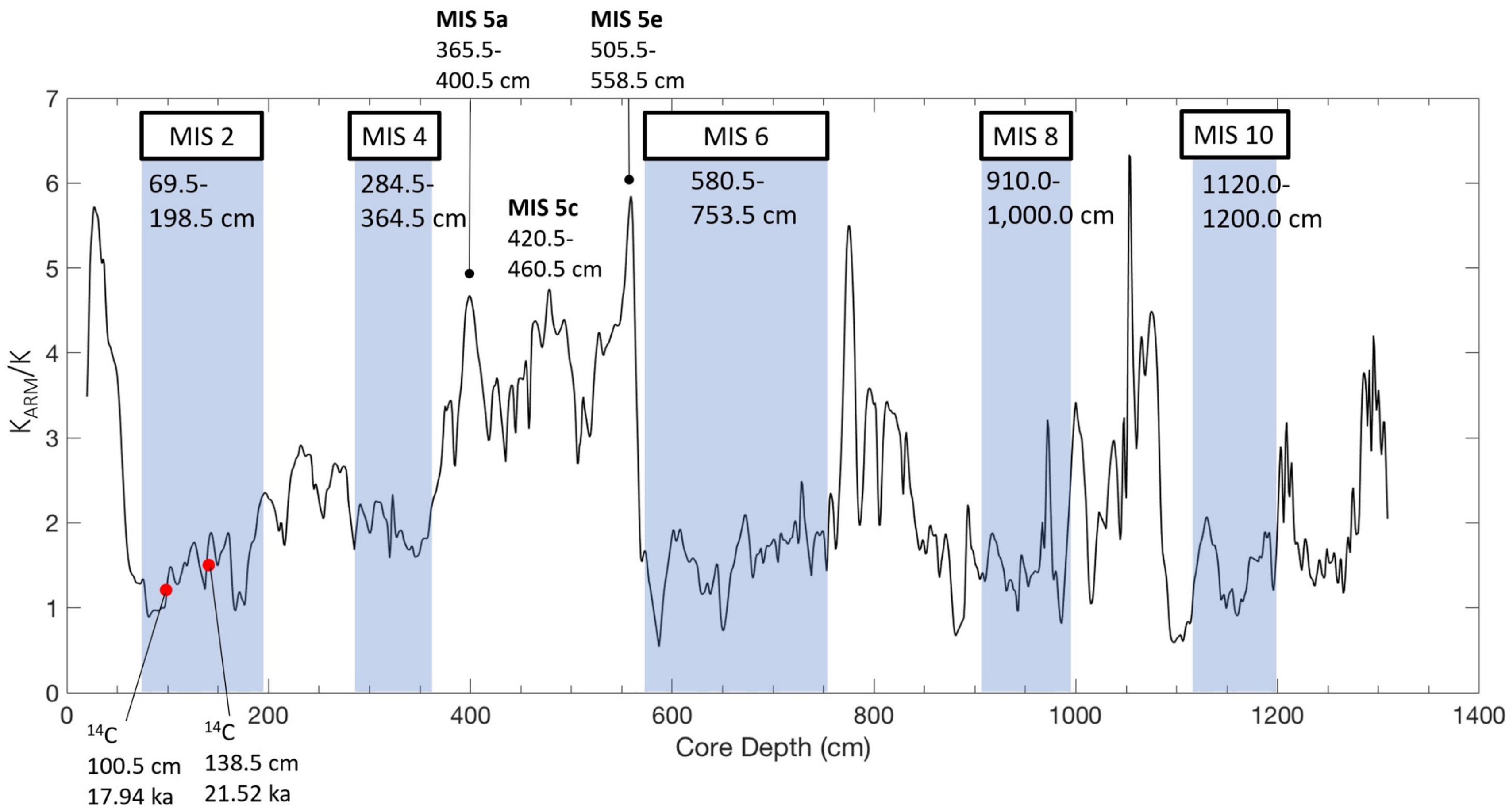

Fig. 5. JPC22 age model applied to K_{ARM}/K. Figure shows Xuan et al. (2011) K_{ARM}/K and previously analyzed ^{14}C dates (red dots).

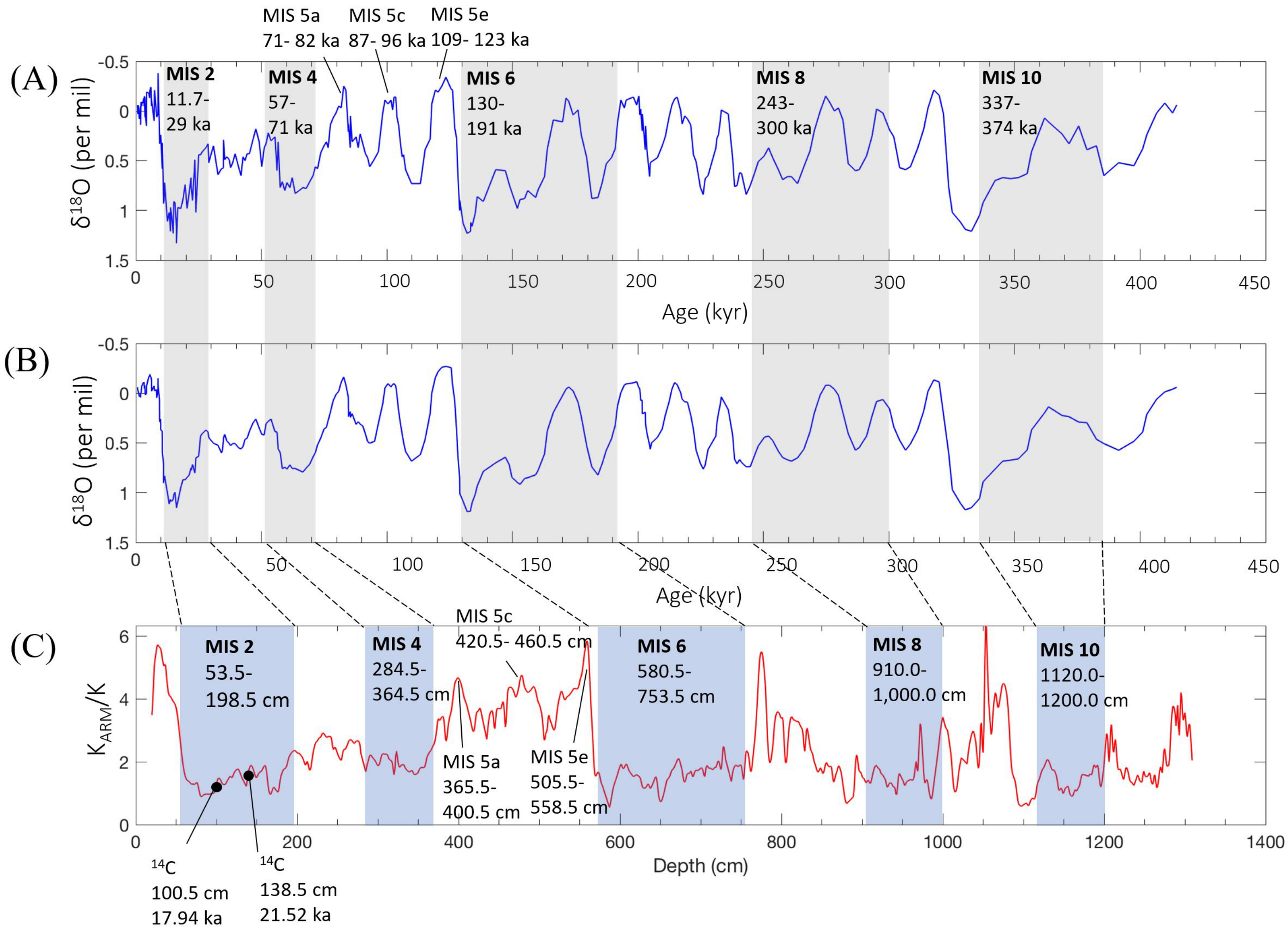

Fig. 6. Comparison between K_{ARM}/K with PCHIP calculated ages and Vostok $\delta^{18}O$ data. A) Vostok $\delta^{18}O$, B) Vostok $\delta^{18}O$ 4-kyr smoothed, and C) JPC22 K_{ARM}/K with previously analyzed ^{14}C dates (Xuan et al., 2011).

4.3 SEDIMENTATION RATES

Multiple sedimentation rates for MIS 2, 4, and 6 are calculated based on slope changes in the age model, allowing average sedimentation rate calculations for each stage (Figs. 7, 8, and 9). During MIS 2, sedimentation rates reach 25.6 cm/kyr from 22.8 to 23.7 ka (0.9 kyr). However, this high sedimentation rate is not associated with MIS 2 initiation or termination. The mean sedimentation rate during MIS 2 is 11.6 cm/kyr. For comparison, the average sedimentation rate during MIS 1 is 12.4 cm/kyr. During MIS 4, the average sedimentation rate is 7.0 cm/kyr, with the highest rate during the middle of the stage at 9.2 cm/kyr from 61.4 to 65.6 ka (4.2 kyr). MIS 6 has an average rate of 3.8 cm/kyr, and no sedimentation rates exceed 6 cm/kyr in this stage.

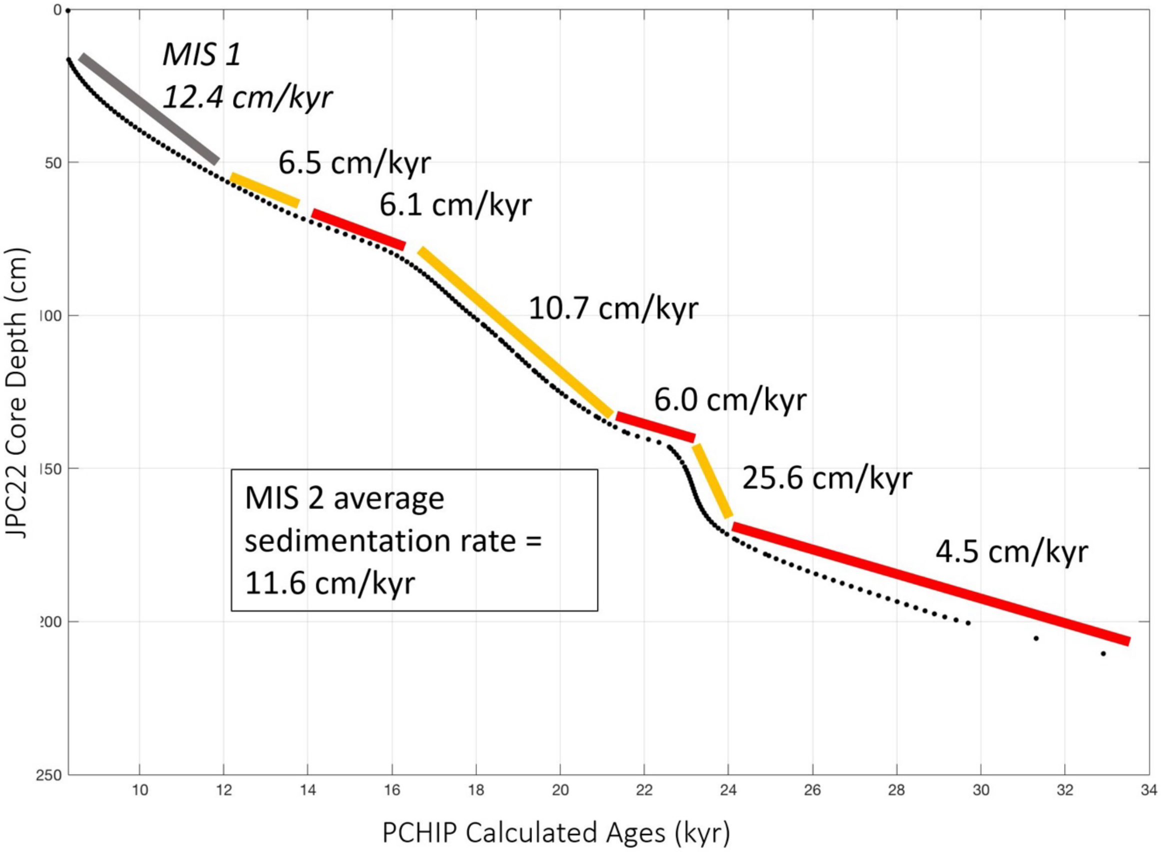

Fig. 7. JPC22 sedimentation rates during MIS 2. Appendix Table 9 lists all individual slope sedimentation rate calculations fluctuating between lower (orange lines) and higher (red lines) rates (Table 1). While MIS 1 (gray) was not included in this study, the sedimentation rate is provided as a comparison to modern rates. Values are plotted as individual data points.

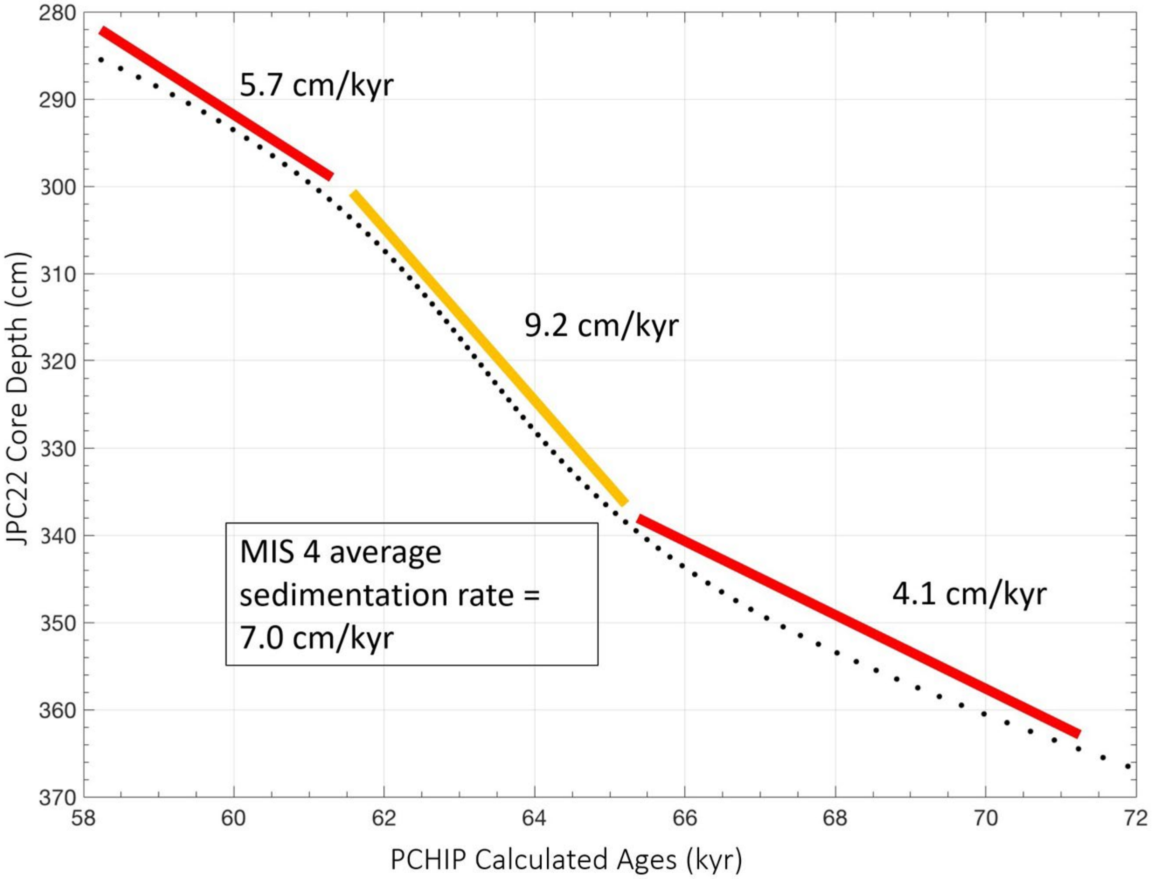

Fig. 8. JPC22 sedimentation rates during MIS 4. Appendix Table 9 lists all individual slope sedimentation rate calculations fluctuating between lower (orange lines) and higher (red lines) rates (Table 1). Values are plotted as individual data points.

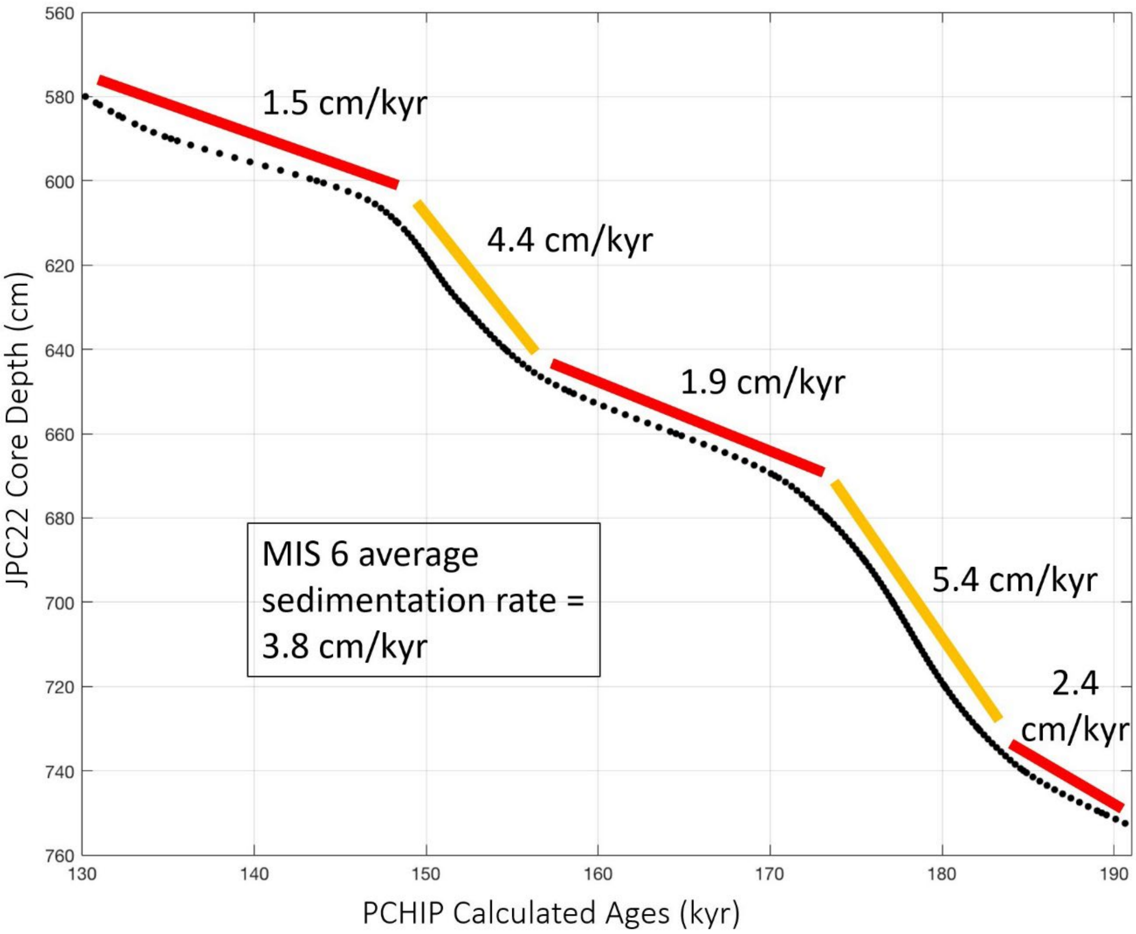

Fig. 9. JPC22 sedimentation rates during MIS 4. Appendix Table 9 lists all individual slope sedimentation rate calculations fluctuating between lower (orange lines) and higher (red lines) rates (Table 1). Values are plotted as individual data points.

Table 1. Sedimentation rates during MIS 1-11.

MIS	**Core Depth Interval**	**Average Depositional Rate**	**Average Time per cm**
	(cm)	**(cm/kyr)**	**(kyr)**
1	0-52.5	18.2	0.1
2	53.5-198.5	11.6	0.1
3	199.5-280.5	3.1	0.4
4	284.5-364.5	7.0	0.2
5a	365.5-400.5	3.0	0.3
5c	420.5-460.5	4.8	0.2
5e	505.5-579.5	3.4	0.3
6	580.5-753.5	3.8	0.4
7	754.5-900.0	5.5	0.3
8	910.0-1000.0	1.9	0.6
9	1010.0-1110.0	3.1	0.4
10	1120.0-1200.0	6.3	0.3
11	1210.0-1300.0	2.1	0.6

4.4 GRAIN SIZE ANALYSIS

Grain size analysis is conducted by wet sieving 708 bulk sediment samples into four size fractions.

4.4.1 IRD GRAIN SIZE DISTRIBUTION

Wet sieve analysis provides total IRD weight (g) in the intervals 45-63 µm, 63-250 µm, and >250 µm (Fig. 10). While bulk IRD data do not reflect any particular SA, they provide information related to IRD deposition in Fram Strait, such as presence or absence of IRD deposition, number of grains, and size fractions. IRD from all size fractions show a peak (23.3 ka or 23.5 ka) following the initiation of MIS 2, with the most prominent of the size fractions being 63-250 µm. Throughout MIS 2, 63-250 µm shows multiple, smaller IRD peaks. Coarser IRD (>63 µm), especially >250 µm, show low numbers through MIS 2 until a small peak at 17.2 ka, and a final peak at 13.4ka just before the termination of MIS 2. The remaining peaks in MIS 2 are dominated by finer-grained IRD (<63 µm). All identified IRD peaks during MIS 2 occur during periods of high sedimentation rates. The only IRD peak observed across all size fractions at the same time, 23.5 ka, occurs during the highest MIS 2 sedimentation rate (25.6 cm/kyr).

During MIS 4, IRD is >63 µm at initiation. While finer IRD remains low throughout MIS 4, >63 µm IRD show a peak during the middle of the stage at ~63.7 ka, coinciding with high sedimentation rates of 9.2 cm/kyr. IRD do not show distinct peaks at MIS 4 termination.

During MIS 6, the dominant peak occurs at 175.6 ka, with a smaller peak at 169.1 ka, both during a relatively high sedimentation rate period for MIS 6 (5.4 cm/kyr). There is a corresponding, yet smaller, fine IRD peak at 175.6 ka. During the middle of MIS 6, IRD peaks are dominated by grains in the 63-250 µm size class.

Sedimentation rates are low during MIS 6, with the highest rates ranging from 4.4 to 5.4 cm/kyr (Fig. 9). Interestingly, the largest MIS 6 IRD (>250 µm) peak occurs at 166.1 ka during a period of extremely low sedimentation (1.9 cm/kyr). A higher sedimentation period (4.4 cm/kyr) from 155.9 ka to 172.1 ka corresponds with a series of IRD peaks. There is a >250 µm IRD peak at 152.3 ka, a series of smaller fine IRD peaks at 155.6 ka, and 63-250 µm IRD peak at 156.3 ka and 152.8 ka, reaching nearly 40 weight percent. Sedimentation rates are much lower during MIS 6 than MIS 2 or 4, with the highest rates only ranging from 4.4 to 5.4 cm/kyr. While the 152.3 ka IRD peak occurs during a higher sedimentation period (4.4cm/kyr), the 166.1 ka IRD peak occurs during a period of low sedimentation rates (1.9 cm/kyr). Between ~152 ka and 133 ka, IRD melt-out is low or absent. Prior to MIS 6 termination, there is a 63-250 µm IRD peak at 133.6 ka, with minor IRD peak in the finer and coarser fractions. While MIS 5 is not the focus of this study, the 63-250 µm IRD peak at ~125 ka might be part of the disintegration of the MIS6 ice sheets. During MIS 6, IRD are dominated by the 63-250 µm fraction, however finer and coarser IRD are not entirely absent.

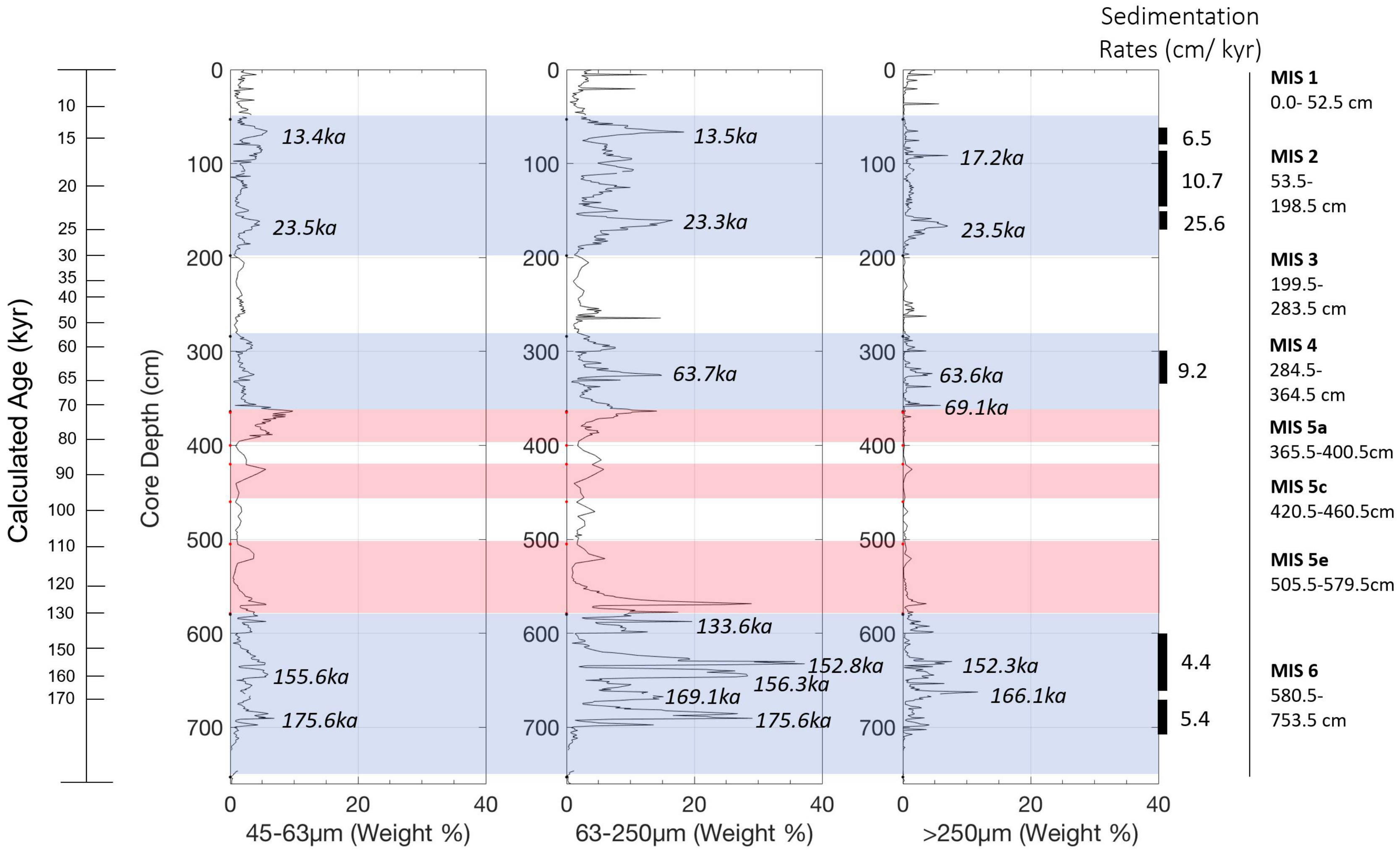

Fig. 10. IRD weight percent from wet sieve grain size analysis. Figure includes high sedimentation rates (black bars with associated rates) from Figs. 7, 8, and 9, MIS 2, 4, and 6 (blue shaded), and MIS 5a, c, and e (red shaded).

4.5 FORAMINIFERA ABUNDANCE

Adult forams (63-250 µm and >250 µm) show peaks in abundance just after MIS 2 at 25.5 ka (Fig. 11). Abundances decrease before a series of peaks at 22.4 ka and 17.9 ka, with moderate peaks in-between. At 17.9 ka, all >63 µm forams decrease until MIS 2 termination. Juvenile forams (45 µm to 63 µm) are not abundant during most of MIS 2, with some minor peaks at 19.7 ka (Fig. 11). During MIS 4, adult foram abundance peaks after initiation of this stage at 65.5 ka, but rapidly decreases, while juvenile abundances are low throughout. At MIS 6 initiation, we see peaks in >63 µm forams at 190.6 ka. Following an extended hiatus, >63 µm forams peak again at between 160.9 ka to 162.2 ka, before decreasing again. At 150.9 ka, there are multiple large peaks in >63 µm foram abundance. At the same time, 45-63 µm forams slightly increase, but only show a peak at 23.5 ka.

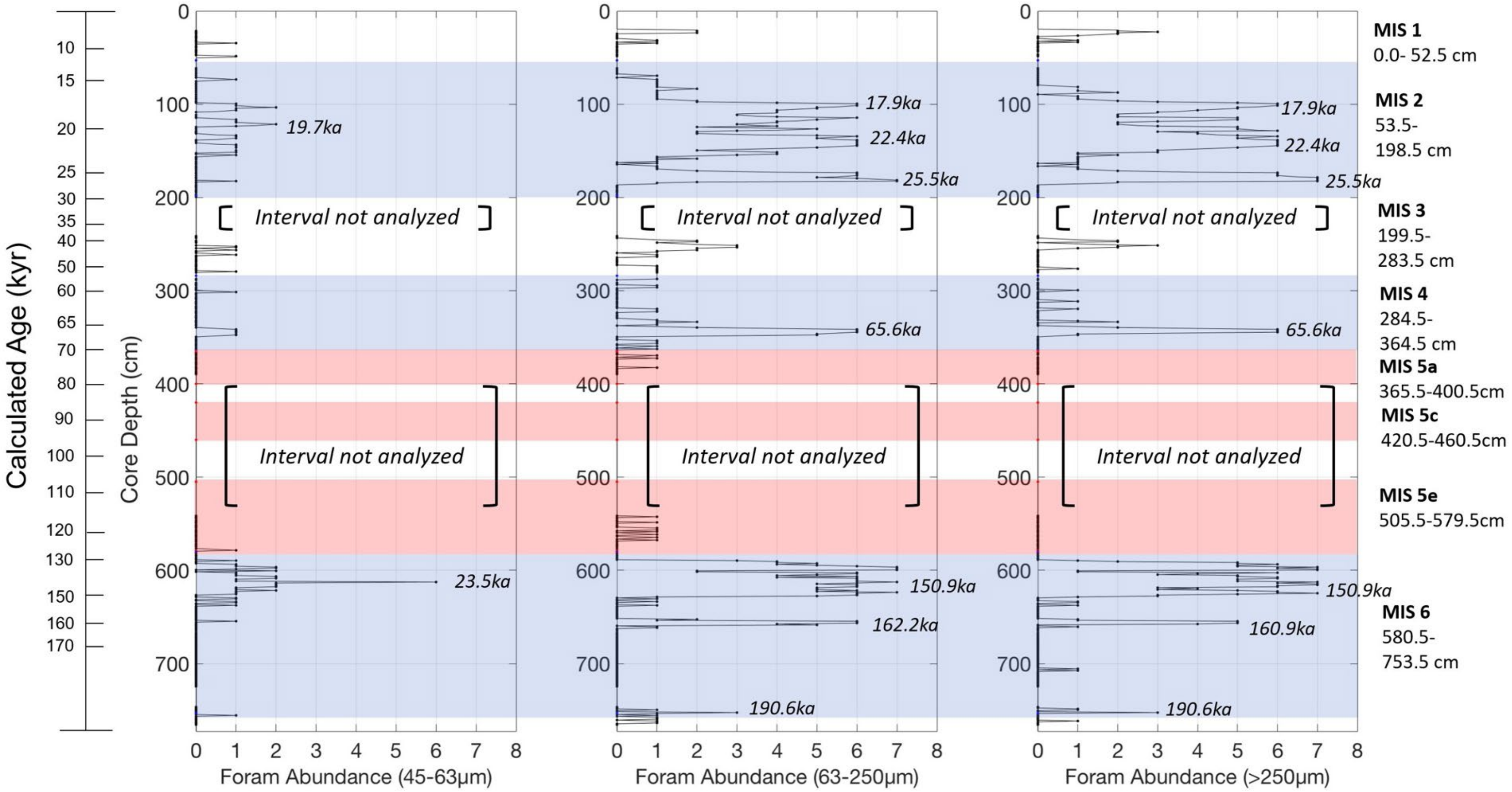

Fig. 11. Foram abundances based on estimated percent of forams in each IRD sample. Foram abundances are: 0 (Absent 0%), 1 (Low/ Absent 1-4%), 2 (Low 5-24%), 3 (Low/ Moderate 25-49%), 4 (Moderate 50%), 5 (Moderate/ High 51-74%), 6 (High 75-89%), and 7 (Very High >90%). Forams are plotted as points with 2-cm boxcar smoothed black line.

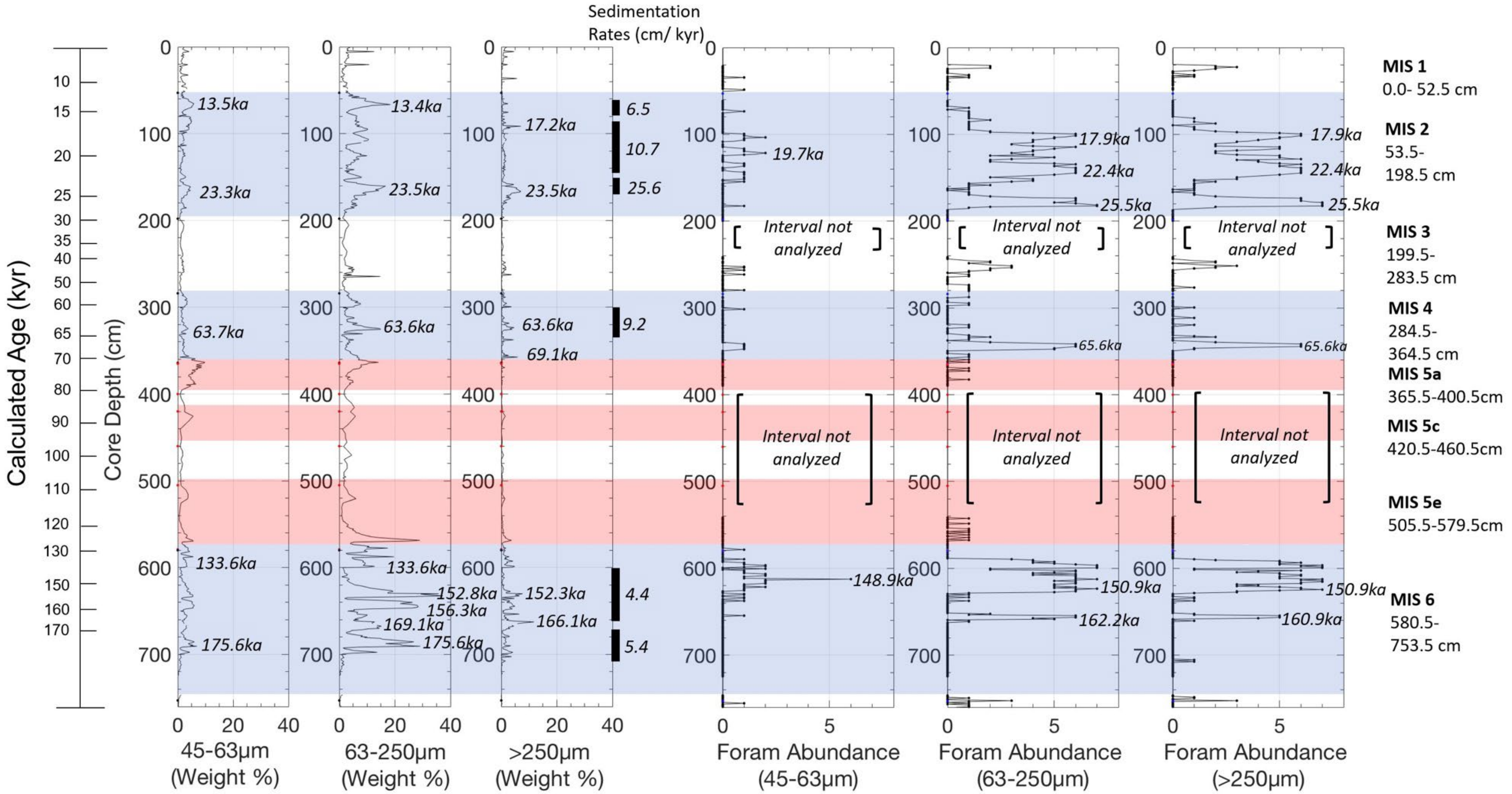

Fig. 12. Foram abundances and IRD weight percentages. Foram abundances (from Fig. 11) combined with IRD weight percentages (from Fig. 10), and high sedimentation rates (black bars with associated rates) from Figs. 7, 8, and 9.

During MIS 2, forams are relatively abundant during the middle of MIS 2. Foram peaks at 23.3 ka correspond to high sedimentation rates but lack corresponding IRD peaks. Near MIS 2 termination, the 13.5 ka IRD peaks occur in the absence of any foram peaks. During MIS 4, >63 µm foram peaks around 65.6 ka precede all IRD peaks starting at 63.7 ka and do not occur during periods of high sedimentation.

During MIS 6, there are several peaks in 45-250 µm IRD with no corresponding increase in foram abundance. Forams >63 µm peak between 160.9 ka and 162.2 ka followed by a rapid decrease. A series of high foram abundance peaks starting at 150.9 ka, corresponding with the beginning of a period of high sedimentation, is preceded by a peak in 63-250 µm IRD peak at 152.8 ka, with a minor >250 IRD peak at 152.3 ka. After 150.5 ka, forams abundances remain high and only decrease before MIS 6 termination. Juvenile forams show smaller peaks during this high abundance period, with only one major peak at 148.9 ka.

4.6 SEM QUARTZ GRAINS ANALYSIS

SEM analysis of surface features on a >250 µm quartz grain from 44.5 cm (based on initial estimate for MIS 2 termination) indicates primarily sea-ice transport influences with some glacial ice transport influences (St. John, 2023) (Personal communication with St. John). A second quartz grain from 83.5 cm indicates sea ice transport influences with some glacial ice transport influences based on absent rounded grains, including surface characterizes like a shift to sub-round, sub-angular), less dissolution and micro-layering, and more fractures and gouging (St. John, 2015). Based on our calculated age model, the initial 44.5 cm (10.6 ka) sample would be ~1 kyr after MIS 2 termination and we could expect a mix of sea ice and glacial influences. The second quartz grain from 83.5 cm (16.5 ka) fell within the MIS 2 peak.

4.7 INDIVIDUAL SOURCE AREA FE-GRAIN MATCHING

All Fe-grains are matched to their individual SAs 1-41 (Fig. 13). Each Figure identifies MIS 2, MIS 4, and MIS 6 and their corresponding core depths (cm).

4.7.1 INDIVIDUAL SOURCE AREAS- MIS 2

Most of the Canadian Archipelago SAs (2-7) share similar trends of gradually increasing Fe-grains from MIS 2 initiation to a peak at ~18 ka and another peak at ~13 ka. SA 2, and SAs 25-28 either lack the ~18 ka peak or have nearly absent Fe-grain numbers. Notably, most SA 3 (N. Axel Heiberg Island) falls under the hiatus threshold set at the match error of 1.5 % or in most cases 2 Fe-grains per 10 g bulk weight. Additional Canadian Archipelago SAs (24-28) also fall below our hiatus threshold during MIS 2. Most Canadian SA Fe-grain peaks fall in the range of 10-20 Fe-grains/10 g bulk weight. On the other hand, SA 4 has three times as many Fe-grains throughout as any other Canadian SA. This source is the main outlet for the Innuitian Ice Sheet into the Arctic Ocean (Darby and Zimmerman, 2008).

Fe-grain numbers in Beaufort Sea SAs 8 and 9 rarely fall under our <2 Fe-grain threshold, except at the beginning of MIS 2. Most Beaufort SAs show Fe-grain peaks at ~25 ka, a gradual increase to a ~18 ka peak, and another peak at ~13 ka. SA 11 and 13 (Alaskan shelf) regularly fall below the 2-grain threshold, and only contribute <6 Fe-grains/10 g bulk weight throughout MIS 2. The SA 8 (Banks Island and the major outlet for Laurentide Ice) contributes over twice as many Fe-grains as SA 9. West of the Beaufort Sea, Bering Strait Sources (SA 38-40) show similar Fe-grain triple peaks (~25 ka, ~18 ka, and ~13 ka) in MIS 2.

Fe-grains from the area of Wrangel Island and the New Siberian Islands (SA 19-23) show variable numbers among SAs. SA 20 and 21 have <6 Fe-grains/10 g bulk weight during MIS 2 and regularly fall under the 2-grain threshold. However, both SAs show similar peaks during the middle of MIS 2. SAs 19 and 22 Fe-grains gradually increase after MIS 2 initiation and peak at ~22 ka and ~18 ka. The Bering Strait SAs (38-41) have similar MIS 2 trends as these SAs to the west (19-23). All Bering Strait, Wrangel Island and New Siberian Islands SAs show Fe-grain peaks near the MIS 2 initiation, at ~22 ka, ~18 ka, and 14-12 ka. SA 22 has the largest number of Fe-grains of all Wrangel Island and New Siberian Islands SAs during the middle of MIS 2 reaching >40 Fe-grains/10 g bulk weight. This SA (22) is located off the Indigirka River, which is much smaller than the Kolyma River area (SA 21), suggesting that sediment entrainment on the East Siberian shelf is not dependent on the size of the river flowing onto that shelf area.

Laptev Sea (SA 17-18) shows continuous Fe-grain transport during MIS 2, with only a few intervals in SA 17 near the MIS 2 initiation falling below the 2-grain threshold. SA 17 Fe-grains peaks at ~18 ka, however SA 18 shows multiple peaks during the middle of MIS 2, like SAs to the east, with Fe-grains >40 Fe-grains/10 g bulk weight. Both SA 17 and 18 show Fe-grain peaks at ~13 ka.

Kara Sea SA 36 and 37 Fe-grains gradually increase from MIS 2 initiation and peak at ~13 ka. However, SA 37 has an additional Fe-grain peak at ~18 ka. While SA 37 lacks the ~18-ka peak, it contributes nearly 30 Fe-grains/10 g bulk weight during the ~13 ka peak. Kara Sea (SA 12) shows no Fe-grains exceeding the 2-grain threshold during all of MIS 2.

The large rivers flowing into the Kara Sea (SA 14-16) have low Fe-grain numbers throughout MIS 2 except for Fe grain peaks at ~18 ka and ~12-14 ka, and mostly fall under our <2-grain threshold. Similar to most circum-Arctic sources, Kara Sea SAs shows a slight peak at ~18 ka and ~13 ka, near the MIS 2 termination. Except for SA 36, Kara Sea and the rivers flowing to this sea have Fe-grain numbers are much lower than other SAs.

Barents-Svalbard SAs (SA 29- 32) show >5-20 Fe-grains/10 g bulk weight throughout MIS 2. SA 32 (Franz Josef Land) contributed the largest number of Fe-grains, with peaks reaching >40 Fe-grains/10 g bulk weight. Like several previously discussed SAs, Barents-Svalbard SAs have Fe-grain peaks at ~18 ka and ~13 ka. Fe-grains from SA 34 fall under the 2-grain threshold, except for the two peaks seen across all Barents-Svalbard sources.

4.7.2 INDIVIDUAL SOURCE AREAS- MIS 4

Canadian sources did not show distinct peaks, and Fe-grains regularly fell below the 2-grain threshold. Two notable exceptions are SA 4 (the major outlet area for the IIS) with peaks exceeding 50 Fe-grains/10 g bulk weight, and to a less extent SA 5 with peaks >20 Fe-grains/10 g bulk weight. Beaufort Sea sources 11 and 12 have minimal Fe-grains, but SA 8 (the major outlet area for the LIS) shows nearly constant Fe-grains in multiple peaks exceeding 30 Fe-grains/10 g bulk weight. Bering Strait sources show variable Fe-grain numbers ranging from 5-10 Fe-grains, with a slight peak in SA 40 and 41 at ~59 ka and ~63 ka. Laptev Sea, East Laptev Sea, and Kara Sea show similar variable, but low Fe-grain numbers, and all show a similar small Fe-grain peak at ~63 ka. Barents-Svalbard sources show similar variable Fe-grains with few distinct peaks, and all lack the previously identified ~63-ka peak.

4.7.3 INDIVIDUAL SOURCE AREAS- MIS 6

Most SAs lack Fe-grain matches during the initiation of MIS 6, and several are low throughout this stage. However, almost all SAs show Fe-grain peaks at ~175 ka. Some SAs have a second peak at ~152 ka including: Canadian Archipelago (SA 2, 3), Laptev Sea (SA 18), Kolyma River shelf area (SA 21), West Svalbard SA 33, and Kara Sea (SA 36, 37). Like the MIS 6 initiation, Fe-grains are either missing or in very small numbers during the MIS 6 termination (130-150 ka), despite >63 µm IRD peaks at 134 ka and 140 ka (Figs. 10 and 12).

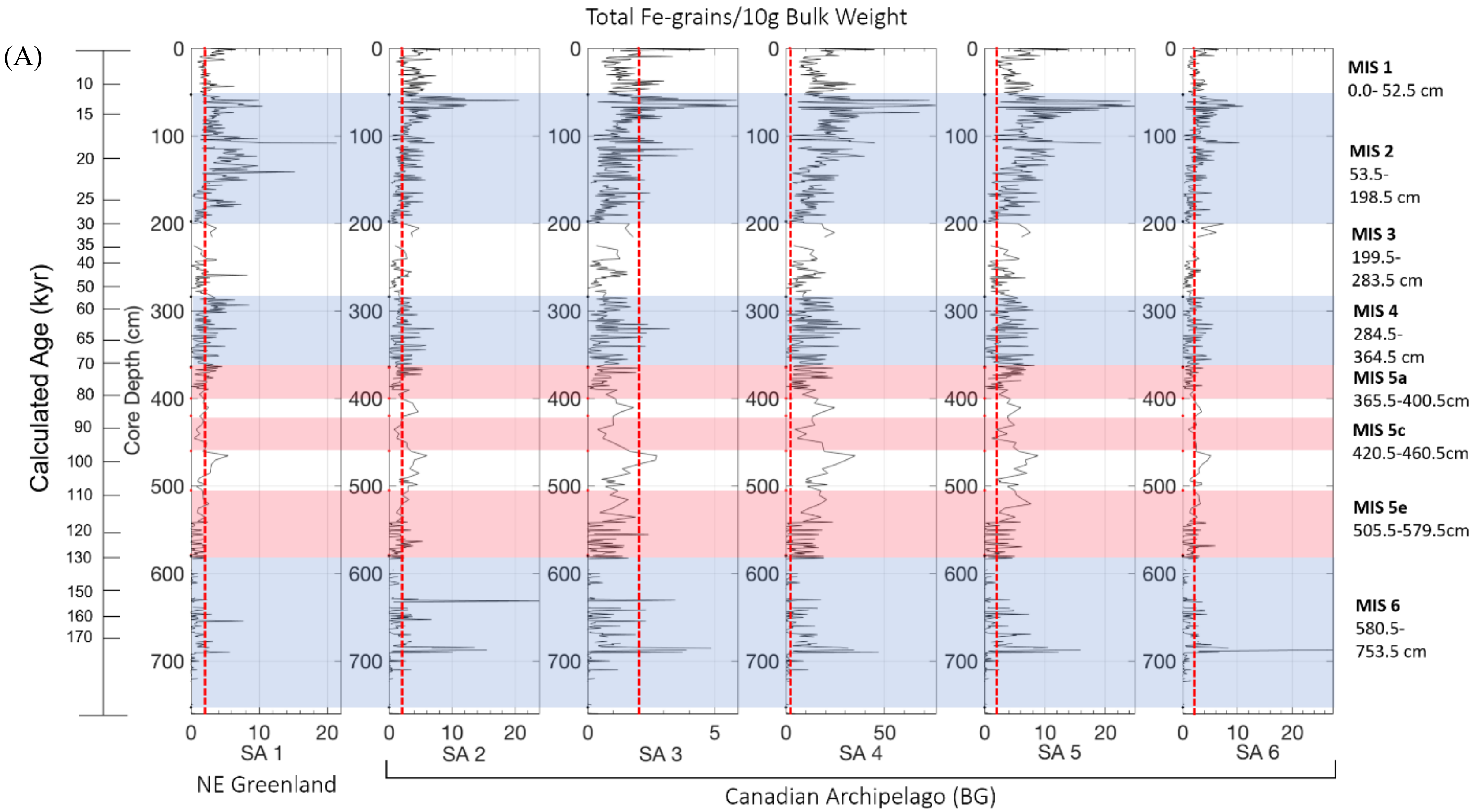

Fig. 13. Total number of Fe-grains matched/10g bulk weight for Individual SAs. (**A**), SA 1-6 (**B**), SA 7-12 (**C**), SA 13-18 (**D**), SA 19-24 (**E**), SA 25-30 (**F**), SA 31-36 (**G**), SA 37-41 (SAs listed on Fig. 2). If applicable, primary ocean surface currents are labelled as TPD and BG. Variable x-axis limits highlight Individual SA data.

Figure 13 Continued

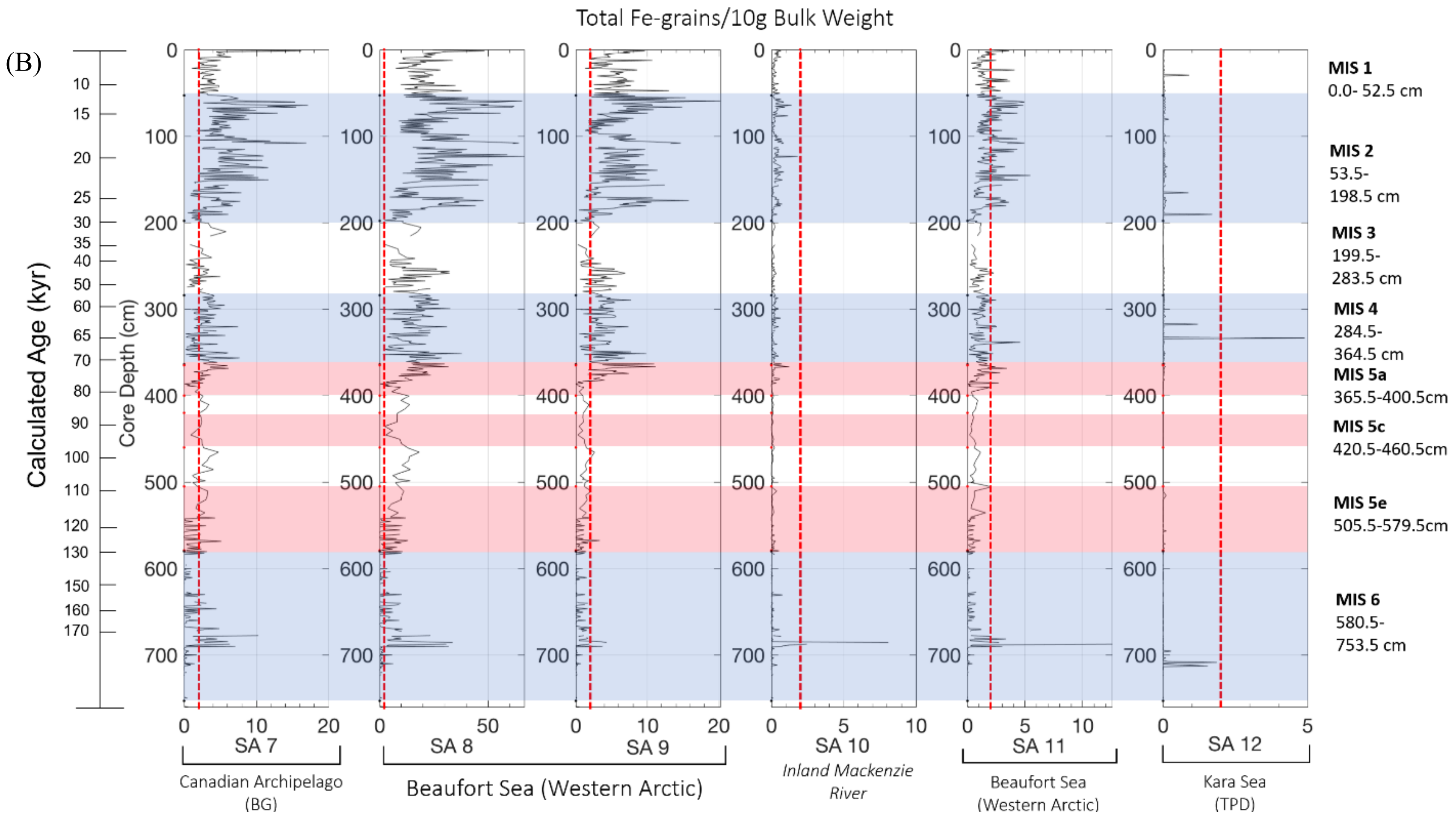

Figure 13 Continued

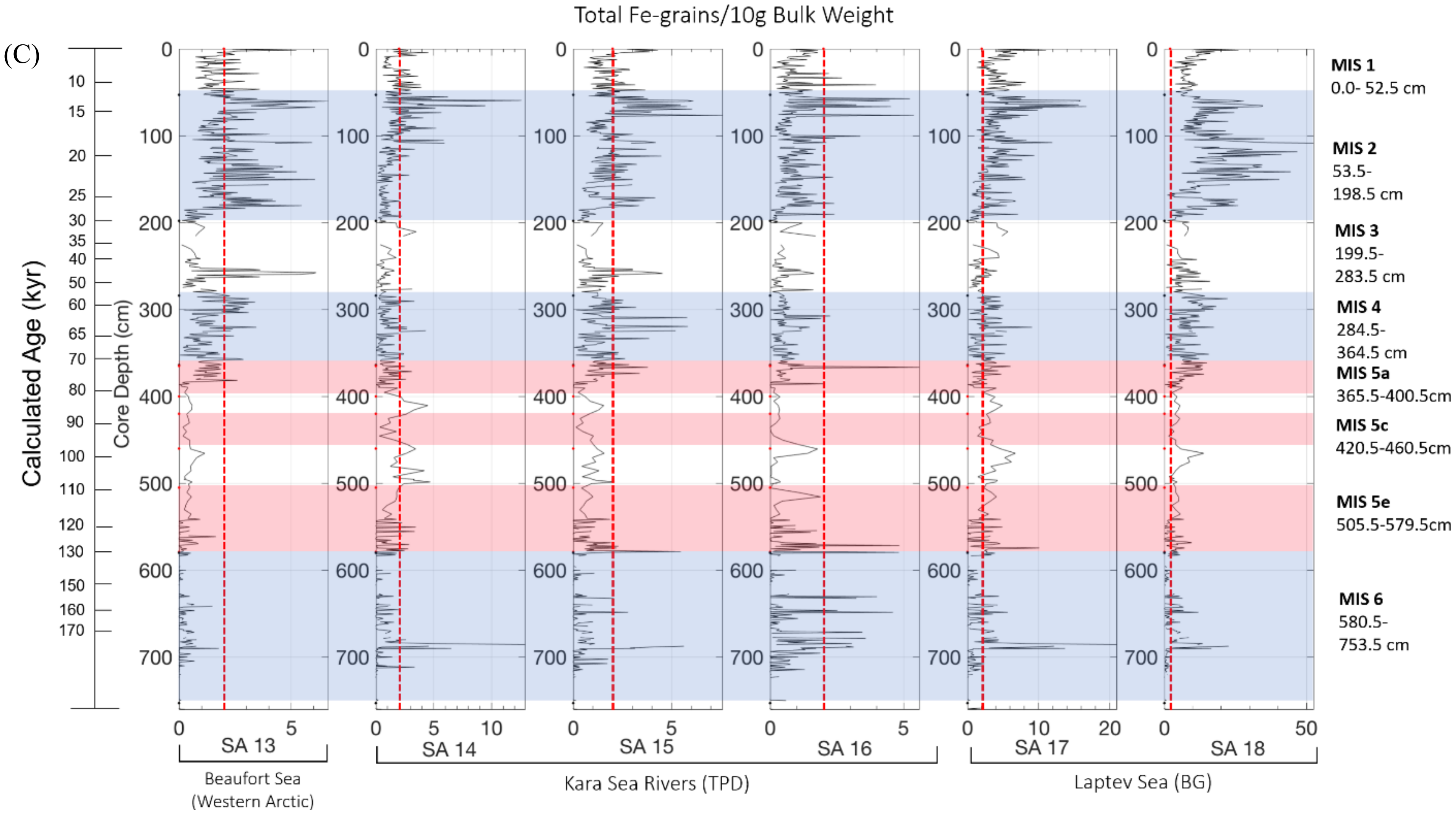

Figure 13 Continued

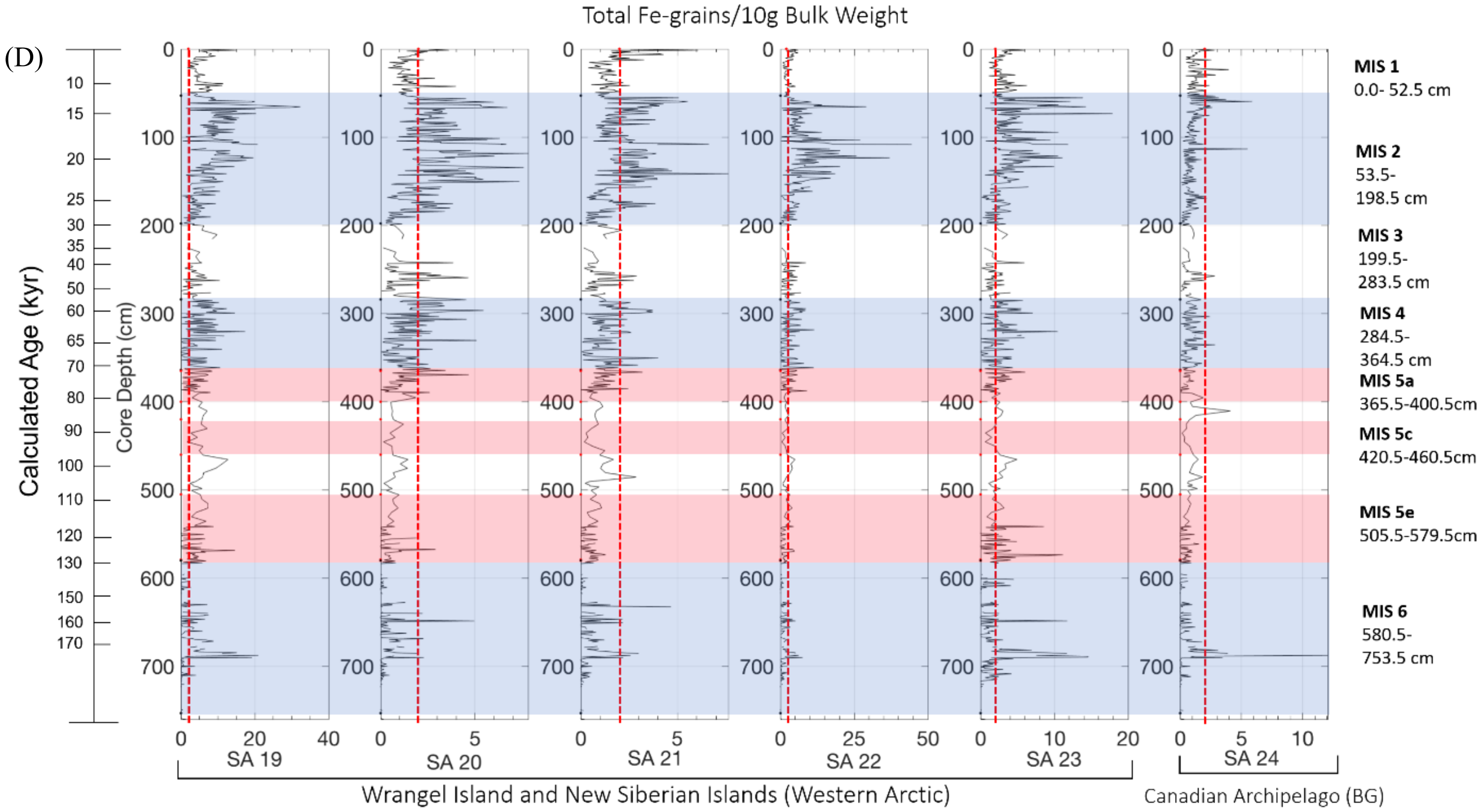

Figure 13 Continued

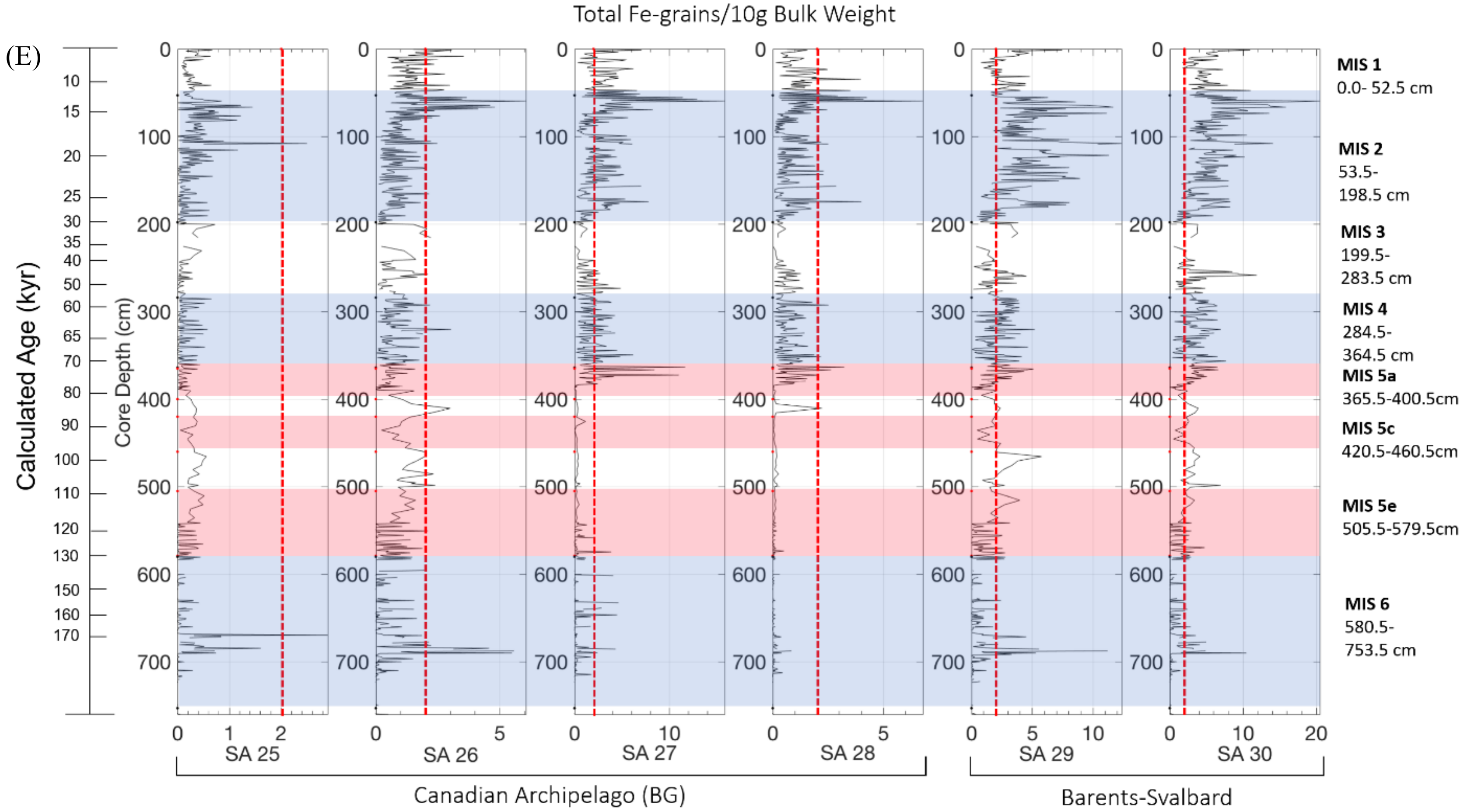

Figure 13 Continued

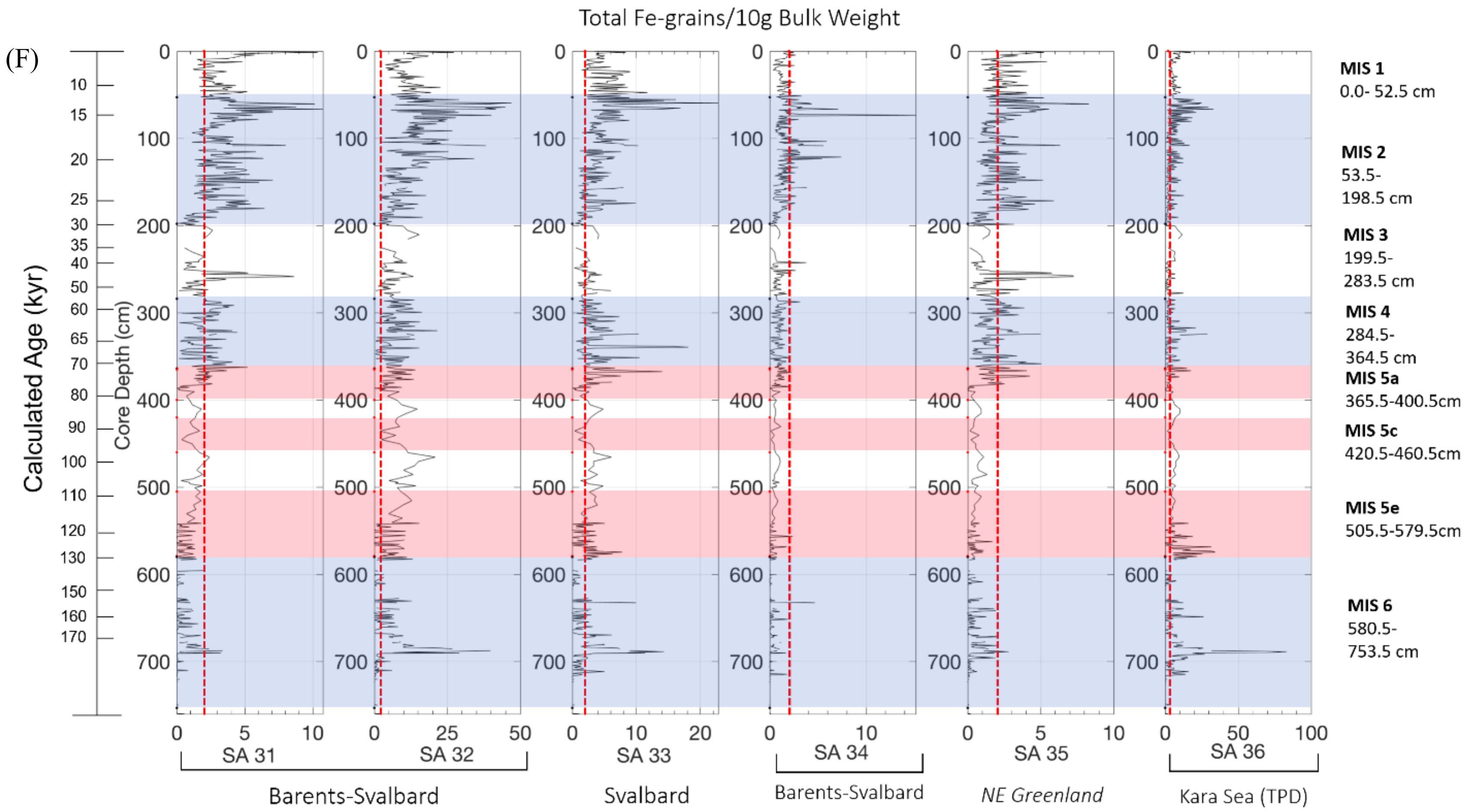

Figure 13 Continued

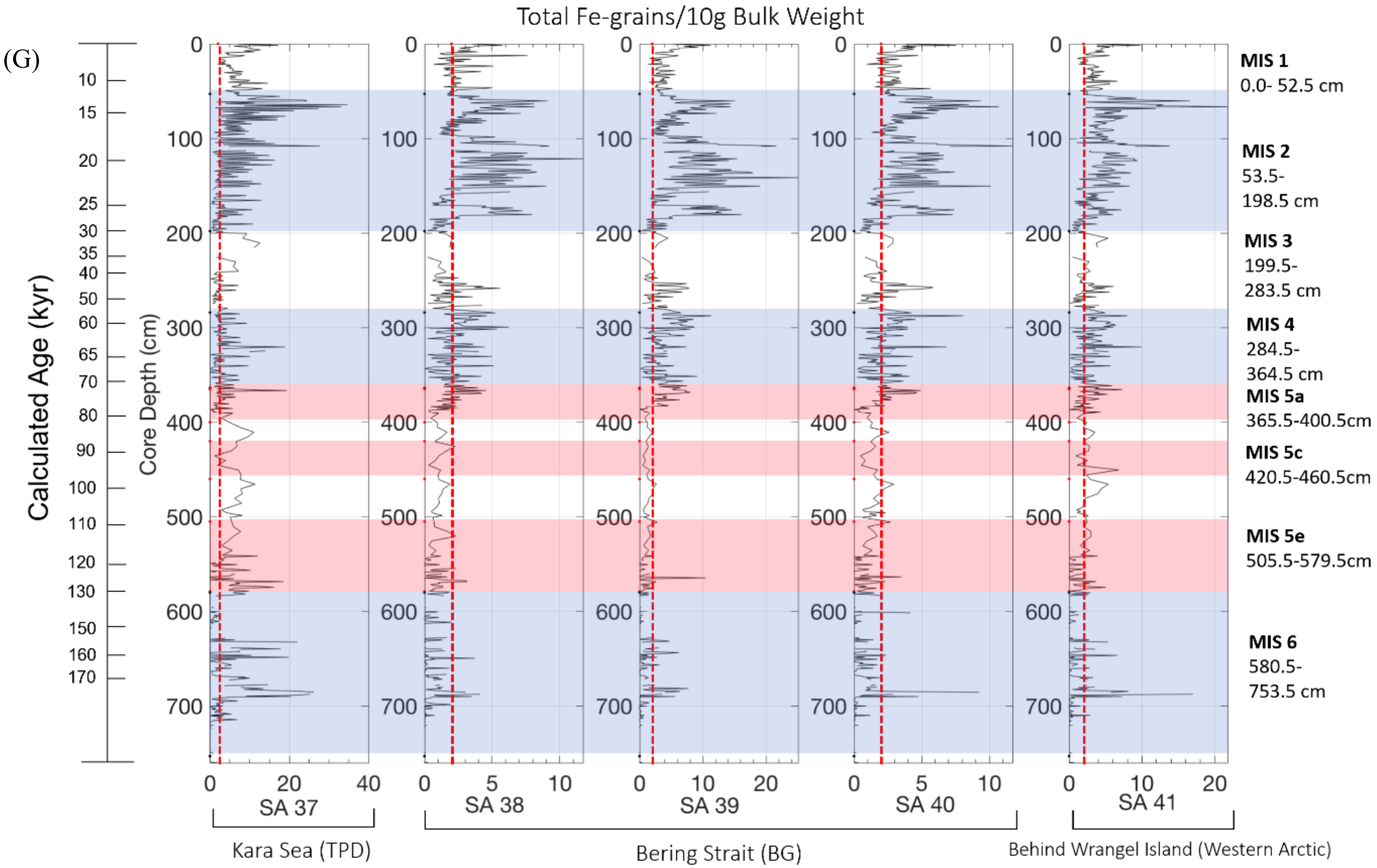

4.8 GROUPED SOURCE AREA FE-GRAIN MATCHING

Individual SAs are combined into SA Groups based on the objectives of this study, namely, to determine if large areas in the Arctic and circum-Arctic were sources for Fe-grains and IRD or were blocked by ice from delivering IRD to Fram Strait (Fig. 14). In each Section, "hiatus duration" thresholds are defined by intervals where Fe-grain numbers dropped below 2 Fe-grains/10 g bulk weight. All hiatus durations are identified to 0.01 kyr, primarily due to high sedimentation rates in MIS 2. To establish a comparison standard, all hiatus durations during MIS 4 and 6 are also identified to 0.01 kyr. All age interpretations are made to 0.1 kyr.

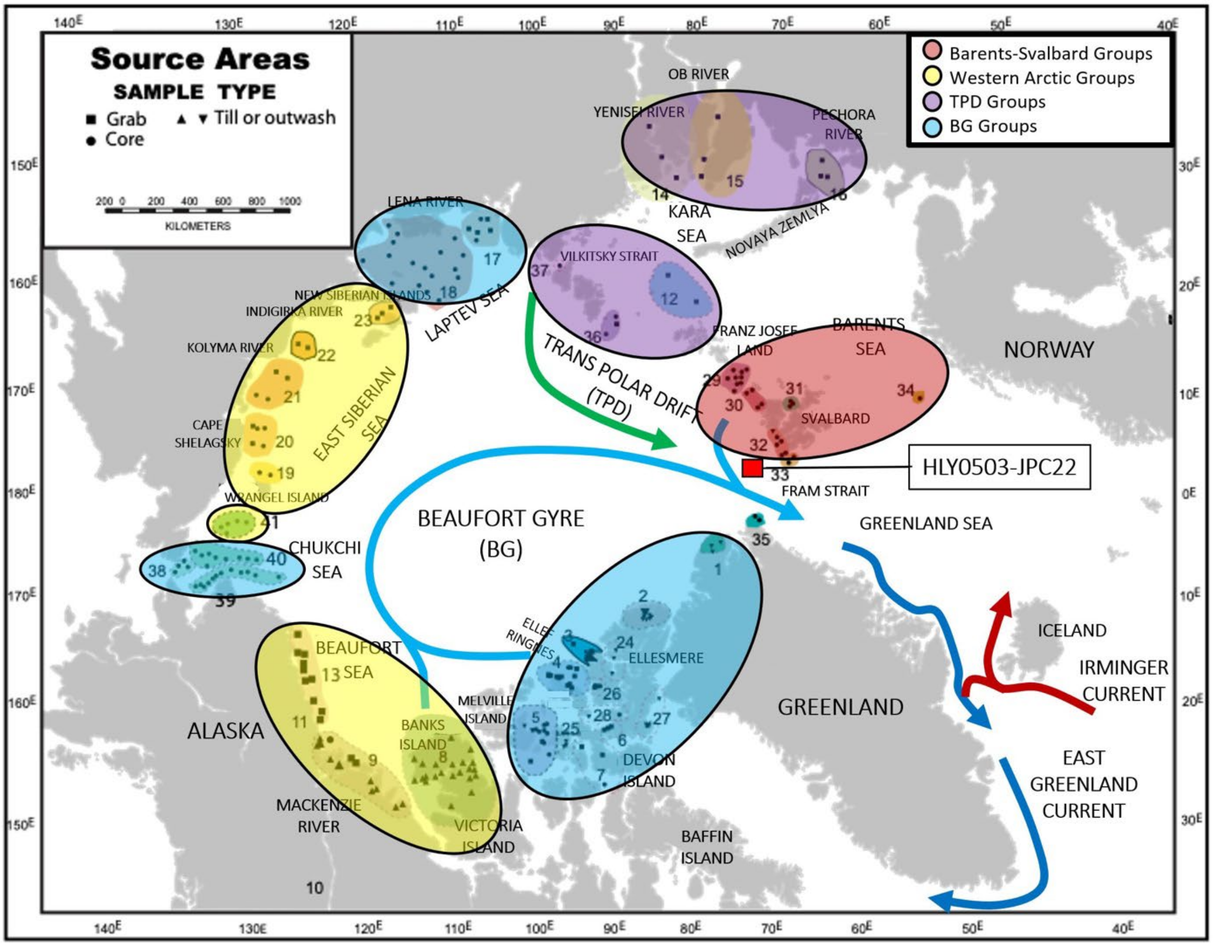

Fig. 14. Circumarctic SA Groups. SA Groups including Barents-Svalbard SA Groups (red shaded), Western Arctic SA Groups (yellow shaded), and Central Arctic SA Groups including TPD SA Groups (purple shaded) and BG SA Groups (blue shaded) (After Darby et al., 2017).

4.8.1 BARENTS-SVALBARD ICE SHEET

SAs are grouped together to help determine how the BSIS behaved during the LGM (MIS 2) and attempt to constrain when it disintegrated (Fig. 14). SAs are grouped as (Fig. 15): Barents-Svalbard sources (SA 29, 30, 31, 32, 34). SA 33, the SA closest to the core location provides context about melt-out conditions at the JPC22 core location. The BSIS objective requires high-resolution analysis during MIS 2, so the threshold for displayed hiatuses is defined by the average time per cm based on our sedimentation rate calculations during MIS 2 (Fig. 7 and Table 1). The hiatus duration threshold for Barents-Svalbard SAs is > 0.12 kyr.

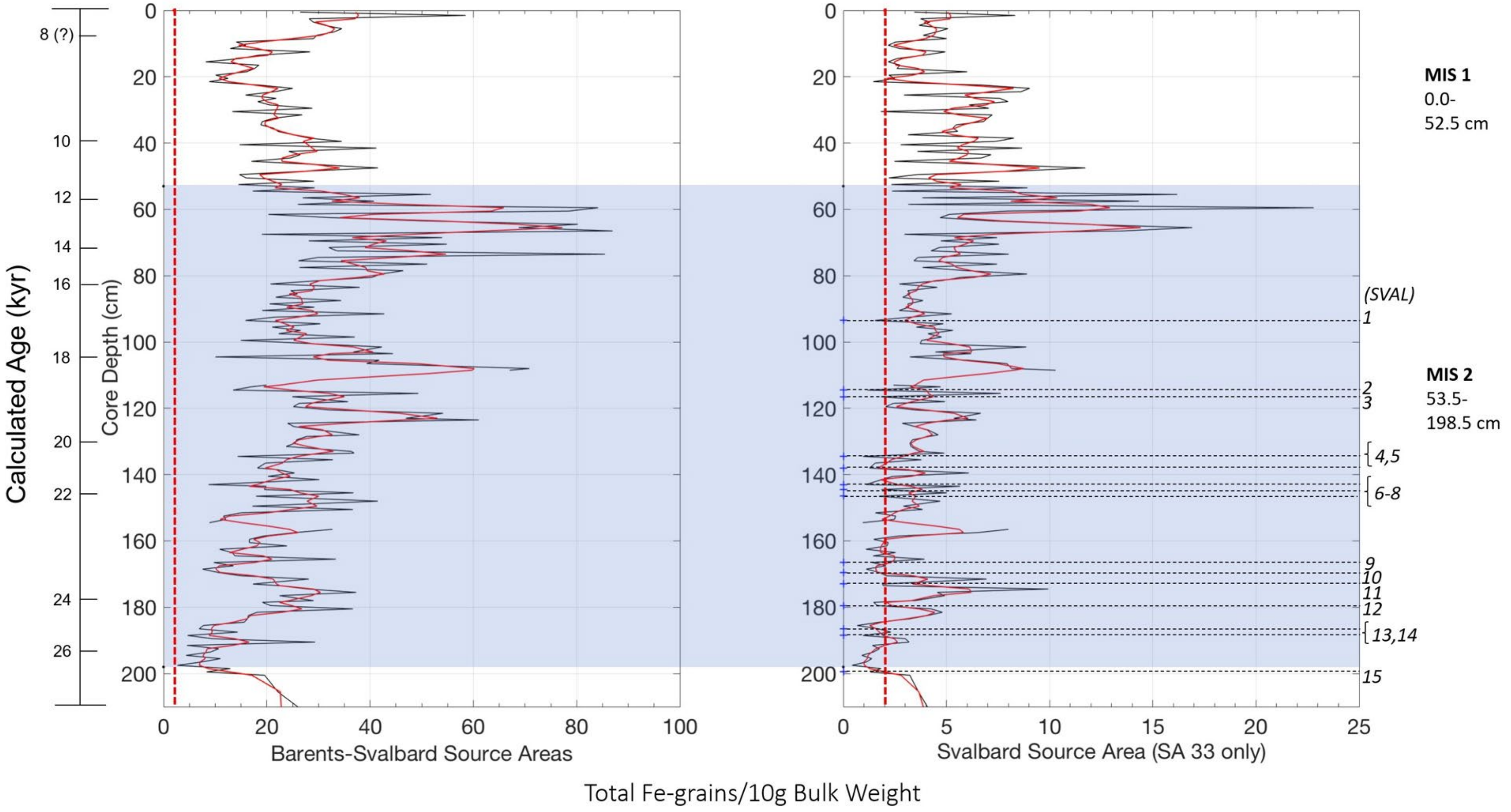

Fig. 15. Barents-Svalbard SA Groups and SA 33 (from Fig. 13) total number of Fe-grains/10 g bulk weight during MIS 2. Figure includes 5-cm boxcar smoothed data (solid red line), <2-grain threshold limit (red dashed line), and hiatuses >0.12 kyr (black dashed lines) described in Table 2.

4.8.1.1 MIS 2

Barents-Svalbard SAs have continuous, yet variable Fe-grain inputs throughout MIS 2 with no hiatuses. Fe-grains gradually increase from MIS 2 initiation to 18.6 ka, then decrease and peak again at 14.9 ka, 13.5 ka, 12.5 ka, and a minor peak at 12.0 ka (Fig. 15). The triple peak, consisting of 14.9 ka, 13.5 ka, and 12.5 ka have extremely high Fe-grain numbers of >80 Fe-grains/10 g bulk weight. While Barents-Svalbard SAs do not have any hiatuses during MIS 2, Svalbard SA 33 has several hiatuses. This source has a gradual Fe-grain trend increasing from ~17.0 ka to 13.5 ka followed by a triple peak, like the Barents-Svalbard SA. The triple peak at SA 33, starting at 13.5 ka, precedes the triple peak at Barents-Svalbard SA which starts at 12.5 ka.

While Barents-Svalbard SA lack hiatuses, SA 33 hiatuses (SVL4-SVL15) (Table 2) occur at MIS 2 initiation and intermittently through the middle of MIS 2. None of these hiatuses last more than 0.80 kyr with most <0.30 kyr. The longest hiatuses occur near the beginning of MIS 2.

The Barents-Svalbard Source Areas (MIS 2, 4, and 6) have a hiatus duration threshold of >1.00 kyr (Fig. 16 and Table 3). This provides a similar comparison to other >1.00 kyr hiatus durations in Western Arctic SAs (Section 4.8.2) and Central Arctic SAs (Section 4.8.3). During MIS 2, there is only one hiatus duration >1.00 kyr in SA 33 (SVAL15) (Table 2). SVAL15 is also identified as SVAlb1 (Table 3).

Table 2. Hiatuses for Barents-Svalbard SA Groups during MIS 2.

MIS	Core Depth (cm)	Hiatus Starting Age (kyr)	Barents-Svalbard		Svalbard	
			Hiatus Duration (kyr)	Hiatus ID Number	Hiatus Duration (kyr)	Hiatus ID Number
2	93.5	17.4			0.16	SVAL1
	114.5	19.1			0.16	SVAL2
	116.5	19.3			0.20	SVAL3
	134.5	21.0			0.26	SVAL4
	138.0	21.5			0.44	SVAL5
	143.0	22.6			0.53	SVAL6
	144.5	22.7			0.14	SVAL7
	146.5	22.8			0.13	SVAL8
	166.5	23.5			0.12	SVAL9
	169.5	23.8			0.26	SVAL10
	173.5	24.2			0.38	SVAL11
	179.5	25.1			0.44	SVAL12
	186.5	26.5			0.82	SVAL13
	188.5	26.9			0.43	SVAL14
	199.5	29.4			2.35	SVAL15

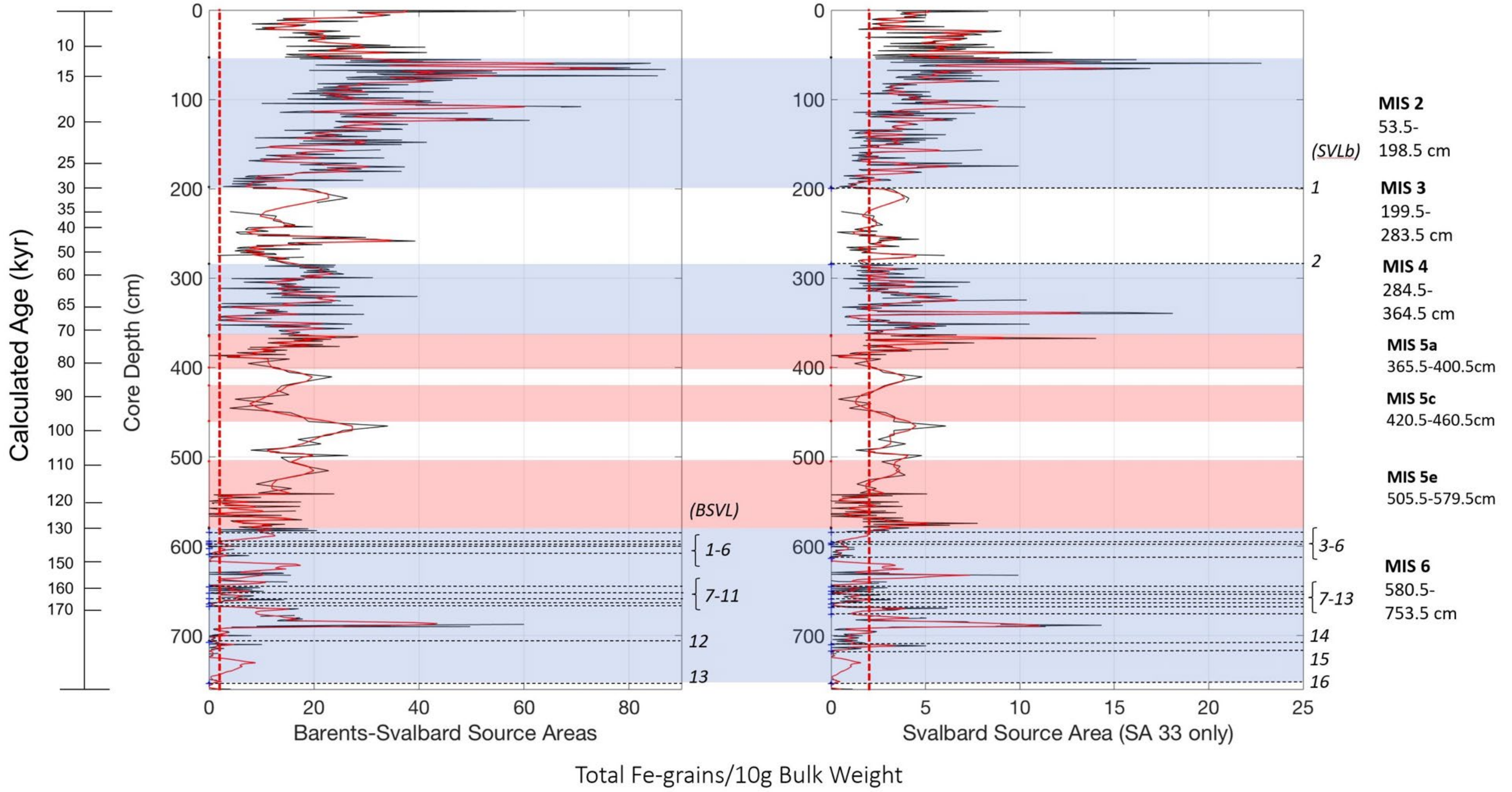

Fig. 16. Barents-Svalbard SA Groups and SA 33 (from Fig. 13) total number of Fe-grains/10 g bulk weight during MIS 2, 4, and 6. Figure includes 5-cm boxcar smoothed data (solid red line), <2-grain threshold limit (red dashed line), and hiatuses >1.00 kyr (black dashed lines) described in Table 3.

Table 3. Hiatuses for Barents-Svalbard SA Groups during MIS 2, 4, and 6.

MIS	**Core Depth (cm)**	**Hiatus Starting Age (kyr)**	**Barents-Svalbard**		**Svalbard**	
			Hiatus Duration (kyr)	**Hiatus ID Number**	**Hiatus Duration (kyr)**	**Hiatus ID Number**
2	199.5	29.4			2.35	SVLb1
4	284.5	57.9			3.56	SVLb2
6	584.5	132.1	1.33	BSVL1	1.33	SVLb3
	589.5	134.8	2.81	BSVL2	2.81	SVLb4
	594.5	138.9	4.60	BSVL3		
	596.5	140.6	1.78	BSVL4	6.37	SVLb5
	602.5	145.4	2.43	BSVL5		
	609.5	148.2	1.33	BSVL6		
	613.5	149.1			6.11	SVLb6
	645.5	156.3	1.35	BSVL7	1.64	SVLb7
	650.0	158.3			1.03	SVLb8
	652.5	159.7	1.19	BSVL8		
	653.5	160.3			2.36	SVLb9
	658.5	163.5	1.32	BSVL9		
	659.5	164.2			3.58	SVLb10
	664.5	167.4	1.83	BSVL10	3.44	SVLb11
	667.5	169.1	1.05	BSVL11		
	668.5	169.6			2.09	SVLb12
	676.5	172.4			1.80	SVLb13
	707.5	178.2	1.25	BSVL12		
	710.0	178.6			1.93	SVLb14
	717.5	179.7			1.09	SVLb15
	753.5	191.2	3.77	BSVL13	3.77	SVLb16

4.8.1.2 MIS 4

During MIS 4, the Barents-Svalbard SA Fe-grains are nearly constant with two minor peaks with >25 Fe-grains/10 g bulk weight at 63.3 ka and 65.4 ka (Fig. 16). In general, there are lower numbers of Fe-grains than in MIS 2. SA 33 shows similar peaks. During MIS 4, there is only one hiatus with a duration >1.00 kyr. SA 33 shows one hiatus at the initiation of MIS 4

(SVALb2) (Fig. 16 and Table 3) lasting 3.56 kyr. Barents-Svalbard SAs do not contain any hiatuses with durations >1.00 kyr. While Fe-grain numbers fall below the 2-grain threshold during MIS 4 (Fig. 16), especially in SA 33, none of the associated hiatus durations exceed 1.00 kyr.

4.8.1.3 MIS 6

Barents-Svalbard SAs and SA 33 show similar Fe-grain peaks during the middle of MIS 6 (Fig. 16). At 175.0 ka, the combined Barents-Svalbard SA Fe-grains reach 60 Fe-grains/10 g bulk weight. SA 33 shows a smaller peak (~14 Fe-grains/10 g bulk weight) occurring at the same time. There is a smaller Fe-grain peak at 152.8 ka in all Barents-Svalbard SAs.

Barents Svalbard SAs have numerous hiatuses with durations >1.00 kyr during MIS 6. Due to the number of hiatuses and their distribution, some hiatuses are grouped as “hiatus clusters”. All hiatuses are identified and listed by their “start date”. For example (Table 3), BSLV6 has an initiation “starting date” of 148.2 ka, and the hiatus cluster terminates with hiatus BSLV1 “starting” at 132.1 ka. However, these “starting dates” exclude BSLV1 duration of 1.33 kyr. Therefore, the full range of each hiatus cluster is calculated by subtracting the hiatus initiation “start date” (i.e., BLSV6) from the hiatus termination “start date” (i.e., BLSV1), and incorporating the duration of the final hiatus (i.e., 1.33 kyr). Accounting for the 1.33 kyr duration for BSLV1, the “hiatus cluster” ended at 130.8 ka. The full “hiatus cluster” duration spans from 148.2 ka to 130.8 ka for a total hiatus cluster duration of 17.4 kyr. All hiatus cluster calculations are located in Table 11.

Barents Svalbard SAs have two hiatus clusters during MIS 6. One cluster during the middle of the stage spans 155.0-169.1 ka (BSVL7-11) with a total duration of 14.1 kyr. Another cluster near the MIS 6 termination spans 130.8-148.2 ka (BSVL1-6) lasting 17.8 kyr (Tables 3 and 11).

Near MIS 6 initiation, there are hiatuses in Barents-Svalbard SAs (BSVL13) and in SA 33 (SVLb16) that have durations of 3.77 kyr. SA 33 has two hiatus clusters. One occurs during the middle of the stage from 154.7-172.4 ka (SVALb7-13) lasting 16.1 kyr (Tables 3 and 11). This hiatus cluster occurs at nearly the same time as the Barents-Svalbard hiatus cluster, albeit 3.6 kyr longer. Another SA 33 hiatus cluster occurs at 130.8-149.1 kyr (SVALb3-6) lasting 18.3. kyr (Tables 3 and 11). This second SA 33 hiatus cluster is nearly identical to the combined Barents-Svalbard Source Group hiatus cluster BSVL1-6. In all Barents-Svalbard SAs, the 175.9 ka Fe-grain peak precedes the 155.0-169.1 ka (or 154.7-172.4 ka in SA 33) hiatus cluster, followed by the 152.8 ka Fe-grain peak, then the second hiatus cluster at 130.8-148.2 ka.

4.8.2 WESTERN ARCTIC OCEAN SIMS

SAs are grouped to help determine the presence and/or ages of proposed SIMs (Polyak et al., 2001; Jakobsson et al., 2008) on the East Siberian shelf near Wrangel Island and New Siberian Islands, and shelf areas of the Beaufort Sea, or at least determine when these SIMs disintegrated if they existed (Fig. 14). SAs are grouped as follows (Fig. 17): Wrangel Island and New Siberian Islands sources (SA 19, 20, 21, 22, 23) and Beaufort Sea sources (SA 13, 11, 9, 8). SA 41 (Fig. 13), located immediately southeast of Wrangel Island provides context for monitoring ice-rafting from this source that might have been ice-covered at times. The hiatus duration threshold for Western Arctic SAs is >1.00 kyr.

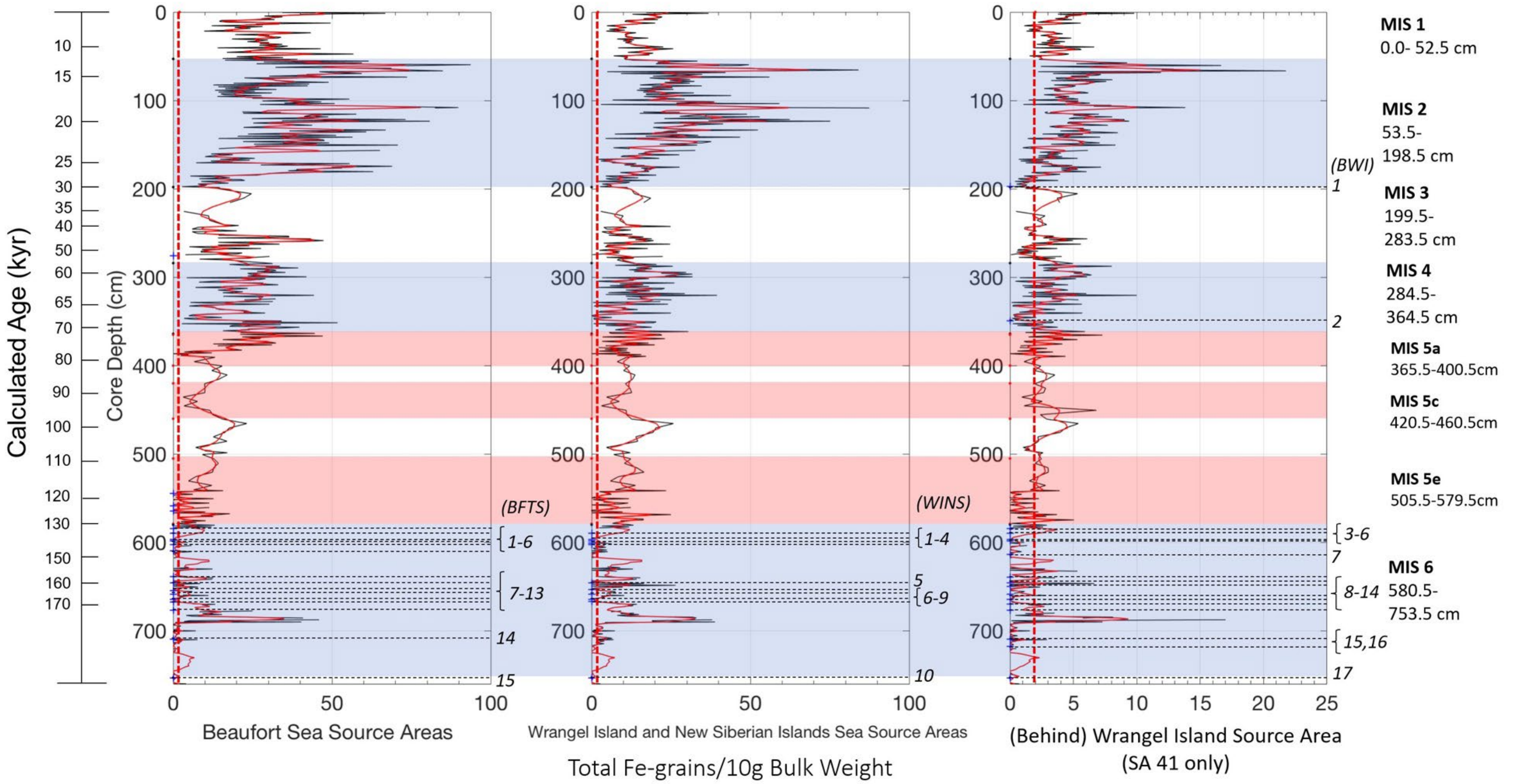

Fig. 17. Western Arctic SA Groups total number of Fe-grains/10 g bulk weight during MIS 2, 4, and 6. SA groups include Wrangel Island and New Siberian Islands SAs (representing East Siberian SAs) and Beaufort Sea SAs (Fig. 13). Figure includes 5-cm boxcar smoothed data (solid red line), <2-grain threshold limit (red dashed line), and hiatuses >1.00 kyr (black dashed lines) described in Table 4.

4.8.3.1 MIS 2

During MIS 2, all SAs show continuous Fe-grain numbers with peaks that culminate around 19 ka and again around 14 ka (Fig. 17). There sole hiatus during MIS 2 was for SA 41 at 28.9 ka, near the MIS 2 initiation (BWI1) (Table 4).

4.8.3.2 MIS 4

Fe-grain numbers vary but are constant throughout MIS 4 with no identified hiatuses for the Beaufort Sea SAs and Wrangel Island and New Siberian Islands SAs (Fig. 17). Compared to other SAs, Fe-grain numbers are still high with peaks of >30 Fe-grains. However, Fe-grain numbers are much lower than during MIS 2. Wrangel Island and New Siberian Islands SAs Fe-grain numbers drop below the hiatus threshold at 66.6 ka; however, the durations only range from 0.22 kyr to 0.66 kyr, which do not exceed 1.00 kyr (Table 4). There is one hiatus for SA 41 at 67.1 ka, just after the MIS 4 initiation (BWI2) (Table 4).

4.8.3.3 MIS 6

The Beaufort Sea SAs and Wrangel Island and New Siberian Islands SAs are dominated by hiatuses during MIS 6. Beaufort Sea SA hiatuses during MIS 6 are clustered near the termination at 132.2 ka to 148.0 ka (BFTS1-6), with a total duration of 15.8 kyr, and another cluster spans the middle of the stage 152.7 ka to 178.5 ka (BFTS7-13), lasting 25.8 kyr (Tables 4 and 11).

Table 4. Hiatuses for Western Arctic SA Groups during MIS 2, 4, and 6.

MIS	**Core Depth**	**Hiatus Starting Age**	**Beaufort Sea**		**Wrangel Island and New Siberian Islands**		**Behind Wrangel Island**	
			Hiatus Duration	**Hiatus ID Number**	**Hiatus Duration**	**Hiatus ID Number**	**Hiatus Duration**	**Hiatus ID Number**
	(cm)	**(kyr)**	**(kyr)**		**(kyr)**		**(kyr)**	
2	197.5	28.9					1.79	BWI1
4	349.5	67.1					1.00	BWI2
6	584.5	132.1	1.33	BFTS1			1.33	BW13
	589.5	134.8	2.81	BFTS2	2.81	WINS1	2.81	BW14
	596.5	140.6	6.37	BFTS3	6.37	WINS2	6.37	BW15
	598.5	142.4	1.70	BFTS4			1.70	BW16
	600.5	144.0			1.14	WINS3		
	602.5	145.4	2.43	BFTS5	1.29	WINS4		
	609.5	148.2	2.30	BFTS6				
	613.5	149.1					6.11	BWI7
	638.5	154.2	1.67	BFTS7				
	639.5	154.5					1.80	BWI8
	645.5	156.3	1.35	BFTS8	1.35	WINS5	1.64	BWI9
	650.0	158.3					1.91	BWI10
	653.5	160.3			2.36	WINS6		
	654.5	160.9	3.00	BFTS9				
	658.5	163.5	1.32	BFTS10	1.32	WINS7	5.61	BW11
	664.5	167.4	1.83	BFTS11	1.83	WINS8	3.44	BW12
	666.5	168.5			1.11	WINS9		
	667.5	169.1	1.62	BFTS12				
	669.5	170.0					2.32	BWI13
	676.5	172.4	1.45	BFTS13			1.45	BWI14
	709.5	178.5	1.47	BFTS14			3.13	BWI15
	717.5	179.7					1.31	BWI16
	753.5	191.2	3.77	BFTS15	3.77	WINS10	3.77	BWI17

Wrangel Island and New Siberian Islands SAs have two MIS 6 hiatus clusters at nearly the same time as those for the Beaufort Sea. One between 132.2 ka and 145.5 ka (WINS1-4) lasting 13.5 kyr, and a second hiatus cluster from 154.7 ka and 168.0 ka (WINS6-9) lasting 13.3

kyr (Tables 4 and 11). Beaufort Sea SA hiatuses are slightly longer but align with the timing of Wrangel Island and New Siberian Islands SAs hiatuses.

While Fe-grains are low during MIS 6, there are several peaks during this stage. Fe-grains peak between 170.0-175.6 ka in all Western SAs, with numbers nearly reaching 50 Fe-grains/10 g bulk weight in the Beaufort Sea and 40 Fe-grains in Wrangel Island and New Siberian Islands Sea. There are smaller Fe-grain peaks (16 Fe-grains/10 g bulk weight) at Wrangel Island and New Siberian Islands SAs at 157.6 ka and 152.2 ka. There is no Fe-grain peak of any size near the close of MIS 6.

4.8.3 CENTRAL ARCTIC OCEAN THICK ICE CONSTRAINTS

SAs are grouped together to help determine if large ice masses existed in the central Arctic Ocean that might have reduced or prevented ice-rafting (Fig. 14). To address the central Arctic ice hypothesis, sources are grouped by their primary transport current: the Beaufort Gyre or the Transpolar Drift, both of which cross slightly different parts of the central Arctic Ocean (Figs. 2 and 16). Beaufort Gyre (BG) Groups include the following: Bering Strait SA Group (SA 38, 39, and 40); Laptev Sea SA Group (SA 17, 18); NE Greenland (SA1); and Canadian Archipelago SA Group (SA 2, 3, 4, 5, 6, 7, 24, 25, 26, 27, 28) in Fig. 18. We also include all Western Arctic SA Groups from Section 4.3.1 in Fig. 17 to address the Central Arctic Ocean thick ice objective. Transpolar Drift (TPD) Groups include the following: Kara Sea [and Severnaya Zemlya, Russian archipelago extending from the Taymyr Peninsula] SA Group (SA 37, 36, 12), and the Kara Sea Rivers SA Group (SA 15, 14, 16) in Fig. 19. The hiatus duration threshold for Central Arctic SAs is >1.00 kyr.

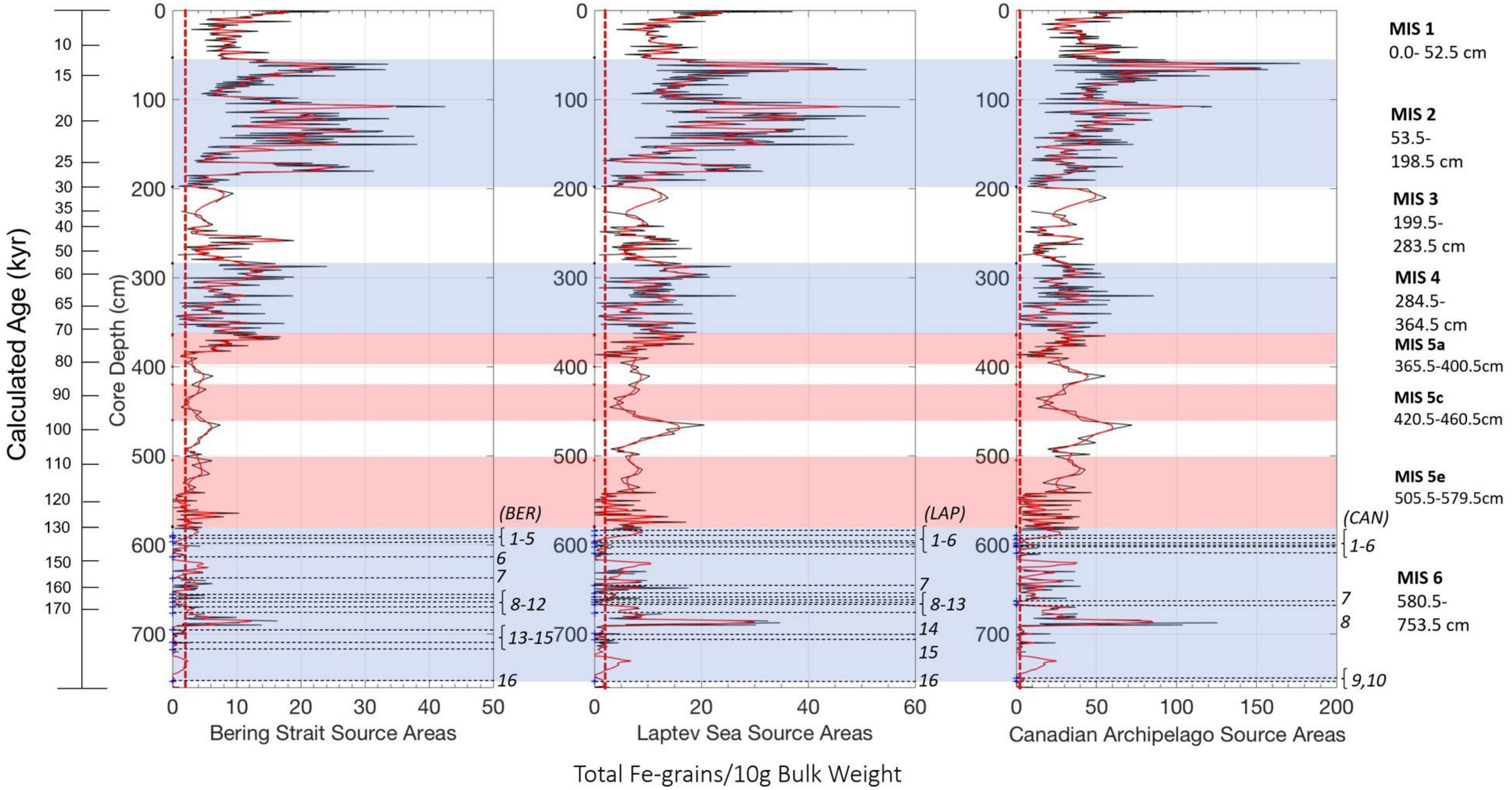

Fig. 18. Central Arctic (BG) SA Groups total number of Fe-grains/10 g bulk weight during MIS 2, 4, and 6. SA Groups include Bering Strait SAs, Laptev Sea SAs, and Canadian Archipelago SAs. Figure includes 5-cm boxcar smoothed data (solid red line), <2-grain threshold limit (red dashed line), and hiatuses >1.00 kyr (black dashed lines) described in Table 5.

Table 5. Hiatuses for Central Arctic (BG) SA Groups during MIS 2, 4, and 6.

MIS	Core Depth	Hiatus Starting Age	Beaufort Gyre (BG)					
			Bering Strait		Laptev Sea		Canadian Archipelago	
			Hiatus Duration	Hiatus ID Number	Hiatus Duration	Hiatus ID Number	Hiatus Duration	Hiatus ID Number
	(cm)	(kyr)	(kyr)		(kyr)		(kyr)	
6	584.5	132.1			1.33	LAP1		
	589.5	134.8	2.81	BERS1	2.81	LAP2	2.81	CAN1
	591.5	136.3	1.97	BERS2				
	594.5	138.9					4.60	CAN2
	596.5	140.6	4.41	BERS3	6.37	LAP3		
	598.5	142.4	1.70	BERS4	1.70	LAP4	1.70	CAN3
	600.0	143.6	1.63	BERS5			1.14	CAN4
	602.5	145.4			2.43	LAP5	1.29	CAN5
	609.5	148.2			2.30	LAP6	1.77	CAN6
	613.5	149.1	4.58	BERS6				
	637.5	154.0	1.64	BERS7				
	645.5	156.3			1.35	LAP7		
	654.5	160.9			3.00	LAP8		
	655.5	161.6	3.65	BERS8				
	658.5	163.5			1.32	LAP9	1.32	CAN6
	659.5	164.2	2.30	BERS9				
	661.5	165.5			1.62	LAP10		
	664.5	167.4	3.44	BERS10	1.83	LAP11	1.83	CAN7
	666.5	168.5					1.11	CAN8
	667.5	169.1			1.62	LAP12		
	669.5	170.0	2.32	BERS11				
	676.5	172.4	1.45	BERS12	1.45	LAP13		
	695.5	176.4	1.12	BERS13				
	709.5	178.5	1.47	BERS14	1.04	LAP14		
	717.5	179.7	1.31	BERS15	1.10	LAP15		
	749.5	189.0					1.30	CAN9
	753.5	191.2	3.77	BERS16	3.77	LAP16	2.47	CAN10

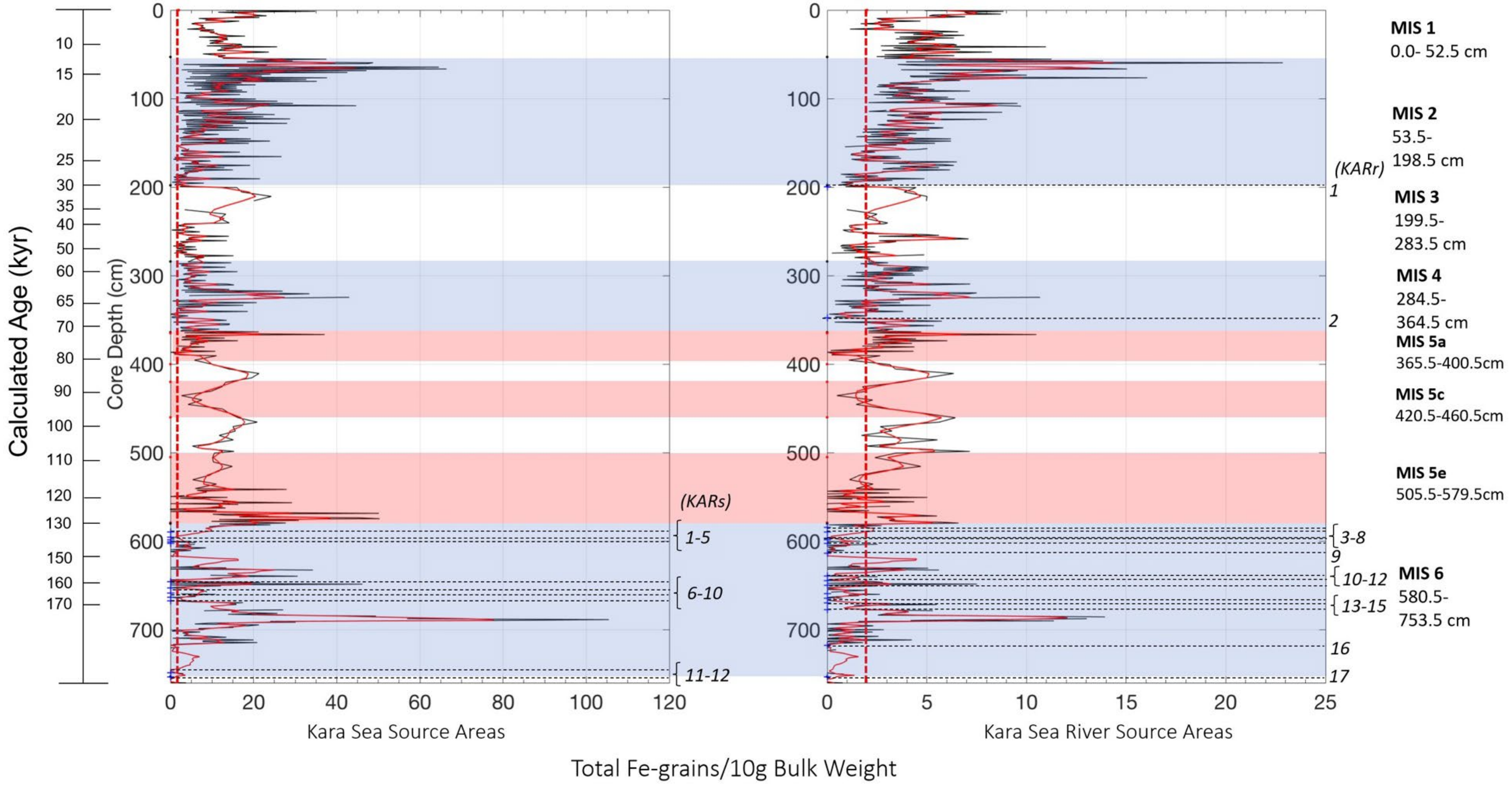

Fig. 19. Central Arctic (TPD) SA Groups total number of Fe-grains/10 g bulk weight during MIS 2, 4, and 6. SA Groups include Kara Sea SAs and Kara River SAs. Figure includes 5-cm boxcar smoothed data (solid red line), <2-grain threshold limit (red dashed line), and hiatuses >1.00 kyr (black dashed lines) described in Table 6.

Table 6. Hiatuses for Central Arctic (TPD) SA Groups during MIS 2, 4, and 6.

MIS	Core Depth	Hiatus Starting Age	Transpolar Drift (TPD)			
			Kara Sea		Kara Sea Rivers	
	(cm)	(kyr)	Hiatus Duration (kyr)	Hiatus ID Number	Hiatus Duration (kyr)	Hiatus ID Number
2	199.5	29.4			1.91	KARr1
4	347.5	66.7			1.38	KARr2
6	584.5	132.1			1.33	KARr3
	589.5	134.8	2.81	KARs1	2.81	KARr4
	595.5	139.7	5.49	KARs2		
	596.5	140.6			6.37	KARr5
	598.5	142.4	1.70	KARs3	1.70	KARr6
	600.5	144.0	1.14	KARs4		
	602.5	145.4	1.29	KARs5	2.83	KARr7
	613.5	149.1			3.28	KARr8
	639.5	154.5			1.80	KARr9
	644.5	155.9			1.54	KARr10
	645.5	156.3	1.35	KARs6		
	650.0	158.3			1.03	KARr11
	652.5	159.7	1.19	KARs7		
	658.5	163.5	1.32	KARs8		
	659.5	164.2			5.94	KARr12
	661.5	165.5				
	663.5	166.8	1.24	KARs9		
	664.5	167.4			3.44	KARr13
	667.5	169.1	1.05	KARs10		
	669.5	170.0			2.32	KARr14
	677.5	172.7			2.07	KARr15
	717.5	179.7			1.09	KARr16
	748.5	188.5	1.04	KARs11		
	753.5	191.2	2.73	KARs12	3.77	KARr17

4.8.3.1 MIS 2

BG Groups (Bering Strait, Laptev Sea, and Canadian Archipelago) have similar Fe-grain trends during MIS 2 as do the Beaufort Sea SAs and Wrangel Island and New Siberian Islands SAs (Fig. 17). Both BG SA Groups have distinct Fe-grain peaks at 25.3 ka, 4 kyr after the MIS 2 initiation. There are additional peaks during the middle of MIS 2 at 23.0 ka, 22.4 ka and another large peak at 18.6 ka. Between the 18.6 ka and 13.6 ka peaks, Fe-grain numbers never fall below the hiatus threshold. Canadian Archipelago Fe-grains follow the same trend but lack the distinct Fe-grain peaks at 23.0 ka and 22.4 ka. Canadian Archipelago sources have some of the highest values of Fe-grains out of all 41 SAs during MIS 2, with peaks >100 Fe-grains/10 g bulk weight. Laptev Sea sources and LIS outlet (SA8) also have multiple peaks >50 Fe-grains/10 g bulk weight. TPD SA groups (Kara Sea and Kara Sea Rivers) show similar Fe-grain trends as Canadian Archipelago with a minor peak at 18.6 ka and a more distinct peak at 13.5 ka. In the Kara Sea sources, the 13.5 ka peak reached 66 Fe-grains/10 g bulk weight.

Hiatuses for all Central Arctic groups are listed in Table 5 and Table 6. Among all BG Groups, TPD Groups, and Western Arctic SA Groups there is only one hiatus in the Kara Sea River Sources, KARr1, at MIS 2 initiation at 29.4 ka (Table 6), and the previously identified BWI1 hiatus in SA 41 at 28.9 ka. While Fe-grain numbers fall below our <2 grain threshold in Kara Sea sources, the hiatus duration does not exceed 1.00 kyr.

4.8.3.2 MIS 4

TPD Groups, BG Groups, and Western Arctic Groups have variable, but generally continuous Fe-grain transport during MIS 4. Canadian Archipelago, Kara Sea, and Kara Sea River Sources lack a distinct Fe-grain peak at MIS 4 termination. An Fe-grain peak occurs across all TPD Groups, Beaufort Gyre Groups, and Western Arctic Groups during the middle of MIS 4 at 63.3 ka. Bering Strait and Laptev Sea sources also show a peak at 58.7 ka, near MIS 4 termination.

In all three groups, there is only a hiatus in the Kara Sea River sources, KARr2, at 66.7 ka (Table 6), and the previously identified BWI2 hiatus in SA 41 at 67.1 ka. Once again, Fe-grain numbers fall below our <2 grain threshold in portions of MIS 4, but the hiatus durations do not exceed 1.00 kyr.

4.8.3.3 MIS 6

All Central Arctic SA Groups show clusters of hiatuses during MIS 6. Hiatus cluster durations may help constrain the amount of time a central ice mass was present. Two groups of hiatus clusters occur with one during the middle of MIS 6 and another at MIS 6 termination.

TPD Groups, Beaufort Gyre Groups, and Western Arctic Groups have clusters of hiatuses during the middle of MIS 6 with a general range from 157-171 ka (Table 13) and near the MIS 6 termination generally ranging from 131-147 ka (Table 12). Kara Sea Rivers Sources have additional intermittent hiatuses between the hiatus clusters of other SA Groups.

One major Fe-grain peak occurs across all Western Arctic Groups, Beaufort Gyre Groups, and TPD Groups at 175.0 ka (Figs. 17, 18, and 19). After a hiatus cluster from 157.0-170.8 ka, there are several smaller peaks around 157.6 ka and 152.2 ka before the second hiatus cluster from 130.8-146.9 ka. Even though the 157.6 ka and 152.2 ka Fe-grain peaks were smaller than the earlier 175.0 ka peak, large Fe-grain numbers (46 Fe-grains/10 g bulk weight) occur from the Beaufort Sea sources, mostly from SA 8, the LIS outlet area.

CHAPTER 5

DISCUSSION

5.1 DISCUSSION OVERVIEW

To resolve the three study objectives, we applied our analyzed JPC22 data including: the age model, sedimentation rates, IRD (wet sieve) weights (g) by size fractions, foram abundances, SEM quartz grain analysis, Fe-grain matching to all 41 SAs, and Fe-grain matching to Grouped SAs.

5.2 BARENTS-SVALBARD ICE SHEET

Barents-Svalbard Grouped SAs have constant, yet varied Fe-grain inputs throughout MIS 2 with no hiatuses (Fig. 15). Constant Fe-grain input conditions may help constrain the additional consideration of melt out conditions in Fram Strait. While hiatuses may indicate a lack of material from SAs, they could also indicate a lack of sediment deposition via melt out in Fram Strait. However, constant Fe-grains throughout MIS 2 suggest melt out is occurring; therefore, a lack of melt out can be ruled out to explain a hiatus in Fe-grains. Additionally, the presence of abundant forams throughout MIS 2, with two exceptions at 23.3 ka and 13.5 ka (Fig. 11), indicates Fram Strait had open water or light ice conditions. In general, sedimentation rates are much higher during MIS 2 than MIS 4 or 6. Two possible explanations are lack of sediment compaction or higher melt-out rates at the core site during MIS 2. Because this timeframe is near the top of the core, the sediment has not undergone as much compaction as MIS 4 or 6. However, MIS 2 has two periods with sedimentation rates >10 cm/kyr (Fig. 7). One of these periods has a short-lived, but extremely high rate of 25.6 cm/kyr during the middle of MIS 2. This may suggest melt out rates were also higher during MIS 2.

Fe-grains increase from MIS 2 initiation to peaks at 19.9 ka and 18.6 ka. Fe-grain numbers form a triple-peak at 12.5 ka, 13.5 ka, and 14.9 ka. The 14.9 ka Fe-grain peak does not correspond to a coarser >63 µm IRD peak, but finer 45-63 µm IRD instead (Fig. 20). The BSIS collapse starting at 14.9 ka is not detected in cores closer to Svalbard but is seen in a core farther east near Franz Josef Land (Patton et al., 2015). During these triple peaks, sedimentation rates were between 6.1 to 6.5 cm/kyr, which is moderately high for the Arctic. These peaks indicate a dynamic period of BSIS ice export events or calving of the Barents Ice Sheet. Where the >63 µm IRD decreases for some of the Fe-grain peaks between 18.6 ka and 13.5 ka suggest that these might be sea ice events instead of BSIS calving events.

At 18.6 ka there is a major BSIS calving event based on the Fe-grain peak here that coincides with a >63 µm IRD peak (Fig. 21). This corresponds nicely to the age of the first of a two-stage collapse proposed by Patton et al. (2015). Following this collapse, the BSIS slowly rebuilt, or sea ice thickened in response to a climate feed-back causing cooling and preventing further collapse (Patton et al., 2015), before the Fe-grain transport events and >63 µm IRD events at 13.5 ka and 12.5 ka, albeit a minor IRD peak, indicating the final part of a two-stage collapse. The final MIS 2 BSIS collapse occurs at 13.5 ka and 12.5 ka, again as a two-pulse event. Previous studies did not recognize these dual pulse collapses (Patton et al., 2015).

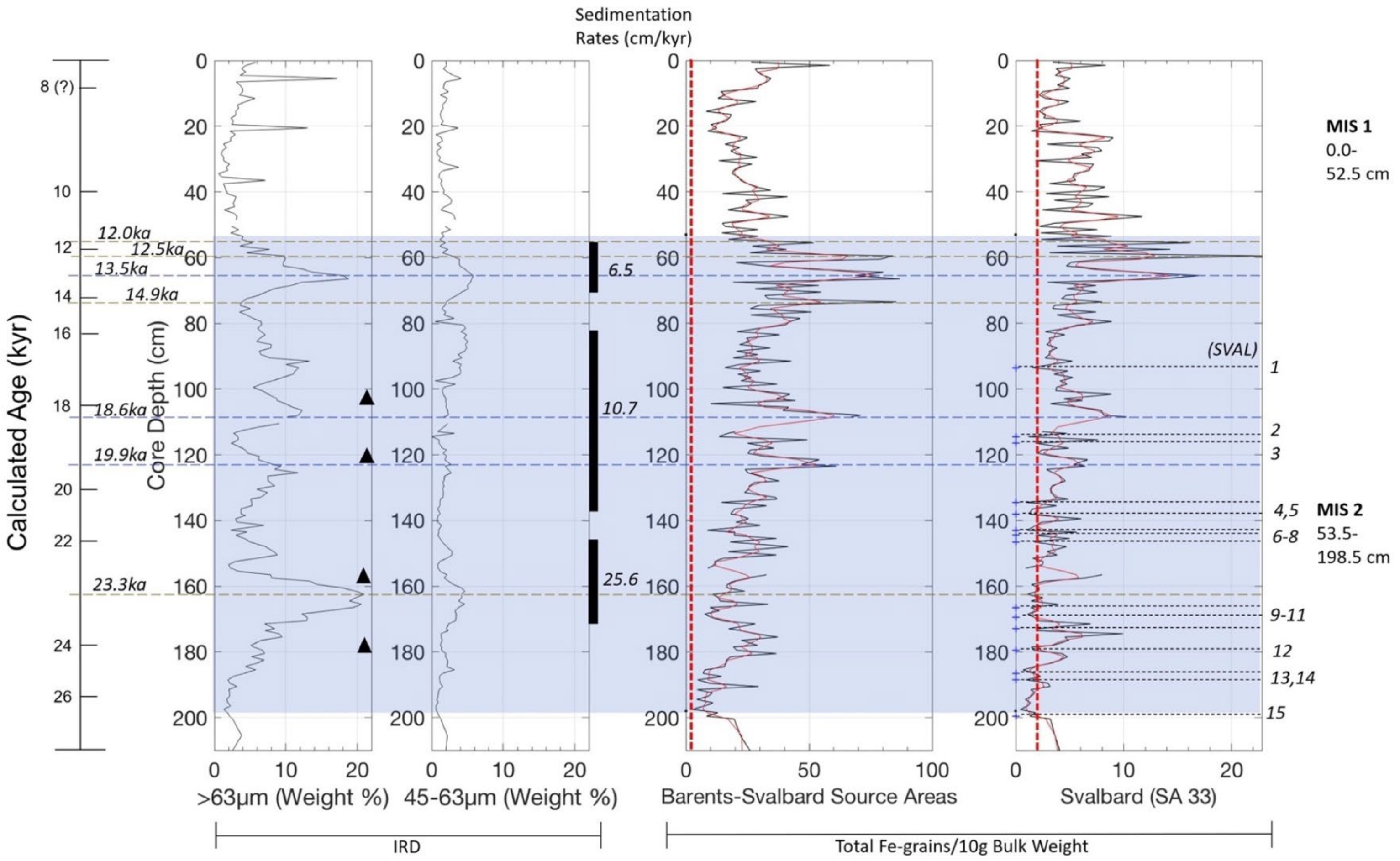

Fig. 20. Barents-Svalbard SA Groups Fe-grain numbers (from Fig. 15) and IRD (from Fig. 10). Figure shows IRD peaks generally aligned to Fe-grain peaks (blue dashed line), either an IRD or Fe-grain peak without a corresponding peak (brown dashed line), hiatuses (black dashed lines) (from Table 2), foram peaks (solid triangles) (from Fig. 11), 5-cm boxcar smoothed Fe-grains (solid red line), and high sedimentation rates (black bars with associated rates) (from Figs. 7, 8, and 9).

There is constant BSIS Fe-grain transport throughout MIS 4 with peaks at 65.4 ka and 63.3 ka (Fig. 21). The only IRD peak that aligns with Fe-grain peaks is the >63 µm IRD peak at 63.3 ka. The Fe-grain peak at 65.4 ka lacks a distinct corresponding IRD peak, however some >63 µm IRD are present. During MIS 4, the BSIS experiences two calving events: a less pronounced event at 65.4 ka, and a primary calving event at 63.3 ka. The lack of multiple calving events may indicate the BSIS was smaller during MIS 4 with several sea ice-rafting events.

During MIS 6, IRD and Fe-grains peak at 175.0 ka with 60 Fe-grains/10 g bulk weight, and a corresponding >63 µm IRD peak (Fig. 21). Together, this indicates a large BSIS calving event. SA 32 (west of Franz Josef Land) is one of the regions with high Fe-grain numbers during the 175.0 ka Fe-grain peak. Fe-grains show a hiatus cluster from 155.0-169.1 ka (14.1 kyr), however >63 µm IRD are still present during this period, indicating that ice-rafting from other areas occurred during the Fe-grain hiatus from the BSIS (Table 3). At 152.8 ka, the >63 µm IRD corresponds with minor peaks in Fe-grains. There's another hiatus cluster near the MIS 6 termination from 130.8-148.2 ka (BSVL1-6) lasting 17.8 kyr (Tables 3 and 11).

Possible explanations for the MIS 6 hiatuses are an absence of the BSIS, a lack of Fe-grain transport events, or low melt out rates near the core location. Lower sedimentation rates in MIS 6 suggest colder conditions and less melt-out than for MIS 2 and 4 on the Yermak Plateau in Fram Strait (Fig. 9 and Table 1). However, while Fe-grains are nearly absent during hiatus clusters, IRD is present and corresponds to high deposition. Therefore, these Fe-grain hiatuses do not indicate a lack of melt out. Models indicate the BSIS was present during MIS 6 (Batchelor et al., 2019). If the BSIS was not present during the hiatus clusters, it would need to rebuild following the hiatuses to explain the Fe-grain peaks. A more plausible scenario is the BSIS was present through MIS 6, especially through the hiatus clusters, but did not exhibit any collapses or produce large calving events besides the 175-ka event. During the remainder of MIS 6, the BSIS does not have any additional calving events. No further Fe-grain events are observed until MIS5e suggesting the BSIS possibly did not finally collapse until MIS 5.

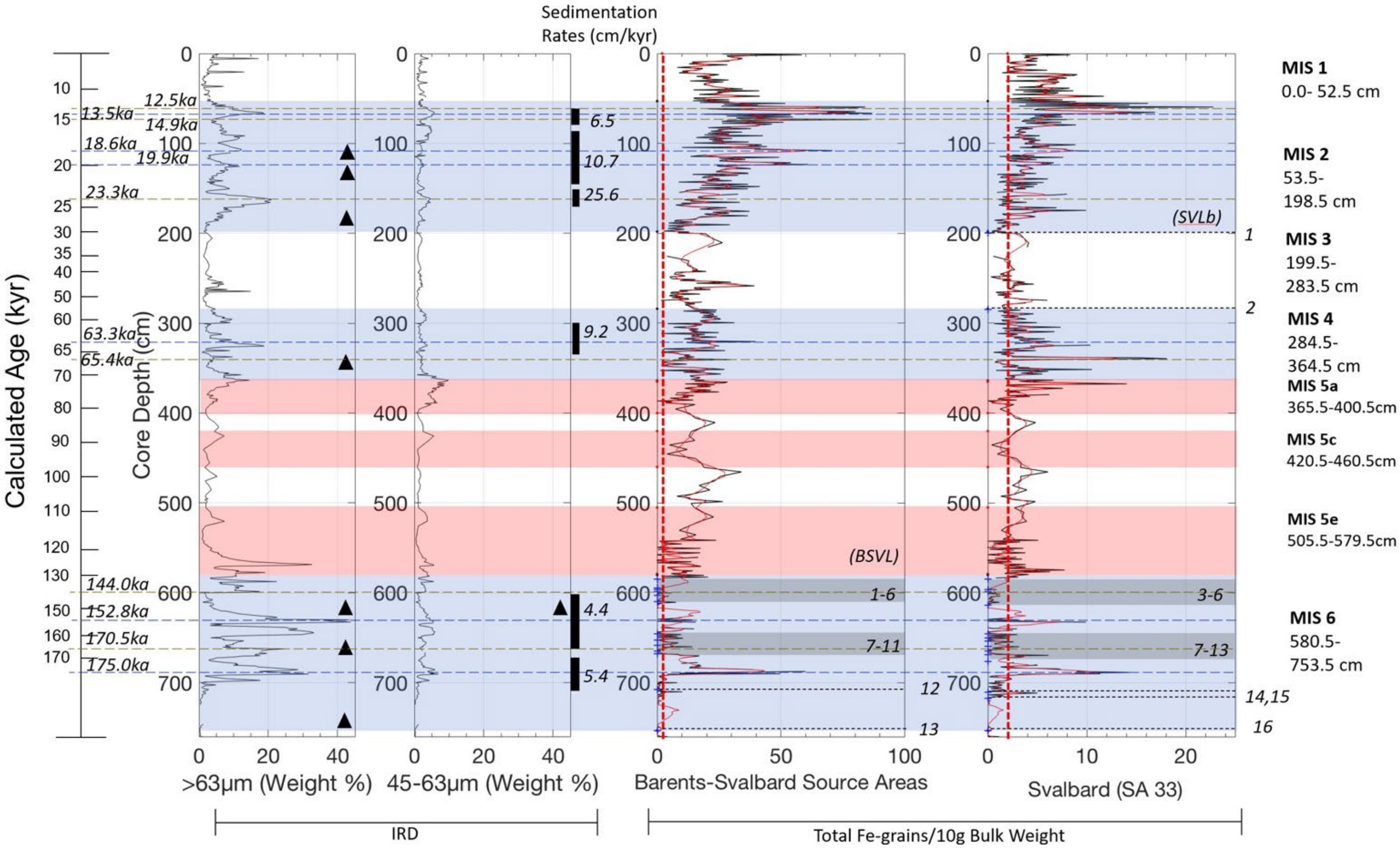

Fig. 21. Barents-Svalbard SA Groups Fe-grain numbers (from Fig. 16) and IRD (from Fig. 10). Figure shows IRD peaks generally aligned to Fe-grain peaks (blue dashed line), either an IRD or Fe-grain peak without a corresponding peak (brown dashed line), hiatuses (black dashed lines) (from Table 3), hiatus clusters (gray shaded) (from Table 11), foram peaks (solid triangles) (from Fig. 11), 5-cm boxcar smoothed Fe-grains (solid red line), and high sedimentation rates (black bars with associated rates) (from Figs. 7, 8, and 9).

5.3 WESTERN ARCTIC OCEAN

Models indicate the Beaufort Sea was not covered by a large ice sheet, but a SIM may have been present (Batchelor et al., 2019). There are no hiatuses of Fe-grains from the Beaufort Sea SAs during MIS 2 and Fe-grains are constantly transported from this region (Figs. 17 and 22). This precludes a long period of ice build-up required for a SIM here. Likewise, because this shelf was exposed during MIS 2, icebergs could not ground here and form an ice mass.

Fe-grains from the Beaufort Sea peak at 24.8 ka, only ~4 kyr after MIS 2 begins (Fig. 22). However, the >63 µm IRD peak occurs at 23.3 ka. The two peaks at 19.9 ka and 18.6 ka for all western Arctic SAs are the same age as the BSIS initial collapse. The 18.6 ka Fe-grain peak might indicate a partial collapse of a possible SIM, followed by a final collapse at 13.4 ka. The Beaufort Sea SA Group includes SA 8, which has strong influences from the LIS because the Fe-grain numbers for this one source are far greater than the other western Arctic sources. It is quite possible that the 18.6 ka Fe-grain peak represents the LIS collapse, and not a potential SIM collapse.

After the 23.3 ka >63 µm IRD peak, there are minor IRD peaks before a final peak at 13.4 ka, which aligns with Fe-grain peaks. This series of peaks could indicate an increase in sea-ice formation due to progressively colder conditions or continuous calving from a SIM. However, continuous Fe-grain transport and calving conditions would make SIM build-up more difficult. If a SIM was developing, Fe-grains would likely be low or in decline, rather than experiencing a gradual increase. More likely, this could indicate a plateau in sea-ice entrainment followed by a peak in production of dirty sea ice. Any sea ice would have to form at the shelf margins due to lower sea level. The Fe-grain sources would be the same as if sea level were higher, as a drop in sea level would most likely transport sediment offshore. Wrangel Island and the New Siberian

Islands in the East Siberian Sea have a similar Fe-grain trend to the Beaufort Sea throughout MIS 2, with no hiatuses in Fe-grain transport.

Fe-grain data suggest that if a SIM was present in either the East Siberian Sea or the Beaufort Sea during MIS 2, then they would have to have built up in less than 1-2 kyr. Wrangel Island and the New Siberian Islands SAs and Beaufort Sea SAs provide high numbers of Fe-grains throughout MIS 2, with peaks ranging from 58-94 Fe-grains/10 g bulk weight, but the >63 µm IRD peaks that coincide with Fe-grain peaks are generally small and <10 %.

One scenario is that SIMs gradually built up in the Beaufort Sea and East Siberian Sea from the MIS 2 initiation until 18.6 ka, partially collapsed at this time, rebuilding to 13.4 ka, and collapsing near MIS 2 termination. The continuous supply of IRD from a building SIM would require a rather high precipitation rate on these shelves during a glacial interval. Modelling studies do not support this argument and predict even lower precipitation than during warmer interglacial periods, however they cannot rule out localized increases in precipitation (Sikorski et al., 2008; Miller et al., 2010a, 2010b). Given these possible scenarios and multiple caveats, SIMs probably did not exist in the Western Arctic Sources of the Beaufort Sea and the East Siberian Shelf during MIS 2.

Fe-grain transport from the Beaufort Sea and East Siberian Sea is constant throughout MIS 4 with no hiatuses (Fig. 22). Constant Fe-grains suggest that ice-rafting during MIS 4 is less dynamic than MIS 2, with nearly continuous transport through MIS 4, especially 45-63 µm. This is more typical of sea ice-rafting than calving from an ice mass. Previous studies proposed a possible SIM near the Beaufort Sea but show an ice-free East Siberian Sea during MIS 4 (Polyak et al., 2001; Jakobsson et al., 2008, 2010; Batchelor et al., 2019). The Fe-grain peaks at 67.6 ka and 63.3 ka in Beaufort Sea Sources indicate ice-rafting events, especially the 63.3 ka which has a corresponding >63 μm IRD peak, suggesting glacial origins. The shelves in this region are primarily fine-grained sediment, so the >63 μm IRD peak likely reflects other SAs besides Beaufort Sea or East Siberian Sea. The >63 μm IRD peak may also reflect sand-size sediment transported by longshore drift inner shelf of the Beaufort Sea has (Short et al., 1974; Darby et al., 2009b). Likewise, while these peaks are associated with large Fe-grain numbers (> 45 Fe-grains/10 g bulk weight), the peaks are not as distinct as MIS 2. These data suggest that a Beaufort Sea SIM is unlikely during MIS 4 and this area was a source of sea-ice entrainment.

MIS 6 was dominated by hiatuses, especially at its termination and during the middle of the stage (Fig. 22 and Table 4). Near MIS 6 initiation, Fe-grain peaks indicate transport from the Beaufort Sea and East Siberian Sea between 170.0-175.6 ka. There are corresponding IRD peaks in both 45-63 μm and 63-250 μm, and a minor >250 μm peak (Fig. 10). Fe-grain peaks with corresponding IRD peaks indicate a mixed transport event of sea ice and possible SIM calving events. These Fe-grain peaks are followed by substantial hiatus clusters. Hiatus clusters are identified in the Beaufort Sea 152.7-178.5 ka spanning 25.8 kyr (BFTS 7-13) and Wrangel Island and New Siberian Islands SAs 154.7-168.0 ka spanning 13.3 kyr (WINS 5-9) (Fig. 17 and Table 4). However, IRD transport is still present during these hiatuses. Near the end of this hiatus cluster, there is an IRD peak that corresponds with minor Fe-grains peaks in all Western Arctic sources at 157.6 ka. While Fe-grain peaks only average 10-16 Fe-grains/10 g bulk, IRD size fractions indicate Fe-grain transport prior to the first hiatus cluster may have been a mix of sea ice and glacial ice. After a period of minor Fe-grain peaks, an IRD peak occurs at 152.2 ka. The remainder of MIS 6 is primarily a second hiatus cluster from 132.2-148.0 ka (15.8 kyr) in the Beaufort Sea (BFTS 1-4) and 132.2-145.5 ka (15.8 kyr) in the East Siberian Sea (WINS 1-4). However, IRD are still present, even at MIS 6 termination, but not from the Beaufort Sea or East

Siberian Sea. No obvious collapse of a SIM in the western Arctic occurs near the end of MIS 6 until MIS 5e.

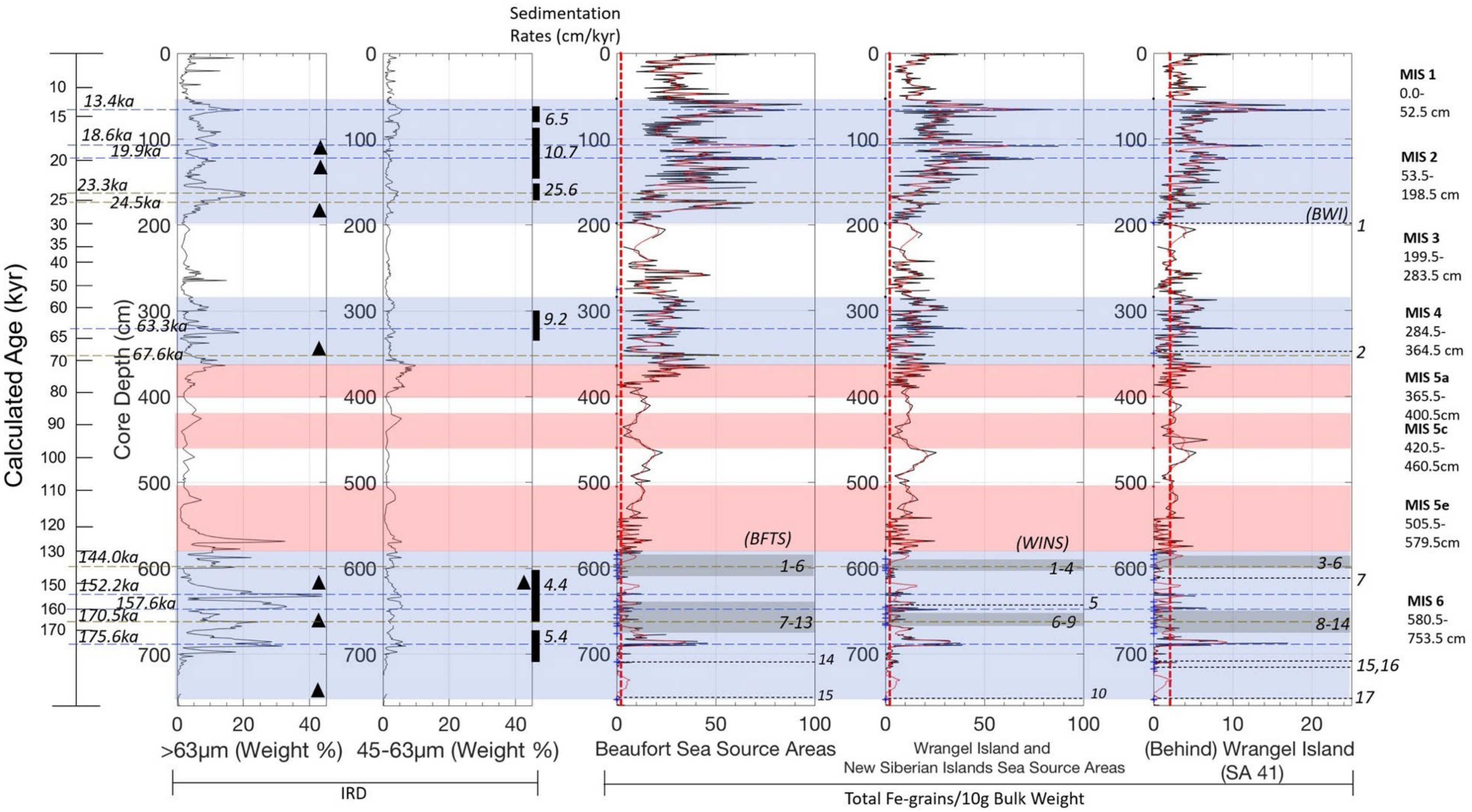

Fig. 22. Western SA Groups Fe-grain numbers (from Fig. 17) and IRD (from Fig. 10). Figure shows IRD peaks generally aligned to Fe-grain peaks (blue dashed line), either an IRD or Fe-grain peak without a corresponding peak (brown dashed line), hiatuses (black dashed lines) (from Table 4), and hiatus clusters (gray shaded) (from Table 11), foram peaks (solid triangles) (from Fig. 11), 5-cm boxcar smoothed Fe-grains (solid red line), and high sedimentation rates (black bars with associated rates) (from Figs. 7, 8, and 9).

5.4 CENTRAL ARCTIC OCEAN

Fe-grains during MIS 2 and MIS 4 did not indicate any hiatuses >1.00 kyr in any of the Beaufort Gyre Groups, TPD Groups, or Western Arctic SA Groups (Figs. 22, 23, and 24). A large ice mass in the central Arctic Ocean would likely inhibit IRD transport, thus resulting in a lack of Fe-grains from these regions. Depending on its spatial extent, thickness, and dynamics, a central Arctic ice mass would be expected to create hiatuses with durations >1.00 kyr. Additionally, low Fe-grain numbers throughout most of MIS 2 from Kara Sea rivers reflect discharges that were 20-30 % of current discharges due to ice blockage and drier conditions (Alkama et al., 2006) (Fig. 24). Despite decreases in Fe-grain numbers, a lack of hiatuses suggests no large ice mass existed in the central Arctic Ocean.

BG SA Groups (Bering Strait and Laptev Sea) have a series of distinct Fe-grain peaks at 25.3 ka, 23.0 ka, 22.4 ka and another large peak at 18.6 ka (Fig. 23). Only the peaks at 23 ka and 18.6 ka coincide with >63 µm IRD peaks, suggesting that the rest of these Fe-grain peaks are sea-ice events. After the 18.6 ka peak, there is another peak at 13.6 ka. Canadian Archipelago Fe-grains follow the same trend but lack the distinct Fe-grain peaks at 23.0 ka and 22.4 ka.

Fe-grains were nearly constant throughout MIS 4 with a minor peak at 63.3 ka that aligns with a >63 µm IRD peak. If a central Arctic ice mass would prevent Fe-grains from distal sources from reaching the core location, the abundant Fe-grain peaks from all BG SAs, TPD SAs, and Western SAs during MIS 2 suggest a lack of a central Arctic ice mass. Based on nearly continuous Fe-grains and IRDs and the absence of hiatuses in all BG SAs, TPD SAs, and Western SAs, a large central Arctic Ocean ice mass did not exist during MIS 2 and 4. Bering Strait Sources and Laptev Sources show an Fe-grain peak near the MIS 4 termination at 58.7 ka but lack a distinct corresponding IRD peak.

During MIS 6, there is one Fe-grain peak in MIS 6 across all TPD Groups, BG Groups, and Western Arctic Groups at 175.0 ka with a corresponding >63 μm IRD peak, and a minor fine-grained IRD peak (Figs. 22, 23, and 24). The Fe-grain peaks primarily corresponding with coarse-grained IRD peaks indicate wide-spread calving events across the Central Arctic and Western Arctic SA Groups. Like the previously identified large Fe-grain contributions from Barents-Svalbard SA 32, the Kara Sea SA 36 contributes the largest number of Fe-grains during the 175.0 ka peak (106 Fe-grains/10 g bulk weight). The Kara Sea contributions could be from the eastern portion of the BSIS (Fig. 1). Canadian Archipelago SAs also have high Fe-grain numbers reaching 126 Fe-grains/10 g bulk weight. Following this calving event, all Central Arctic SAs have two major clusters of Fe-grain hiatuses (Tables 12 and 13). The two hiatus clusters have an average age duration of 13.8kyr, during the middle of MIS 6 at 157.0-170.8 ka, and 16.1kyr near the termination of MIS 6 at 130.8-146.9 ka. While Fe-grains are low during the first hiatus cluster, coarse IRD remains constant and even peaks during this period. The first hiatus cluster is much less pronounced in the Canadian Archipelago SA Groups, and only spans < 3kyr compared to the hiatus cluster average of 13.8kyr (Fig. 23). Likewise, IRD during this period correspond to Fe-grains from some individual Canadian Archipelago sources, SA 4 (16 Fe-grains/10 g bulk weight) and SA 5 (8 Fe-grains/10 g bulk weight) (Figs. 2 and 13). Fe-grain transport from this Canadian SA is nearly continuous albeit low during the 157-170 ka hiatus (Fig. 23). The same is true for Kara Sea sources and BSIS sources.

After the first hiatus cluster, there are a series of minor Fe-grain peaks in the BG and TPD combined SAs starting around 157.6 ka, with large corresponding >63 μm IRD peaks (Figs. 23 and 24). Again, this may indicate another widespread, yet minor calving event or ice sheet collapses, as seen in most SAs examined in this study. IRD then decreases again near the beginning of the second Fe-grain hiatus cluster, possibly indicating a build-up of a central Arctic ice mass. However, coarse-grained IRD µm is not completely absent and even shows a minor peak near MIS 6 termination at 129.2 ka.

Given the nature of the widespread Fe-grain peaks at 175.0 ka and around 157.6 ka, and corresponding hiatus clusters found at nearly all SA Groups, MIS 6 ice transport must have been influenced by large-scale hiatuses lasting >14 kyr. The large presence of forams overlapping both hiatus clusters suggests melt out at the Fram Strait was not a limited factor (Figs. 11 and 12). The two >14 kyr hiatuses might have provided sufficient time for an ice mass to build somewhere in the central Arctic Ocean (perhaps the Lomonosov Ridge) but would require rather high precipitation rates that are not supported by modelling (Miller et al., 2010a, 2010b). Thus, only small SIMs would have sufficient time to develop during MIS 6, unless large ice masses can develop in less than 14 kyr under much lower precipitation conditions than today. However, the Fe-grain data might support grounding of large icebergs on the Lomonosov Ridge as proposed by Jakobsson et al. (2008, 2010). If these clusters of hiatuses are due to this ice mass on the Lomonosov Ridge, it disintegrated in two stages separated by 18 kyr starting at 175.6 ka. If central Arctic ice masses existed during MIS 6 hiatus clusters, they partially collapsed at 175.6 ka and 157.6 ka and showed no distinct collapse event before MIS 6 termination. There are no Fe-grain events until MIS5e, which suggests any central Arctic ice mass (mostly grounded icebergs or shelf ice) did not disintegrate until MIS 5 (Figs. 23 and 23).

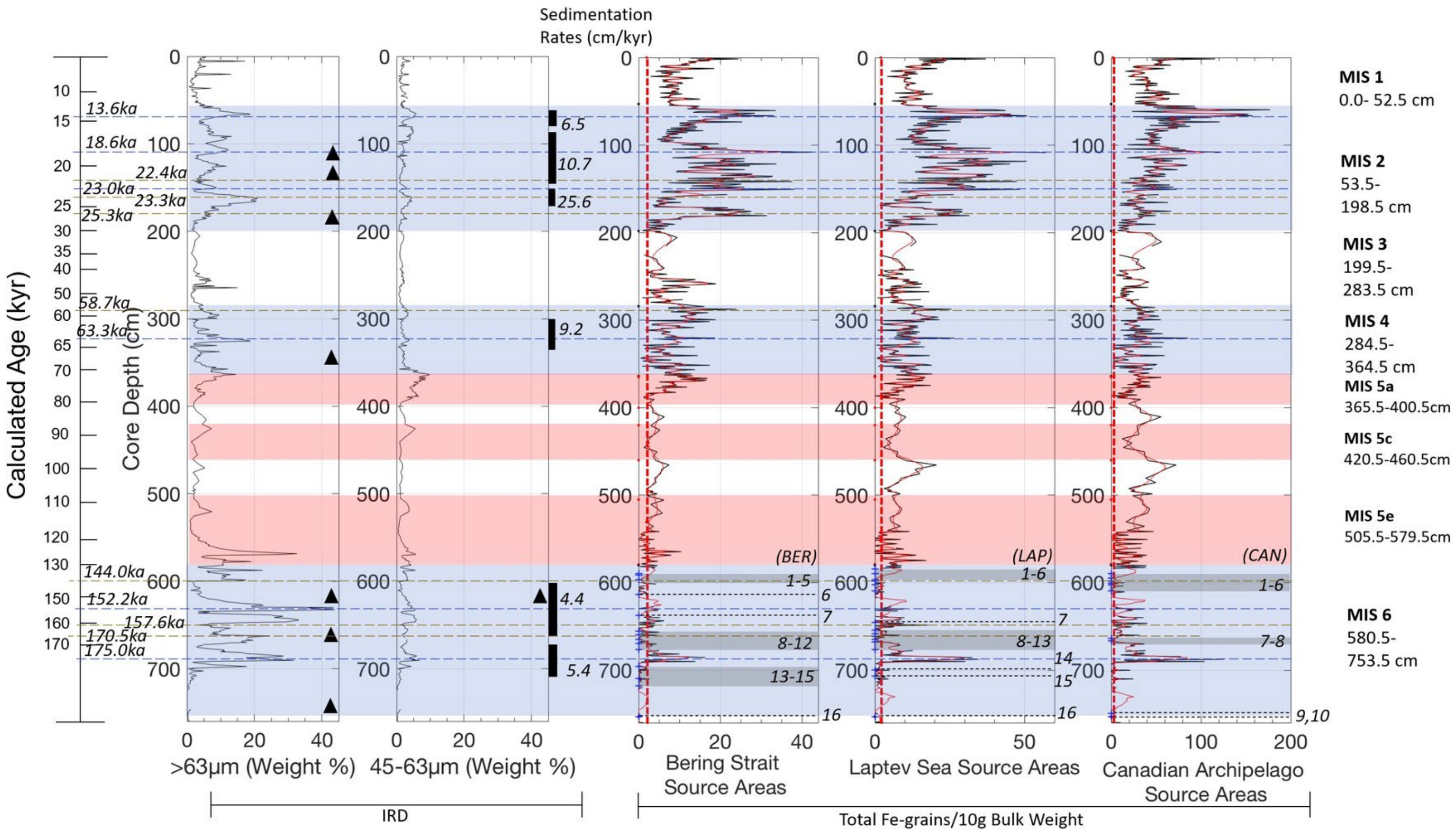

Fig. 23. Central Arctic (BG) SA Groups Fe-grain numbers (from Fig. 18) and IRD (from Fig. 10). Figure shows IRD peaks generally aligned to Fe-grain peaks (blue dashed line), either an IRD or Fe-grain peak without a corresponding peak (brown dashed line), hiatuses (black dashed lines) (from Table 5), and hiatus clusters (gray shaded) (from Table 11), foram peaks (solid triangles) (from Fig. 11), 5-cm boxcar smoothed Fe-grains (solid red line), and high sedimentation rates (black bars with associated rates) (from Figs. 7, 8, and 9).

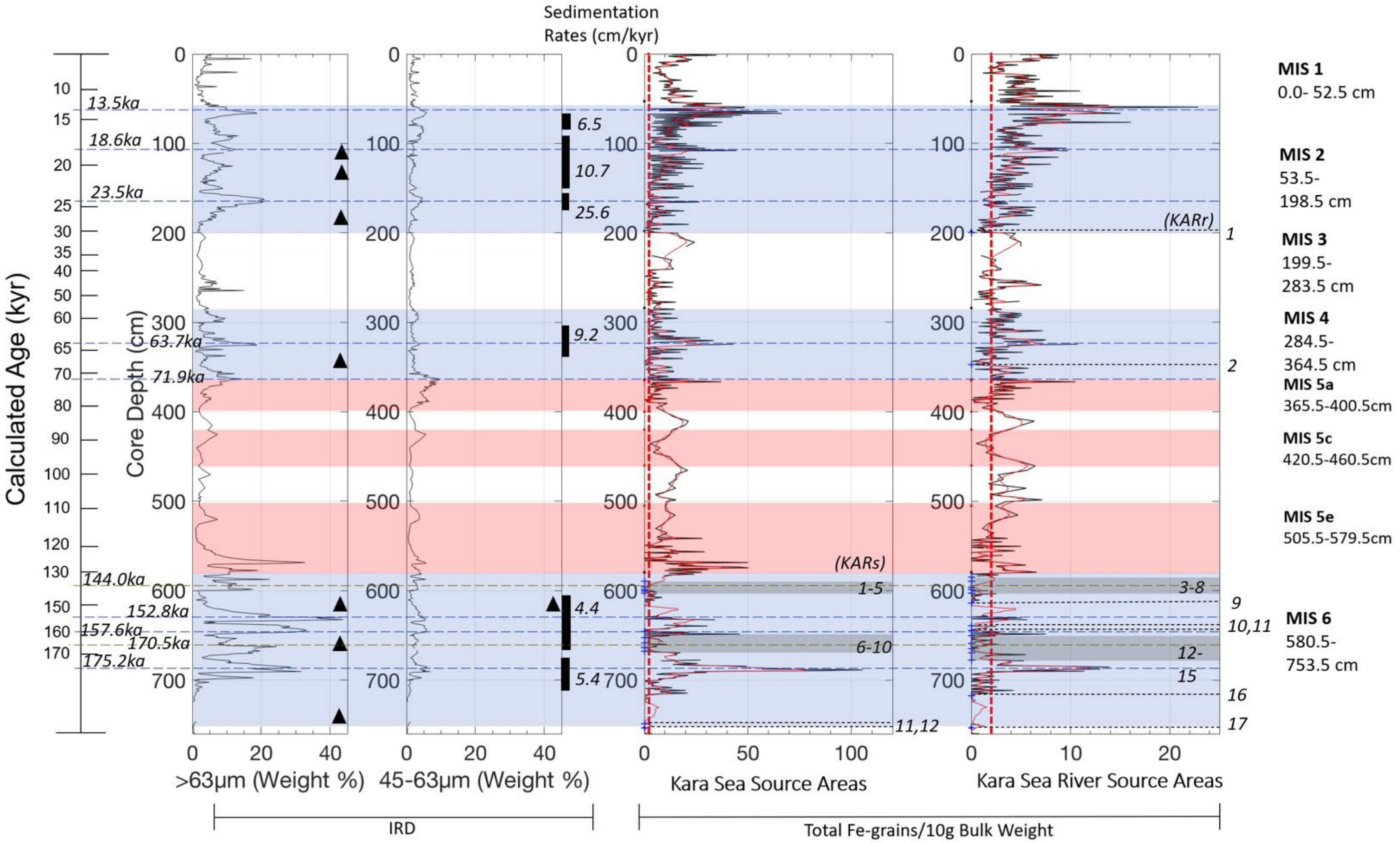

Fig. 24. Central Arctic (TPD) SA Groups Fe-grain numbers (from Fig. 19) and IRD (from Fig. 10). Figure shows IRD peaks generally aligned to Fe-grain peaks (blue dashed line), either an IRD or Fe-grain peak without a corresponding peak (brown dashed line), hiatuses (black dashed lines) (from Table 6), and hiatus clusters (gray shaded) (from Table 11), foram peaks (solid triangles) (from Fig. 11), 5-cm boxcar smoothed Fe-grains (solid red line), and high sedimentation rates (black bars with associated rates) (from Figs. 7, 8, and 9).

While IRD indicates melt out is occurring during MIS 6, the overall lower numbers of Fe-grains compared to later glacial intervals (MIS 2 and 4) suggests lower melt-out rates in Fram Strait. This is probably due to colder temperatures here than during subsequent glacial stages. To quantify this idea, hiatus durations are calculated as a percentage of time for each MIS. Table 7 shows the percentage of time during each MIS when there is a hiatus duration >1.0kyr. Hiatus durations are summed from Table 3, Table 4, and Table 5 to calculate: (1) the percent of time for each SA Group, or SA Subgroups; and (2) and the average percent of hiatus time per MIS.

Overall, hiatuses account for an average of 11 % of MIS 2, 9 % of MIS 4, and 54 % of MIS 6. Increased hiatuses and low sedimentation rates (Fig. 9 and Table 1) during MIS 6 also suggest low melt-out rates in Fram Strait. Low melt out rates could impact the sizes of IRD deposition. While this study does not address this concept, it is possible only >63 μm IRD is deposited by winnowing currents, or that finer-grained IRD was not entrained through freezing.

Table 7. Central Arctic Source Area Groups Hiatus Durations as Percent during MIS 2, 4, and 6.

Stage	Source Area Groups	SA Subgroups	Total Hiatuses Duration	Total Stage Period	Time Hiatuses Present	Average Hiatus Time per MIS
			(kyr)	(kyr)	(%)	(%)
2	Western Arctic SA Groups		1.8		10.3	
2	BG SA Groups		NONE			
2	TPD SA Groups		2.0		11.5	
MIS 2 Total	All Central Arctic SA Groups			17.3		10.9
4	Western Arctic SA Groups		1.0		7.1	
4	BG SA Groups		NONE			
4	TPD SA Groups		1.4		9.9	
MIS 4 Total	All Central Arctic SA Groups			14.0		8.5
6	Western Arctic SA Groups	Beaufort Sea	34.4		56.4	
		Wrangel Island and New Siberian Islands	23.4		38.4	
		Behind Wrangel Island	44.7		73.3	
6	BG SA Groups	Bering Strait	40.0		65.6	
		Laptev Sea	35.0		57.4	
		Canadian Archipelago	21.3		34.9	
6	TPD SA Groups	Kara Sea	22.3		36.6	
		Kara Sea Rivers	41.4		67.8	
MIS 6 Total	All Central Arctic SA Groups			61.0		53.8

CHAPTER 6

CONCLUSIONS

6.1 STUDY SUMMARY

This study analyzes the circum-Arctic provenance of Fe-grains that are transported by Arctic ice as a proxy for ice movement in the Arctic Ocean during the past three glacial maxima (MIS 2, 4, and 6) with three objectives:

- Describe how the Barents-Svalbard ice sheet behaved during the LGM (MIS 2), as well as MIS 4 and 6, and when and how it retreated during each of these stages.
- Determine the presence and/or ages of SIMs on the East Siberian shelf near Wrangel Island, New Siberian Islands, and shelf areas of the Beaufort Sea during MIS 2, 4, and/ or 6, or at least determine when SIMs disintegrated if they existed.
- Identify if large ice masses existed in the central Arctic Ocean during MIS 2, 4, and/ or 6 that might reduce or prevent ice-rafting.

An age model is developed based on the K_{ARM}/K magnetic grain size proxy (Xuan et al., 2011) and Vostok $\delta^{18}O$ data through MIS 6 (Fig. 4). The age model provides corresponding dates for core depths to calculate sedimentation rates and assign MIS (Figs. 7, 8, and 9, and Table 1).

This study supplements primary Fe-grain proxy analysis with IRD weight percent fractions, foram abundances, and an SEM quartz grain analysis test.

6.2 BARENTS-SVALBARD ICE SHEET

Based on the Fe-grain numbers, the BSIS developed between MIS 2 initiation (29 ka) and its partial collapse at 19.9 ka and 18.6 ka (Fig. 20). Following these two partial collapses, the BSIS either slowly rebuilt or enhanced sea ice conditions prevented subsequent ice-rafting (Patton et al., 2015) before a series of Fe-grain events at 14.9 ka, 13.5 ka, and 12.5 ka. The collapse starting at 14.9 ka is not detected in cores closer to Svalbard but is seen in a core farther east near Franz Josef Land (Patton et al., 2015) (Fig. 1). Likewise, the 14.9 ka peak lacks a distinct coarser-grained >63 µm IRD peak, but finer-grained IRD are present, indicating a sea ice-rafting event. The final MIS 2 BSIS collapse occurs at 13.5 ka and 12.5 ka, again as a two-pulse event. Previous studies did not recognize these dual pulse collapses (Patton et al., 2015).

During MIS 4 (57-71 ka), the BSIS experienced two calving events: a less pronounced event at 65.4 ka, and a second primary event at 63.3 ka, possibly indicating a small collapse of the BSIS near the end of MIS 4 (Fig. 21). The lack of multiple calving events may indicate the BSIS overall size and volume was smaller during MIS 4. The Fe-grains peaks near MIS 4 termination may indicate the final MIS 4 BSIS collapse; however, these are primarily from the Bering Strait and Laptev Sea, around 58.7 ka.

During MIS 6 (130-191 ka), the BSIS has a calving event at 175.0 ka, followed by a hiatus of Fe-grain transport events, then a smaller calving period at 152.8 ka (Fig. 21, Tables 3 and 11). Hiatuses are not interpreted as an absence of the BSIS, but rather a lack of transport, collapse, or large calving events. The BSIS does not have any additional Fe-grain transport events through MIS 6 termination. It is possible the BSIS collapsed around 175.0 ka, then remained constant through MIS 6, with one calving event at 152.8 ka, with a potential collapse not occurring until MIS 5.

6.3 WESTERN ARCTIC OCEAN SIMS

During MIS 2, there are no hiatuses in Fe-grains from western Arctic sources (Fig. 22 and Table 4). Therefore, the near continuous rafting of Fe-grains with multiple peaks and IRD from these western Arctic sources makes a SIM build-up very difficult. Fe-grains increase with several minor peaks from MIS 2 initiation to 18.6 ka (Fig. 22). This Fe-grain peak in the Beaufort Sea SA, indicating a sizeable transport period, indicates a partial collapse of a possible SIM or a sea-ice event. The partial collapse may be followed by a gradual rebuilding to 13.4 ka before collapsing before MIS 2 termination. More likely, this indicates a plateau in sea-ice entrainment followed by a peak in production of dirty sea-ice. If a SIM developed in this region, it would have been constrained to a 1-2 kyr build-up with large IRD transport throughout its existence. However, the continuous IRD supply from such a SIM and a brief build-up period requires high precipitation rates. Modelling does not support but cannot rule out localized increases in precipitation (Sikorski et al., 2008; Miller et al., 2010a and b). Because most of the Fe-grains from the western Arctic sources is from SA 8, the most likely scenario is that the IRD represents calving from the LIS.

Likewise, the continuous transport of Fe-grains throughout MIS 4 from the Beaufort Sea and East Siberian Sea precludes any large ice mass or SIM on these shelves (Fig. 22). If SIMs did develop on the Beaufort Sea shelves or East Siberian Shelves, they collapsed or calved frequently to allow IRD transport from these shelves. Because these shelves contain mostly finer-grained sediment, it is difficult to distinguish sea ice-rafting from shelf mass ice calving/wasting. SIMs could develop more rapidly than a few thousand years if large icebergs from the Laurentide Ice Sheet or other land ice masses could ground on these shelf areas and provide seed ice for SIM growth, but lower sea levels prevented this. Thus, SIMs did not exist on the East Siberian or Beaufort shelves during MIS 4.

During MIS 6, the Beaufort Sea and East Siberian Sea show Fe-grain transport at 175.6 ka with both coarse (>63 µm) and fine (45-63 µm) IRD indicating a potential mix of sea ice and glacial ice (Fig. 22). Therefore, Fe-grain peaks from the Beaufort Sea area may be more indicative of disintegration events than sea ice-rafting. Like the Barents-Svalbard SAs, there are several clustered hiatuses (Table 4 and 11). Following the Fe-grain transport event at 175.6 ka, there are hiatus clusters in the Beaufort Sea (152.7-178.5 ka) and East Siberian Sea (154.7-168.0 ka). Near the end of the East Siberian hiatus cluster, there is an Fe-grain transport event at 157.6 ka. While this Fe-grain peak does not have a corresponding IRD peak, there is an IRD peak shortly after at 152.2 ka, which indicates similar ice transport as the previous IRD peak, a mix of sea ice and glacial ice. MIS 6 has a significant hiatus through the remainder of the stage, from 132.2 ka to 148.0 ka in the Beaufort Sea and 132.2 ka to 145.5 ka in the East Siberian Sea.

These hiatus clusters suggest a SIM could have built up on the Beaufort Sea and East Siberian Sea shelves during these respective MIS 6 intervals. If a SIM built up during the MIS 6 hiatus clusters, the Fe-grain transport events (175.6 ka and 157.6 ka) may indicate collapse events of these SIMs, particularly with a mix of calving events and sea ice export events.

6.4 CENTRAL ARCTIC OCEAN

Nearly continuous Fe-grains from the TPD and BG sources, including all Western Arctic sources, and high IRD indicate a large central Arctic Ocean ice mass did not exist during MIS 2 and 4 (Figs. 22, 23, and 24). There is insufficient time for one to develop and there is more or less continuous IRD transport across the central Arctic.

During MIS 6, Fe-grains have significantly lower numbers than MIS 2 and 4, but there is one Fe-grain peak across all TPD Groups, Beaufort Gyre Groups, and Western Arctic Groups at ~175.0 ka with a >63 µm IRD peak, indicating wide-spread calving events from central Arctic SA Groups (Figs. 22, 23, and 24). If a central Arctic ice mass existed at 175.0 ka, the widespread calving events would likely not reach the core location.

TPD Groups, most BG Groups, and Western Arctic Groups had two major clusters of Fe-grain hiatuses with average age ranges of 157.0 ka to 170.8 ka lasting 13.8 kyr, during the middle of MIS 6, and 130.8 ka to 146.9 ka lasting 16.1kyr, near the termination of MIS 6 (Tables 4, 5, and 6). Minor Fe-grain peaks at 157.6 ka with a large corresponding >63 µm IRD peak may indicate another wide-spread calving event or ice sheet collapse, but much less significant than the 175.0 ka event. Decreasing IRD near the beginning of the second Fe-grain hiatus cluster might indicate a build-up of a central Arctic ice mass, but there are no Fe-grain events until MIS 5e.

The two >14 kyr hiatuses could also suggest a large iceberg armada grounding on the Lomonosov Ridge, and partially disintegrating at 157.6 ka. During MIS 6, it is possible a central ice mass existed during an average range of 157.0 ka to 170.8 ka, with a partial collapse at 157.6 ka, then rebuilding from 130.8 ka to 146.9 ka with no distinct collapse event before MIS5e.

Finally, the combined >63 µm IRD and Fe-grain peaks in the last three glacial stages indicate ice sheet collapses where they existed near the middle of stages and often again near the termination. MIS 4 is a weak glacial stage with smaller ice sheets than MIS 2 and especially MIS 6. Generally, MIS 4 was less severe than MIS 2 with less Fe-grain and thus IRD transport, corresponding to lower coarse peaks in >63 µm fractions. The only ice mass that existed in the central Arctic was during MIS 6 and it probably consisted of grounded icebergs or shelf ice that reached the Lomonosov Ridge. SIMs on the Beaufort Shelf or East Siberian Shelf are problematic during MIS 2 and 4 but could have existed during MIS 6 where the data is inconclusive.

6.5 FUTURE WORK

The data collected for this study provide a rich, detailed history of Arctic climate through MIS 6. This study examined three broad, large-scale objectives. Data from these 41 SAs could provide even more detailed spatial and temporal information related to unique regions of ice sheets, SIMs, calving fronts, ice streams, and sea ice. For example, examining SAs specifically adjacent to Arctic rivers, especially at a higher resolution, may provide information related ice export events and a better understanding of associated ice sheet dynamics. Direct comparison of ice export event timing across circum-Arctic regions may shed light on unknown feedback loops or unique climate conditions either during glacial periods, or during climate transitions. These results may be especially useful if combined or compared to paleoclimate ice modeling studies. With this fully developed dataset, it would also be useful to revisit the IRD, especially the peaks with no associated SA Group Fe-grain peaks and identify which individual SAs contributed to the IRD. This study provided some general context for associated SAs, but these data would be especially informative for multiple IRD peaks during MIS 6. One item that would be especially helpful for communicating these complex data would be an interactive ArcGIS map that allows a user to navigate through time and view visual representations of IRD amounts and Fe-grains numbers for all 41 SAs. Ideally, this could be coupled with an ice modelling study to include ice edge limits and possibly ice export events and animated ocean currents through MIS 6.

While this study partitioned IRD into size fractions representing two modes of transportation, sea ice and glacial ice, additional methods distinguishing these transportation modes would improve this provenance interpretation. This would be useful for future methods to differentiate SIMs from sea ice and glacial ice. Additional SEM analysis of the >250 µm quartz grains could help differentiate glacial from sea-ice IRD. Another factor differentiating SIMs from sea ice is a precipitation requirement. Ideally, paleoclimate proxies that could help constrain temporal and spatial precipitation patterns, especially in the East Siberian Sea, would help confirm the interpreted presence of SIMs.

REFERENCES

Aagaard, K., Carmack, E.C., 1989. The role of sea ice and other fresh water in the Arctic circulation. J. Geophys. Res. Oceans. 94, 14485-14498.

Alkama, R., Kageyama, M., Ramstein, G., 2006. Freshwater discharges in a simulation of the Last Glacial Maximum climate using improved river routing. Geophys. Res. Lett. 33.

Basilyan, A., Nikol'skyi, P., Maksimov, F., Kuznetsov, V.Y., 2010. Age of cover glaciation of the New Siberian islands based on ^{230}Th/U-dating of mollusk shells. Structure and Development of the Lithosphere, Paulsen, Moscow, 506-514.

Batchelor, C.L., Margold, M., Krapp, M., Murton, D.K., Dalton, A.S., Gibbard, P.L., Stokes, C.R., Murton, J.B., Manica, A., 2019. The configuration of Northern Hemisphere ice sheets through the Quaternary. Nat. Commun. 10, 3713.

Bence, A.E., Albee, A.L., 1968. Empirical correction factors for the electron microanalysis of silicates and oxides. Geol. J. 76, 382-403.

Bond, G., Heinrich, H., Broecker, W., Labeyrie, L., McManus, J., Andrews, J., Huon, S., Jantschik, R., Clasen, S., Simet, C. Tedesco, K., 1992. Evidence for massive discharges of icebergs into the North Atlantic Ocean during the last glacial period. Nature. 360, 245-249.

Bond, G., Broecker, W., Johnsen, S., McManus, J., Labeyrie, L., Jouzel, J., Bonani, G., 1993. Correlations between climate records from North Atlantic sediments and Greenland ice. Nature. 365, 143-147.

Bond, G.C., Lotti, R., 1995. Iceberg discharges into the North Atlantic on millennial time scales during the last glaciation. Science. 267, 1005-1010.

Bond, G., Kromer, B., Beer, J., Muscheler, R., Evans, M.N., Showers, W., Hoffmann, S., Lotti-Bond, R., Hajdas, I., Bonani, G., 2001. Persistent solar influence on North Atlantic climate during the Holocene. Science. 294, 2130-2136.

Bradley, R.S., England, J.H., 2008. The Younger Dryas and the sea of ancient ice. Quat. Res. 70, 1-10.

Broecker, W.S., 1975. Floating glacial ice caps in the Arctic Ocean. Science. 188, 1116-1118.

Broecker, W.S., 1994. Massive iceberg discharges as triggers for global climate change. Nature. 372, 421-424.

Carlson, A., 2011. Ice sheets and sea level in Earth's past. Nat. Ed. Knowl. 3, 3.

Colleoni, F., Liakka, J., Krinner, G., Jakobsson, M., Masina, S., Peyaud, V., 2011. The sensitivity of the Late Saalian (140 ka) and LGM (21 ka) Eurasian ice sheets to sea surface conditions. Clim. Dyn. 37, 531-553.

Colleoni, F., Kirchner, N., Niessen, F., Quiquet, A., Liakka, J., 2016. An East Siberian ice shelf during the Late Pleistocene glaciations: Numerical reconstructions. Quat. Sci. Rev. 147, 148-163.

Dahlgren, K.T., Vorren, T.O., 2003. Sedimentary environment and glacial history during the last 40 ka of the Vøring continental margin, mid-Norway. Mar. Geol. 193, 93-127.

Darby, D.A., 2003. Sources of sediment found in sea ice from the western Arctic Ocean, new insights into processes of entrainment and drift patterns. J. Geophys. Res. Oceans. 108.

Darby, D.A., Bischof, J.F., Jones, G.A., 1997. Radiocarbon chronology of depositional regimes in the western Arctic Ocean. Deep-Sea Res. III. 44, 1745-1757.

Darby, D.A., Polyak, L., Bauch, H.A., 2006. Past glacial and interglacial conditions in the Arctic Ocean and marginal seas-a review. Prog. Oceanogr. 71, 129-144.

Darby, D.A., Zimmerman, P., 2008. Ice-rafted detritus events in the Arctic during the last glacial interval, and the timing of the Innuitian and Laurentide ice sheet calving events. Polar Res. 27, 114-127.

Darby, D.A., Polyak, L., Jakobsson, M., 2009a. The 2005 HOTRAX expedition to the Arctic Ocean. Glob. Planet Change. 68, 1-4.

Darby, D., Ortiz, J., Polyak, L., Lund, S., Jakobsson, M., Woodgate, R., 2009b. The role of currents and sea ice in both slowly deposited central Arctic and rapidly deposited Chukchi–Alaskan margin sediments. Glob. Planet Change. 68, 58-72.

Darby, D.A., Myers, W.B., Jakobsson, M., Rigor, I., 2011. Modern dirty sea ice characteristics and sources: The role of anchor ice. J. Geophys. Res. Oceans. 116.

Darby, D.A., Ortiz, J.D., Grosch, C.E., Lund, S.P., 2012. 1,500-year cycle in the Arctic Oscillation identified in Holocene Arctic sea-ice drift. Nat. Geosci. 5, 897-900.

Darby, D.A., Myers, W., Herman, S., Nicholson, B., 2015. Chemical fingerprinting, a precise and efficient method to determine sediment sources. J. Sediment. Res. 85, 247-253.

Darby, D.A., Andrews, J.T., Belt, S.T., Jennings, A.E., Cabedo-Sanz, P., 2017. Holocene cyclic records of ice-rafted debris and sea ice variations on the East Greenland and Northwest Iceland margins. AAAR. 49, 649-672.

Denton, G., 1981. The Arctic ice sheet; an outrageous hypothesis. John Wiley & Sons, New York, NY, pp. 437-467.

Dickson, R., Osborn, T., Hurrell, J., Meincke, J., Blindheim, J., Adlandsvik, B., Vinje, T., Alekseev, G., Maslowski, W., 2000. The Arctic ocean response to the North Atlantic Oscillation. J. Clim. 13, 2671-2696.

Dong, L., Liu, Y., Shi, X., Polyak, L., Huang, Y., Fang, X., Liu, J., Zou, J., Wang, K., Sun, F., 2017. Sedimentary record from the Canada Basin, Arctic Ocean: implications for late to middle Pleistocene glacial history. Clim. Past. 13, 511-531.

Donn, W.L., Ewing, M., 1966. A Theory of Ice Ages III: The theory involving polar wandering and an open polar sea is modified and given a quantitative basis. Science. 152, 1706-1712.

Dove, D., Polyak, L., Coakley, B., 2014. Widespread, multi-source glacial erosion on the Chukchi margin, Arctic Ocean. Quat. Sci. Rev. 92, 112-122.

Dowdeswell, J.A., Vogt, P.R., Crane, K., Sundvor, E., 1995. Deep Pleistocene iceberg plowmarks on the Yermak Plateau: Sidescan and 3.5 kHz evidence for thick calving ice fronts and a possible marine ice sheet in the Arctic Ocean. Geol. J. 23, 476-478.

Dowdeswell, J., Ottesen, D., Evans, J., Cofaigh, C., Anderson, J., 2008. Submarine glacial landforms and rates of ice-stream collapse. Geol. J. 36, 819-822.

Dyke, A.S., Prest, V.K., 1987. Late Wisconsinan and Holocene history of the Laurentide ice sheet. Géogr. phys. quat. 41, 237-263.

Dyke, A., Andrews, J., Clark, P., England, J., Miller, G., Shaw, J., Veillette, J., 2002. The Laurentide and Innuitian ice sheets during the Last Glacial Maximum. Quat. Sci. Rev. 21, 9-31.

Elverhøi, A., Fjeldskaar, W., Solheim, A., Nyland-Berg, M., Russwurm, L., 1993. The Barents Sea Ice Sheet-a model of its growth and decay during the last ice maximum. Quat. Sci. Rev. 12, 863-873.

England, J., 1999. Coalescent Greenland and Innuitian ice during the Last Glacial Maximum: revising the Quaternary of the Canadian High Arctic. Quat. Sci. Rev. 18, 421-456.

Folk, R.L., 1980. Petrology of sedimentary rocks. Hemphill publishing company.

Grosswald, M., 1980. Late Weichselian ice sheet of northern Eurasia. Quat. Res. 13, 1-32.

Grosswald, M.G., Hughes, T.J., 1999. The case for an ice shelf in the Pleistocene Arctic Ocean. Polar Geogr. 23, 23-54.

Grosswald, M.G., Hughes, T.J., 2002. The Russian component of an Arctic ice sheet during the Last Glacial Maximum. Quat. Sci. Rev. 21, 121-146.

Grosswald, M.G., Hughes, T.J., 2008. The case for an ice shelf in the Pleistocene Arctic Ocean. Polar Geogr. 31, 69-98.

Heinrich, H., 1988. Origin and consequences of cyclic ice rafting in the northeast Atlantic Ocean during the past 130,000 years. Quat. Res. 29, 142-152.

Hughes, T., Denton, G.H., Grosswald, M., 1977. Was there a late-Würm Arctic ice sheet? Nature. 266.

Ingólfsson, Ó., Landvik, J.Y., 2013. The Svalbard–Barents Sea ice-sheet–Historical, current and future perspectives. Quat. Sci. Rev. 64, 33-60.

Jakobsson, M., 1999. First high-resolution chirp sonar profiles from the central Arctic Ocean reveal erosion of Lomonosov Ridge sediments. Mar. Geol. 158, 111-123.

Jakobsson, M., Løvlie, R., Arnold, E., Backman, J., Polyak, L., Knutsen, J.-O., Musatov, E., 2001. Pleistocene stratigraphy and paleoenvironmental variation from Lomonosov Ridge sediments, central Arctic Ocean. Glob. Planet Change. 31, 1-22.

Jakobsson, M., Polyak, L., Edwards, M., Kleman, J., Coakley, B., 2008. Glacial geomorphology of the central Arctic Ocean: the Chukchi Borderland and the Lomonosov Ridge. Earth Surf. Process Landf. 33, 526-545.

Jakobsson, M., Nilsson, J., O'Regan, M., Backman, J., Löwemark, L., Dowdeswell, J.A., Mayer, L., Polyak, L., Colleoni, F., Anderson, L.G., 2010. An Arctic Ocean ice shelf during MIS 6 constrained by new geophysical and geological data. Quat. Sci. Rev. 29, 3505-3517.

Jakobsson, M., Anderson, J.B., Nitsche, F.O., Dowdeswell, J.A., Gyllencreutz, R., Kirchner, N., Mohammad, R., O'Regan, M., Alley, R.B., Anandakrishnan, S., 2011. Geological record of ice shelf break-up and grounding line retreat, Pine Island Bay, West Antarctica. Geol. J. 39, 691-694.

Jakobsson, M., Mayer, L., Coakley, B., Dowdeswell, J.A., Forbes, S., Fridman, B., Hodnesdal, H., Noormets, R., Pedersen, R., Rebesco, M., 2012. The international bathymetric chart of the Arctic Ocean (IBCAO) version 3.0. Geophys. Res. Lett. 39.

Jakobsson, M., Ingolfsson, O., Long, A.J., Spielhagen, R.F., 2014a. The dynamic Arctic. Quat. Sci. Rev. 92, 1-8.

Jakobsson, M., Andreassen, K., Bjarnadóttir, L.R., Dove, D., Dowdeswell, J.A., England, J.H., Funder, S., Hogan, K., Ingólfsson, Ó., Jennings, A., 2014b. Arctic Ocean glacial history. Quat. Sci. Rev. 92, 40-67.

Jeffries, M.O., 1992. Arctic ice shelves and ice islands: Origin, growth and disintegration, physical characteristics, structural-stratigraphic variability, and dynamics. Rev. Geophys. 30, 245-267.

Johnsen, S.J., Dahl-Jensen, D., Dansgaard, W., Gundestrup, N., 1995. Greenland palaeotemperatures derived from GRIP bore hole temperature and ice core isotope profiles. Tellus B Chem. Phys. Meteorol. 47, 624-629.

Knies, J., Vogt, C., Stein, R., 1998. Late Quaternary growth and decay of the Svalbard/Barents Sea ice sheet and paleoceanographic evolution in the adjacent Arctic Ocean. Geo. Mar. Lett. 18, 195-202.

Landvik, J.Y., Bondevik, S., Elverhøi, A., Fjeldskaar, W., Mangerud, J., Salvigsen, O., Siegert, M.J., Svendsen, J.-I., Vorren, T.O., 1998. The Last Glacial Maximum of Svalbard and the Barents Sea area: ice sheet extent and configuration. Quat. Sci. Rev. 17, 43-75.

Levitan, M., Lavrushin, Y., 2009. Sedimentation history in the Arctic Ocean and subarctic seas for the last 130 kyr. Lecture Notes in Earth Sciences 118, 1-416.

Lisiecki, L.E., Raymo, M.E., 2005. A Pliocene-Pleistocene stack of 57 globally distributed benthic $\delta^{18}O$ records. Paleoceanography. 20.

Macdonald, R., Sakshaug, E., Stein, R., 2004. The Arctic Ocean: Modern status and recent climate change, In: Stein, R. and Macdonald, RW (Eds.), The Organic Carbon Cycle in the Arctic Ocean. Springer-Verlag, Berlin, pp. 6-21.

Mercer, J.H., 1970. A former ice sheet in the Arctic Ocean? Paleogeogr. 8, 19-27.

Milanković, M., 1920. Théorie mathématique des phénomènes thermiques produits par la radiation solaire. Gauthier-Villars et Cie.

Miller, G.H., Alley, R.B., Brigham-Grette, J., Fitzpatrick, J.J., Polyak, L., Serreze, M.C., White, J.W., 2010a. Arctic amplification: can the past constrain the future? Quat. Sci. Rev. 29, 1779-1790.

Miller, G.H., Brigham-Grette, J., Alley, R., Anderson, L., Bauch, H.A., Douglas, M., Edwards, M., Elias, S., Finney, B., Fitzpatrick, J.J., 2010b. Temperature and precipitation history of the Arctic. Quat. Sci. Rev. 29, 1679-1715.

Myers, W.B., Darby, D.A., 2015. A new age model for the Central Arctic reveals brief intervals of extreme sedimentation rates over the last 140 kyr. Arktos. 1, 1-20.

Myers, W.B., 2019. Circum-Arctic Mineralogy & Pan-Arctic Chronostratigraphy of Late Pleistocene Sediments: Developing a Comprehensive Age Model for the Western Arctic Ocean Using Unique Ice-Rafted Signals.

Myhre, A., Thiede, J., Firth, J., 1995. 1. North Atlantic-Arctic gateways, Proceedings Ocean Drilling Program Initial Reports.

Niessen, F., Hong, J.K., Hegewald, A., Matthiessen, J., Stein, R., Kim, H., Kim, S., Jensen, L., Jokat, W., Nam, S.-I., 2013. Repeated Pleistocene glaciation of the East Siberian continental margin. Nat. Geosci. 6, 842-846.

Nørgaard-Pedersen, N., Spielhagen, R.F., Erlenkeuser, H., Grootes, P.M., Heinemeier, J., Knies, J., 2003. Arctic Ocean during the Last Glacial Maximum: Atlantic and polar domains of surface water mass distribution and ice cover. Paleoceanography. 18.

Nørgaard-Pedersen, N., Mikkelsen, N., Lassen, S.J., Kristoffersen, Y., Sheldon, E., 2007. Reduced sea ice concentrations in the Arctic Ocean during the last interglacial period revealed by sediment cores off northern Greenland. Paleoceanography. 22.

Notholt, H., 1998. The implication of the ‘‘North East Water’’—Polynya on the sedimentation by NE-Greenland and late Quaternary paleo-oceanic investigations. Ber. Polar. 275, 182.

Nowaczyk, N.R., Frederichs, T.W., Kassens, H., Nørgaard-Pedersen, N., Spielhagen, R.F., Stein, R., Weiel, D., 2001. Sedimentation rates in the Makarov Basin, central Arctic Ocean: A paleomagnetic and rock magnetic approach. Paleoceanography. 16, 368-389.

O'Regan, M., Backman, J., Barrientos, N., Cronin, T.M., Gemery, L., Kirchner, N., Mayer, L.A., Nilsson, J., Noormets, R., Pearce, C., 2017. The De Long Trough: a newly discovered glacial trough on the East Siberian continental margin. Clim. Past. 13, 1269-1284.

Ottesen, D., Dowdeswell, J., Rise, L., Rokoengen, K., Henriksen, S., 2002. Large-scale morphological evidence for past ice-stream flow on the mid-Norwegian continental margin. Geol. Soc. Lond. spec. publ. 203, 245-258.

Patton, H., Andreassen, K., Bjarnadóttir, L.R., Dowdeswell, J.A., Winsborrow, M.C., Noormets, R., Polyak, L., Auriac, A., Hubbard, A., 2015. Geophysical constraints on the dynamics and retreat of the Barents Sea ice sheet as a paleobenchmark for models of marine ice sheet deglaciation. Rev. Geophys. 53, 1051-1098.

Petit, J.-R., Jouzel, J., Raynaud, D., Barkov, N.I., Barnola, J.-M., Basile, I., Bender, M., Chappellaz, J., Davis, M., Delaygue, G., 1999. Climate and atmospheric history of the past 420,000 years from the Vostok ice core, Antarctica. Nature. 399, 429-436.

Polyak, L., Edwards, M.H., Coakley, B.J., Jakobsson, M., 2001. Ice shelves in the Pleistocene Arctic Ocean inferred from glaciogenic deep-sea bedforms. Nature. 410, 453-457.

Polyak, L., Curry, W.B., Darby, D.A., Bischof, J., Cronin, T.M., 2004. Contrasting glacial/interglacial regimes in the western Arctic Ocean as exemplified by a sedimentary record from the Mendeleev Ridge. Paleogeogr. 203, 73-93.

Polyak, L., Jakobsson, M., 2011. Quaternary sedimentation in the Arctic Ocean: Recent advances and further challenges. J. Oceanogr. 24, 52-64.

Reimnitz, E., Kempema, E., Barnes, P., 1987. Anchor ice, seabed freezing, and sediment dynamics in shallow Arctic seas. J. Geophys. Res. Oceans. 92, 14671-14678.

Rigor, I.G., Wallace, J.M., Colony, R.L., 2002. Response of sea ice to the Arctic Oscillation. J. Clim. 15, 2648-2663.

Ruddiman, W.F., Vavrus, S.J., Kutzbach, J.E., 2005. A test of the overdue-glaciation hypothesis. Quat. Sci. Rev. 24, 1-10.

Shackleton, N.J., Opdyke, N.D., 1973. Oxygen isotope and palaeomagnetic stratigraphy of Equatorial Pacific core V28-238: Oxygen isotope temperatures and ice volumes on a 10^5 year and 10^6 year scale. Quat. Res. 3, 39-55.

Short, A.D., Coleman, J.M., Wright, L., 1975. Beach dynamics and nearshore morphology of the Beaufort Sea coast, Alaska.

Sikorski, J.J., Kaufman, D.S., Manley, W.F., Nolan, M., 2009. Glacial-geologic evidence for decreased precipitation during the Little Ice Age in the Brooks Range, Alaska. AAAR. 41, 138-150.

St John, K., Passchier, S., TantillO, B., Darby, D., Kearns, L., 2015. Microfeatures of modern sea-ice-rafted sediment and implications for paleo-sea-ice reconstructions. Ann. Glaciol. 56, 83-93.

Stickley, C.E., St John, K., Koç, N., Jordan, R.W., Passchier, S., Pearce, R.B., Kearns, L.E., 2009. Evidence for middle Eocene Arctic sea ice from diatoms and ice-rafted debris. Nature. 460, 376-379.

Thiede, J., Myhre, A.M., 1996. 36. The palaeoceanographic history of the North Atlantic–Arctic gateways: synthesis of the Leg 151 drilling results, Proceedings of the Ocean Drilling Program, Scientific Results. Ocean Drilling Program College Station, TX, pp. 645-658.

Timmermans, M.L., Marshall, J., 2020. Understanding Arctic Ocean circulation: A review of ocean dynamics in a changing climate. J. Geophys. Res. Oceans. 125, e2018JC014378.

Xuan, C., Channell, J.E., Polyak, L., Darby, D.A., 2012. Paleomagnetism of Quaternary sediments from Lomonosov Ridge and Yermak Plateau: implications for age models in the Arctic Ocean. Quat. Sci. Rev. 32, 48-63.

SUPPLEMENTAL DATA

Cofield, S., 2023a. HLY0503-JPC22 Hiatus Low Fe-Grain Intervals (Version 1) [Data set]. Zenodo. https://doi.org/10.5281/zenodo.8172416

Cofield, S., Darby, D., 2023b. HLY0503-JPC22 Master Data [Data set]. Zenodo. https://doi.org/10.5281/zenodo.8172447

Cofield, S., 2023c. Shannon Cofield Dissertation Supplementary Procedures (Version 1) [Zenodo]. https://doi.org/10.5281/zenodo.8172433

St. John, K., 2023. HLY0503-JPC22 Quartz Sand Grain SEM Analysis [Data set]. Zenodo. https://doi.org/10.5281/zenodo.8172463

APPENDICES

APPENDIX A

OPTICAL MINEROLOGY CODING CRITERIA

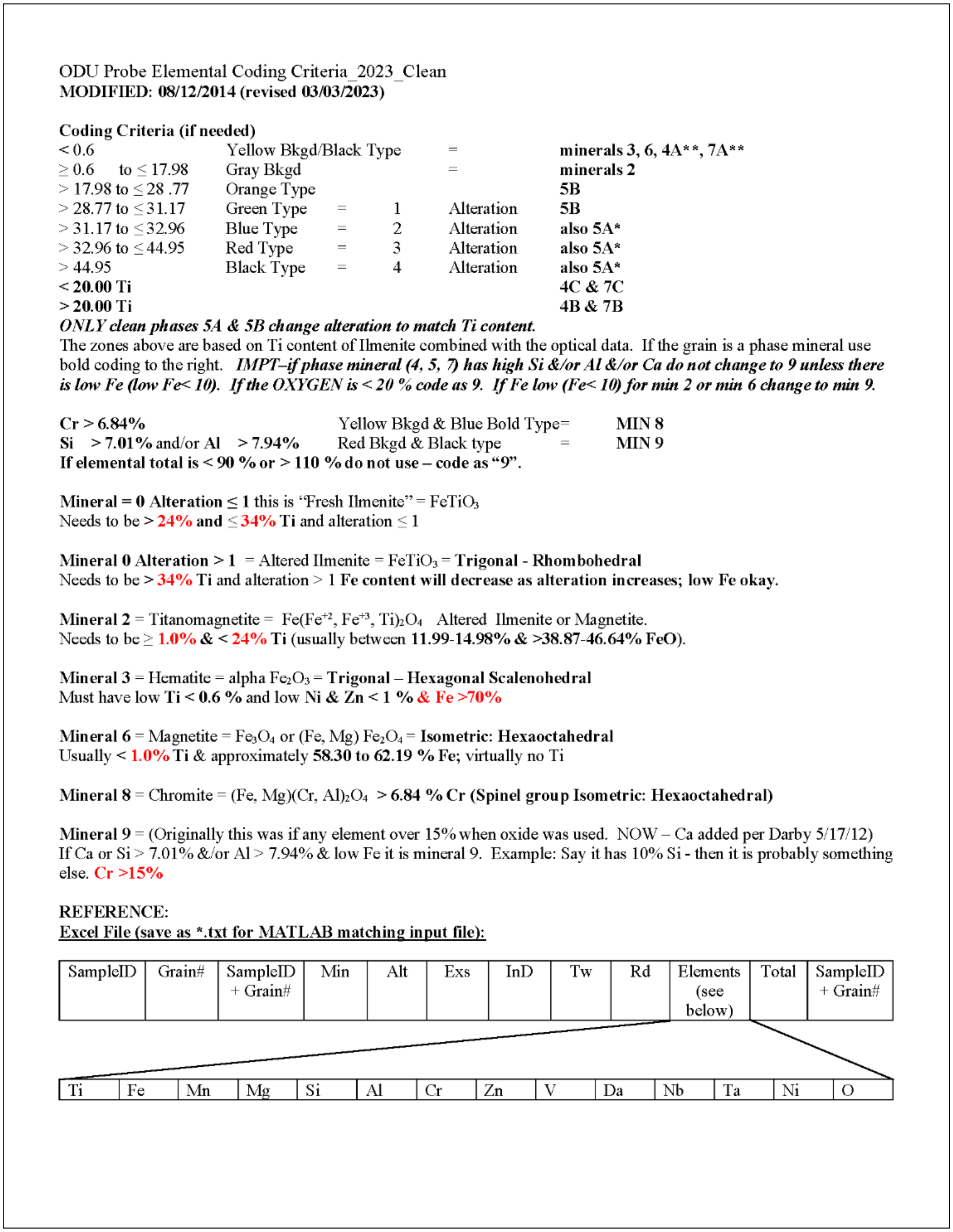

ODU Probe Elemental Coding Criteria_2023_Clean
MODIFIED: 08/12/2014 (revised 03/03/2023)

Coding Criteria (if needed)

< 0.6	Yellow Bkgd/Black Type	=			**minerals 3, 6, 4A**, 7A****
≥ 0.6 to ≤ 17.98	Gray Bkgd	=			**minerals 2**
> 17.98 to ≤ 28 .77	Orange Type				**5B**
> 28.77 to ≤ 31.17	Green Type	=	1	Alteration	**5B**
> 31.17 to ≤ 32.96	Blue Type	=	2	Alteration	**also 5A***
> 32.96 to ≤ 44.95	Red Type	=	3	Alteration	**also 5A***
> 44.95	Black Type	=	4	Alteration	**also 5A***
< 20.00 Ti					**4C & 7C**
> 20.00 Ti					**4B & 7B**

ONLY clean phases 5A & 5B change alteration to match Ti content.
The zones above are based on Ti content of Ilmenite combined with the optical data. If the grain is a phase mineral use bold coding to the right. ***IMPT–if phase mineral (4, 5, 7) has high Si &/or Al &/or Ca do not change to 9 unless there is low Fe (low Fe< 10). If the OXYGEN is < 20 % code as 9. If Fe low (Fe< 10) for min 2 or min 6 change to min 9.***

Cr > 6.84%	Yellow Bkgd & Blue Bold Type=	**MIN 8**
Si > 7.01% and/or **Al > 7.94%**	Red Bkgd & Black type =	**MIN 9**

If elemental total is < 90 % or > 110 % do not use – code as "9".

Mineral = 0 Alteration ≤ 1 this is "Fresh Ilmenite" = $FeTiO_3$
Needs to be **> 24% and** ≤ **34% Ti** and alteration ≤ 1

Mineral 0 Alteration > 1 = Altered Ilmenite = $FeTiO_3$ = **Trigonal - Rhombohedral**
Needs to be **> 34% Ti** and alteration > 1 **Fe content will decrease as alteration increases; low Fe okay.**

Mineral 2 = Titanomagnetite = $Fe(Fe^{+2}, Fe^{+3}, Ti)_2O_4$ Altered Ilmenite or Magnetite.
Needs to be ≥ **1.0% & < 24% Ti** (usually between **11.99-14.98% & >38.87-46.64% FeO**).

Mineral 3 = Hematite = alpha Fe_2O_3 = **Trigonal – Hexagonal Scalenohedral**
Must have low **Ti < 0.6 %** and low **Ni & Zn < 1 % & Fe >70%**

Mineral 6 = Magnetite = Fe_3O_4 or $(Fe, Mg) Fe_2O_4$ = **Isometric: Hexaoctahedral**
Usually **< 1.0% Ti** & approximately **58.30 to 62.19 % Fe**; virtually no Ti

Mineral 8 = Chromite = $(Fe, Mg)(Cr, Al)_2O_4$ **> 6.84 % Cr (Spinel group Isometric: Hexaoctahedral)**

Mineral 9 = (Originally this was if any element over 15% when oxide was used. NOW – Ca added per Darby 5/17/12)
If Ca or Si > 7.01% &/or Al > 7.94% & low Fe it is mineral 9. Example: Say it has 10% Si - then it is probably something else. **Cr >15%**

REFERENCE:
Excel File (save as *.txt for MATLAB matching input file):

SampleID	Grain#	SampleID + Grain#	Min	Alt	Exs	InD	Tw	Rd	Elements (see below)	Total	SampleID + Grain#

Ti	Fe	Mn	Mg	Si	Al	Cr	Zn	V	Da	Nb	Ta	Ni	O

Fig. 25. Updated optical minerology criteria for Fe-grains.

APPENDIX B

K_{ARM}/K AND ISOTOPE CORRELATION FOR AGE MODEL

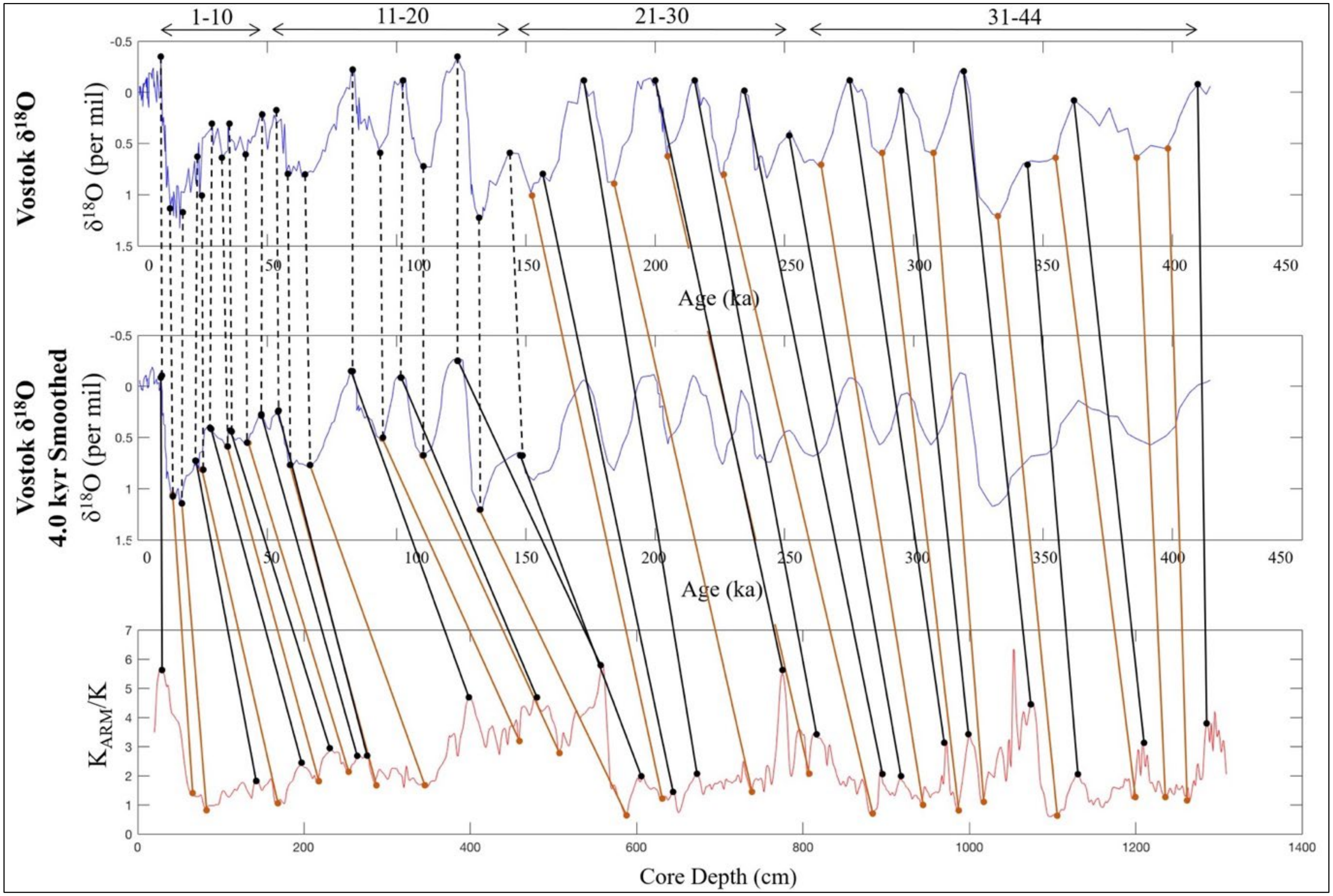

Fig. 26. JPC22 K_{ARM}/K data compared to Vostok $\delta^{18}O$ atmospheric data.

Modern $\delta^{18}O$ data (Petit et al., 1999) are higher resolution and slightly noisier than data >150.0 kyr. To overcome noisy data between 0-150.0 kyr, Vostok $\delta^{18}O$ data are plotted as (Top) raw data and (Middle) 4.0 kyr smoothed data. For these younger ages, (Bottom) JPC22 K_{ARM}/K data (Xuan et al., 2011) are matched to the 4.0kyr smoothed data (solid lines) and linked to the corresponding $\delta^{18}O$ raw data (dashed lines). All data >150.0kyr are matched directly from JPC22 K_{ARM}/K to $\delta^{18}O$ raw data (solid lines). All manual matches are numbered at the top of the Figure and listed in Appendix Table 8.

APPENDIX C

K_{ARM}/K AND ISOTOPE MATCHING PICKS FOR AGE MODEL

Table 8. K_{ARM}/K and Vostok isotope matching picks for age model.

Matching Pick	K_{ARM}/K	Vostok δ^{18}O		^{14}C Dates
	JPC22	Original Data	4.0 kyr Smoothed Data	
	Depth	Age	Age	
(Number)	(cm)	(ka)	(ka)	(ka)
1	27		8.9	
2	65		13.3	
3	81		16.2	
	100			17.940
	138			21.520
4	143		22.6	
5	167		23.6	
6	197		28.8	
7	216		34.1	
8	230		35.5	
9	252		41.0	
10	265		47.8	
11	277		53.9	
12	286		58.4	
13	347		66.6	
14	400		82.8	
15	458		95.1	
16	477		102.3	
17	507		109.8	
18	560		123.5	
19	587		133.3	
20	606		147.2	
21	629	152.0		
22	645	156.1		
23	673	171.4		
24	738	184.1		
25	774	200.4		
26	805	204.7		
27	813	214.6		
28	881	226.0		
29	893	233.2		
30	918	252.0		
31	942	263.6		
32	972	274.8		
33	986	286.6		
34	999	295.1		
35	1016	306.6		

Table 8 continued

Matching Pick	K_{ARM}/K	Vostok $\delta^{18}O$		^{14}C Dates
	JPC22	Original Data	4.0 kyr Smoothed Data	
	Depth	Age	Age	
(Number)	(cm)	(ka)	(ka)	(ka)
36	1098	332.8		
37	1103	332.8		
38	1129	345.3		
39	1195	355.0		
40	1209	375.5		
41	1236	385.6		
42	1266	397.6		
43	1275	409.9		

Table provides manual JPC22 K_{ARM}/K and Vostok $\delta^{18}O$ matches from Fig. 26. Previously analyzed ^{14}C dates are also included (Xuan et al., 2011). For data 0-150.0 kyr, JPC22 K_{ARM}/K data are matched to the 4.0 kyr smoothed data and linked to the corresponding $\delta^{18}O$ data (italic numbers). All data >150.0 kyr are matched directly from JPC22 K_{ARM}/K to $\delta^{18}O$ (solid lines) (Fig. 26).

APPENDIX D

PCHIP INTERPOLATION FOR AGE MODEL

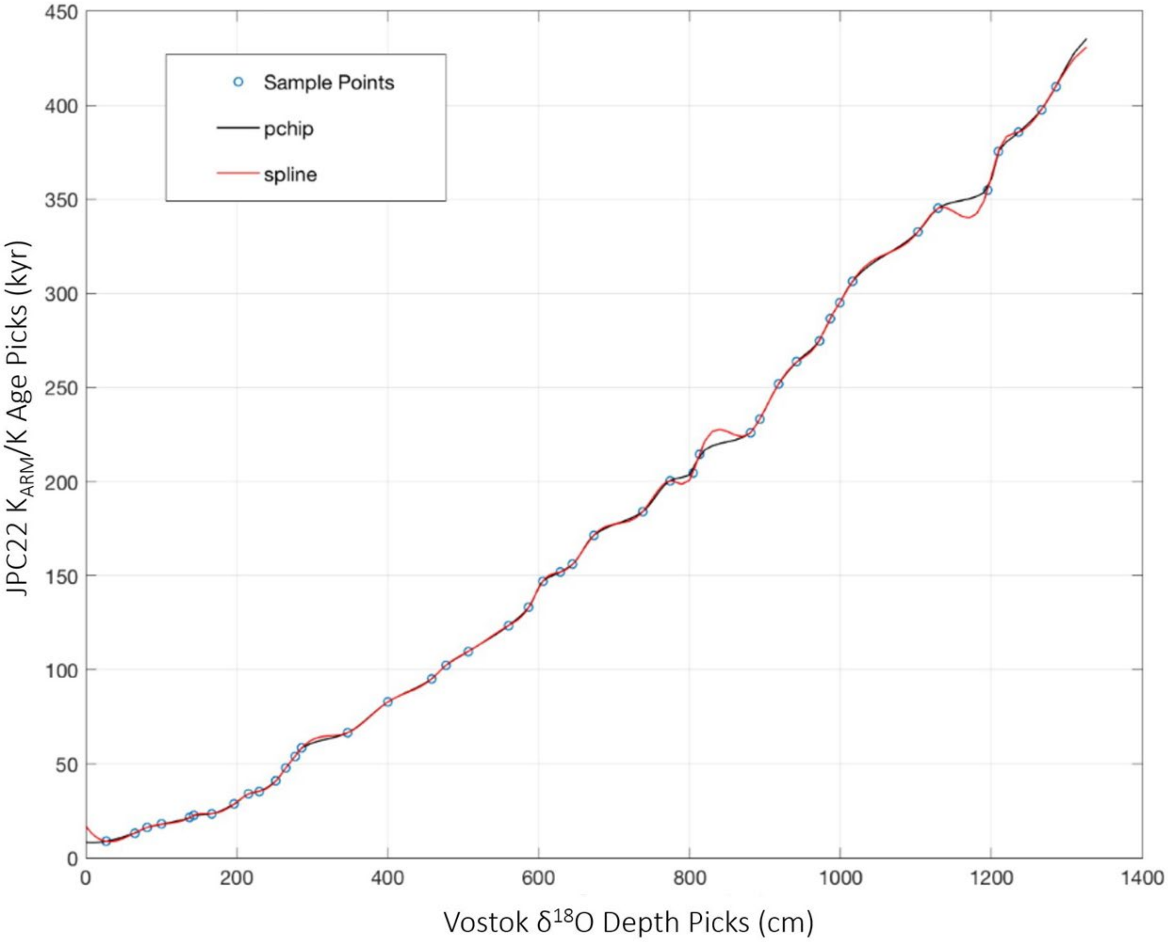

Fig. 27. JPC22 ages calculated using a PCHIP in MATLAB. Figure also shows a spline interpretation, but the spline was not used due to large tails at the ends of the dataset, and PCHIP interpolation has less deviation or variation from the matching picks. Standard error must be assumed from the data used from the input data. For this study, input data are the matching picks, so the standard error is deferred to the original Vostok dataset. Vostok data accuracy is better than ±10.0 kyr for most of the record, and better than ±5.0 kyr for the last 110.0 kyr (1999). Accuracy never exceeds ±15.0 kyr. (Petit et al., 1999).

APPENDIX E

CALCULATED AGES AND CORE DEPTH (MIS 2-6)

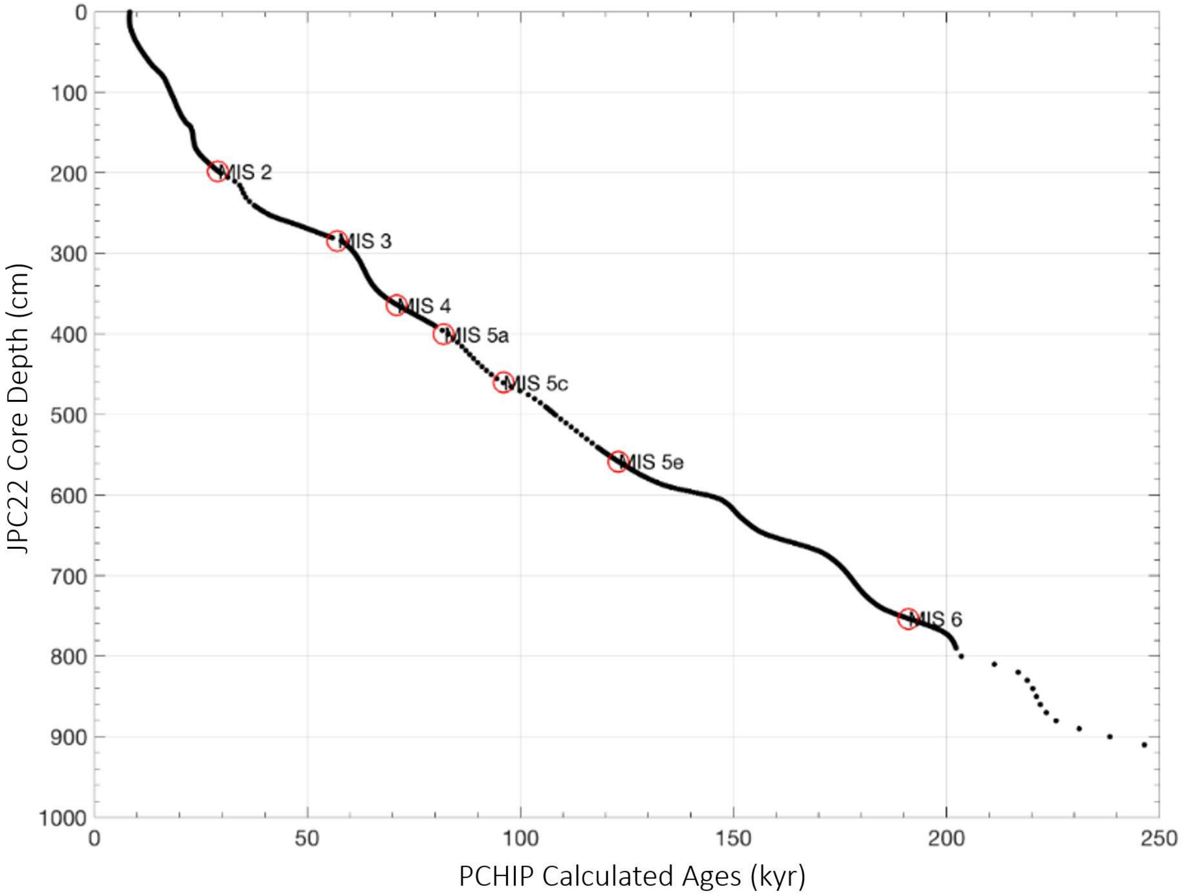

Fig. 28. JPC22 PCHIP calculated ages (kyr) plotted against JPC22 core depth (cm) through MIS 6. Figure highlights the initiation age for each MIS (red circles). This study calculated an age model for the entire core; however, the JPC22 age model seems most reliable through MIS 6 (<753.5 cm core depth).

APPENDIX F

CALCULATED AGES AND CORE DEPTH (MIS 2-11)

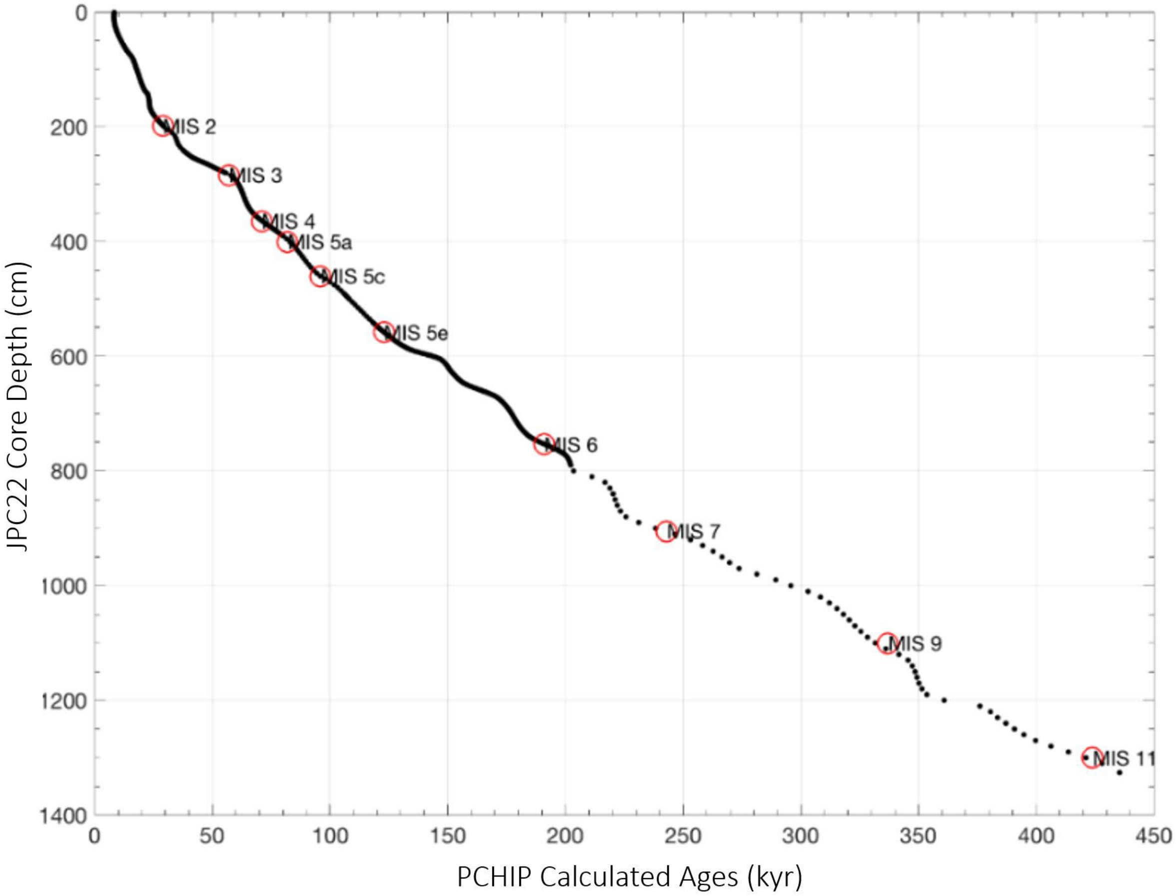

Fig. 29. JPC 22 calculated ages (kyr) from PCHIP interpolation plotted against core depth (cm) through MIS 11. Figure highlights the initiation age for each MIS (red circles). While this study calculated an age model through MIS 11, the JPC22 age model seems most reliable only through MIS 6 (<753.5 cm core depth).

APPENDIX G

SEDIMENTATION RATE CALCULATIONS

Table 9. Sedimentation rate slope calculations.

MIS	**Start Age**	**Start Depth**	**End Age**	**End Depth**	**Sedimentation Rate**
	(ka)	**(cm)**	**(ka)**	**(cm)**	**(cm/kyr)**
1	8.0	8.5	11.6	52.5	12.4
2	11.8	54.5	14.3	70.5	6.5
2	14.3	70.5	16.6	84.5	6.1
2	16.6	84.5	21.6	138.5	10.7
2	21.6	138.5	22.8	145.4	6.0
2	22.8	145.4	23.7	168.7	25.6
2	23.7	168.7	34.1	215.5	4.5
4	59.0	288.5	61.4	302.5	5.7
4	61.4	302.5	65.6	341.5	9.2
4	65.6	341.5	71.6	365.5	4.1
6	130.2	580.8	147.0	605.5	1.5
6	147.0	605.5	155.9	644.5	4.4
6	155.9	644.5	172.1	675.5	1.9
6	172.1	675.5	182.7	732.5	5.4
6	182.7	732.5	191.7	754.5	2.4

To identify variations in sedimentation rates during MIS 2, 4, and 6, we subdivided each stage by variations in slopes. We selected six slopes during MIS 2 (Fig. 7), three slopes during MIS 4 (Fig. 8), and five slopes during MIS 6 (Fig. 9). Table 1 lists average sedimentation rates for each stage, MIS 1-11.

APPENDIX H

AGE MODEL PCHIP DATA TAIL

Table 10. Age model PCHIP data tail calculations.

Depth	Calculated Ages from PCHIP	Tails Present	Calculated Ages from PCHIP	Depositional Rate	Time per cm	Adjusted Ages in PCHIP Tail	Calculated Ages from PCHIP (tails calculated)
(cm)	(ka)	(X)	(ka)	(cm/kyr)	(kyr)	(ka)	(ka)
0.5	8.171	X	8.299	0.1		7.477	7.477
1.5	8.171	X	8.266	-30.3	-0.033	7.554	7.554
2.5	8.171	X	8.238	-35.7	-0.028	7.632	7.632
3.5	8.171	X	8.215	-43.5	-0.023	7.709	7.709
4.5	8.171	X	8.196	-52.6	-0.019	7.786	7.786
5.5	8.171	X	8.182	-71.4	-0.014	7.863	7.863
6.5	8.171	X	8.173	-111.1	-0.009	7.940	7.940
7.5	8.171	X	8.168	-200.0	-0.005	8.017	8.017
8.5	8.171	X	8.167	-1000.0	-0.001	8.094	8.094
9.5	8.171		8.171	250.0	0.004		8.171
10.5	8.179		8.179	125.0	0.008		8.179
11.5	8.192		8.192	76.9	0.013		8.192
12.5	8.208		8.208	62.5	0.016		8.208
13.5	8.229		8.229	47.6	0.021		8.229
14.5	8.254		8.254	40.0	0.025		8.254
15.5	8.283		8.283	34.5	0.029		8.283
16.5	8.315		8.315	31.3	0.032		8.315
17.5	8.352		8.352	27.0	0.037		8.352
18.5	8.392		8.392	25.0	0.04		8.392
19.5	8.436		8.436	22.7	0.044		8.436
20.5	8.484		8.484	20.8	0.048		8.484
21.5	8.535		8.535	19.6	0.051		8.535
22.5	8.590		8.590	18.2	0.055		8.590
23.5	8.649		8.649	16.9	0.059		8.649
24.5	8.710		8.710	16.4	0.061		8.710
25.5	8.775		8.775	15.4	0.065		8.775
26.5	8.844		8.844	14.5	0.069		8.844
27.5	8.915		8.915	14.1	0.071		8.915
28.5	8.990		8.990	13.3	0.075		8.990
29.5	9.068		9.068	12.8	0.078		9.068

Table 10 Continued

Depth	Calculated Ages from PCHIP	Tails Present	Calculated Ages from PCHIP	Depositional Rate	Time per cm	Adjusted Ages in PCHIP Tail	Calculated Ages from PCHIP (tails calculated)
(cm)	(ka)	(X)	(ka)	(cm/kyr)	(kyr)	(ka)	(ka)
30.5	9.148		9.148	12.5	0.08		9.148
31.5	9.232		9.232	11.9	0.084		9.232
32.5	9.319		9.319	11.5	0.087		9.319
33.5	9.408		9.408	11.2	0.089		9.408
34.5	9.500		9.500	10.9	0.092		9.500
35.5	9.595		9.595	10.5	0.095		9.595
36.5	9.693		9.693	10.2	0.098		9.693
37.5	9.793		9.793	10.0	0.1		9.793
38.5	9.895		9.895	9.8	0.102		9.895
39.5	10.000		10.000	9.5	0.105		10.000
40.5	10.108		10.108	9.3	0.108		10.108
41.5	10.218		10.218	9.1	0.11		10.218
42.5	10.329		10.329	9.0	0.111		10.329
43.5	10.444		10.444	8.7	0.115		10.444
44.5	10.560		10.560	8.6	0.116		10.560
45.5	10.678		10.678	8.5	0.118		10.678
46.5	10.798		10.798	8.3	0.12		10.798
47.5	10.920		10.920	8.2	0.122		10.920
48.5	11.044		11.044	8.1	0.124		11.044
49.5	11.170		11.170	7.9	0.126		11.170
50.5	11.298		11.298	7.8	0.128		11.298
51.5	11.427		11.427	7.8	0.129		11.427
52.5	11.558		11.558	7.6	0.131		11.558
				MIS 1 Average time per cm (kyr) =	**0.077**		

To address the data tail, sedimentation (depositional) rates are calculated, including the average time per interval during MIS 1, which has a calculated average depositional rate of 0.077 kyr/cm. PCHIP calculated ages are adjusted for intervals within the data tail (0.5-8.5 cm) by subtracting the calculated average time per interval of 0.077 cm/kyr from the previous age (see “Adjusted Ages” on this table). For all data tail intervals, the average depositional rate is 12.4 cm/kyr and the time per cm is 0.1 cm/kyr.

APPENDIX I

HIATUS CLUSTER CALCULATIONS

Table 11. Hiatus cluster calculations.

Location	Hiatus Cluster Initiation		Hiatus Cluster Termination		Termination Hiatus Duration	Corrected Hiatus Cluster End Date	Total Hiatus Cluster Duration
	"Start Date"		"Start Date"				
	Hiatus ID	(ka)	Hiatus ID	(ka)	(kyr)	(ka)	(kyr)
Barents-Svalbard	BSVL1	132.1	BSVL6	148.2	1.33	130.8	17.8
Barents-Svalbard	BSVL7	156.3	BSVL11	169.1	1.33	155.0	14.1
Svalbard	SVLb3	132.1	SVLb6	149.1	1.33	130.8	18.3
Svalbard	SVLb7	156.3	SVLb13	172.4	1.64	154.7	16.1
Beaufort Sea	BFTS1	135.0	BFTS6	148.0	2.81	132.2	15.8
Beaufort Sea	BFTS7	154.5	BFTS13	178.5	1.80	152.7	25.8
Wrangel Island and New Siberian Islands	WINS1	134.8	WINS4	145.5	2.81	132.2	13.5
Wrangel Island and New Siberian Islands	WINS6	156.3	WINS9	168.0	1.64	154.7	13.3

All hiatuses are identified and listed by their "start date". For example (from Table 3), BSLV6 has an initiation "starting date" of 148.2 ka, and the hiatus cluster terminates with hiatus BSLV1 "starting" at 132.1 ka. However, these "starting dates" exclude BSLV1 duration of 1.33 kyr. Therefore, the full range of each hiatus cluster is calculated by subtracting the hiatus initiation "start date" (i.e., BLSV6) from the hiatus termination "start date" (i.e., BLSV1), and incorporating the duration of the final hiatus (i.e., 1.33 kyr). Accounting for the 1.33 kyr duration for BSLV1, the “hiatus cluster” ended at 130.8 ka. The full “hiatus cluster” duration spans from 148.2 ka to 130.8 ka for a total hiatus cluster duration of 17.4 kyr.

Barents Svalbard SAs have two MIS 6 hiatus clusters: (1) 156.3-169.1 ka (BSVL7-11), with a total duration of 14.1 kyr (155.0-169.1 ka), using 1.33 kyr as the hiatus duration at 156.3 ka; and (2) 132.1-148.2 ka (BSVL1-6), with a total duration of 130.8-148.2 ka, or 17.8 kyr, using 1.33 kyr as the hiatus duration at 132.1 ka (Table 3). SA 33 has two hiatus clusters: (1) 156.3-172.4 ka (SVLb7-13), with a total duration of 16.1 kyr (154.7-172.4 ka), using 1.64 kyr as the hiatus duration at 156.3 ka; and (2) 132.1-149.1 ka (SVLb3-6), with a total duration of 130.8-149.1 kyr, or 18.3. kyr, using 1.33 kyr as the hiatus duration at 132.1 ka (Table 3).

Beaufort Sea SA MIS 6 hiatus clusters include: (1) 135.0-148.0 ka (BFTS1-6), with a total duration of 15.8 kyr (132.2-148.0 ka), using 2.81 kyr as the hiatus duration at 135.0 ka; and (2) 154.5-178.5 ka (BFTS7-13), with a total duration of 25.8 kyr (152.7-178.5 ka), using 1.80 kyr as the hiatus duration at 154.5 ka (Table 4). Wrangel Island and New Siberian Islands SAs have two MIS 6 hiatus clusters: (1) 134.8-145.5 ka (WINS1-4) with a total duration of 13.5 kyr (132.2-145.5 ka), using 2.81 kyr as the hiatus duration at 134.8 ka; and (2) 156.3-168.0 ka (WINS6-9) with a total duration of 13.3 kyr (or 154.7-168.0 ka), using 1.64 kyr as the hiatus duration at 156.3 ka (Table 4).

APPENDIX J

CENTRAL ARCTIC MIS 6 HIATUS CLUSTER AVERAGES (130.8-146.9 ka)

Table 12. Central Arctic MIS 6 hiatus cluster average (130.8-146.9 ka).

Location	**Hiatus Cluster Initiation**		**Hiatus Cluster Termination**		**Termination Hiatus Duration**	**Corrected Hiatus Cluster End Date**	**Total Hiatus Cluster Duration**
	"Start Date"		**"Start Date"**				
	Hiatus ID	**(ka)**	**Hiatus ID**	**(ka)**		**(ka)**	**(kyr)**
Kara Sea	KARs5	145.5	KARs1	134.8			
Kara Sea Rivers	KARr8	149.1	KARr3	132.1			
Bering Strait	BER5	143.6	BER1	134.8			
Laptev Sea	LAP6	148.2	LAP1	132.1			
Canadian Archipelago	CAN6	148.2	CAN1	134.8			
Beaufort Sea	BFTS6	148.2	BFTS1	132.1			
Wrangel Island and New Siberian Islands	WINS4	145.5	WINS1	134.8			
Averages		146.9		133.6	2.81	130.8	16.1

Overlapping hiatus are clustered together to calculate an average hiatus cluster age. The average ages for these hiatus clusters are 133.6-146.9 ka, with a total average duration of 16.1 kyr (130.8-146.9 ka), using 2.81 kyr as the longest hiatus duration at the closest interval 134.1 ka (Table 4). Hiatus calculation referenced in Section 4.8.1 and Table 11.

APPENDIX K

CENTRAL ARCTIC MIS 6 HIATUS CLUSTER AVERAGES (157.0-170.9 ka)

Table 13. Central Arctic MIS 6 hiatus cluster average (157.0-170.9 ka).

Location	**Hiatus Cluster Initiation**		**Hiatus Cluster Termination**		**Termination Hiatus Duration**	**Corrected Hiatus Cluster End Date**	**Total Hiatus Cluster Duration**
	"Start Date"		**"Start Date"**				
	Hiatus ID	**(ka)**	**Hiatus ID**	**(ka)**		**(ka)**	**(kyr)**
Kara Sea	KARs10	169.1	KARs6	156.3			
Kara Sea Rivers	KARr15	172.7	KARr10	155.9			
Bering Strait	BER12	172.4	BER8	161.6			
Laptev Sea	LAP13	172.4	LAP8	160.9			
Canadian Archipelago	CAN8	168.5	CAN7	167.4			
Beaufort Sea	BFTS13	172.4	BFTS7	154.2			
Wrangel Island and New Siberian Islands	WINS9	168.5	WINS5	156.3			
Averages		170.9		158.9	1.91	157.0	13.90

Overlapping hiatus are clustered together to calculate an average hiatus cluster age. The average ages for these hiatus clusters are 158.9-170.9 ka, with a total average duration of 13.9 kyr (157.0 ka to 170.9 ka), using 1.91 kyr as the longest, adjacent hiatus duration at 158.3 ka (Table 4). Hiatus calculation referenced in Section 4.8.1 and Table 11.

VITA

Shannon M. Cofield
Department of Ocean and Earth Sciences
Old Dominion University
Norfolk, VA 23529

EDUCATION

Ph.D. (Expected August 2023) in Geological Oceanography, Old Dominion University, Norfolk, VA 23529
M.S. (May 2015) in Geological Oceanography, Old Dominion University, Norfolk, VA 23529
B.S. (May 2012) in Ocean, Earth, And Atmospheric Sciences, Old Dominion University, Norfolk, VA 23529

PROFESSIONAL EXPERIENCE

2020-Present	Bureau of Ocean Energy Management, Marine Minerals Division, Oceanographer
2012-2020	Teaching Assistant and Lecturer, Old Dominion University, Norfolk, VA 23529
2010-2012	Laboratory Assistant, Old Dominion University, Norfolk, VA 23529

CONFERENCE PRESENTATIONS

S. Cofield, P. Knorr, and M. Mueller. Bureau of Ocean Energy Management, Marine Minerals Program (BOEM-MMP): Steward of offshore critical mineral resources. Oral presentation delivered at Geological Society of America, Reston, Virginia, March 2023

S. Cofield and D. Darby, "Constraints on the Drift of Ice Across the Arctic Ocean During the Last Glacial Intervals (MIS2 and 6)" Poster presentation delivered at Ocean Sciences, Portland, Oregon, February 2018

S. Cofield, D. Darby, and K. St. John, "History of ice-rafting in the Arctic Ocean during Marine Isotope Stage (MIS) 2 and MIS 4", Poster presentation delivered at American Geophysical Union, San Francisco, California, November 2016

S. Cofield, D. Darby, and K. St. John, "History of ice-rafting in the Arctic Ocean during the last glacial maximum" Poster presentation delivered at Geological Society of America, Denver, Colorado, October 2015